UNIVERSIDADE ESTADUAL DE CAMPINAS
Faculdade de Engenharia Química

TÁSSIA LINS DA SILVA QUARESMA

Study and modelling of flame propagation on the BML framework using STOKES

Estudo e modelagem da propagação de chamas pela abordagem BML utilizando o STOKES

CAMPINAS - SP
2021

TÁSSIA LINS DA SILVA QUARESMA

Study and modelling of flame propagation on the BML framework using STOKES

Estudo e modelagem da propagação de chamas pela abordagem BML utilizando o STOKES

Dissertação apresentada à Faculdade de Engenharia Química da Universidade Estadual de Campinas como parte dos requisitos exigidos para a obtenção do título de Mestra em Engenharia Química

Dissertation presented to the School of Chemical Engineering of the University of Campinas in fulfillment of the requirements for the degree in Master in Chemical Engineering

Supervisor: Prof. Dr. Sávio Souza Venâncio Vianna

ESTE TRABALHO CORRESPONDE À VERSÃO FINAL DA DISSERTAÇÃO DEFENDIDA PELA ALUNA TÁSSIA LINS DA SILVA QUARESMA, ORIENTADA PELO PROF. DR. SÁVIO SOUZA VENÂNCIO VIANNA

Campinas - SP
2020

Ficha catalográfica
Universidade Estadual de Campinas
Biblioteca da Área de Engenharia e Arquitetura
Rose Meire da Silva - CRB 8/5974

Q26s

Quaresma, Tássia Lins da Silva, 1992-
Study and modelling of flame propagation on the BML framework using STOKES / Tássia Lins da Silva Quaresma. – Campinas, SP : [s.n.], 2021.

Orientador: Sávio Souza Venâncio Vianna.
Dissertação (mestrado) – Universidade Estadual de Campinas, Faculdade de Engenharia Química.

1. Combustão - Modelos matemáticos. 2. Turbulência - Modelos matemáticos. 3. Explosões. 4. Gases inflamáveis - Acidentes - Avaliação de Risco. I. Vianna, Sávio Souza Venâncio, 1975-. II. Universidade Estadual de Campinas. Faculdade de Engenharia Química. III. Título.

Informações para Biblioteca Digital

Título em outro idioma: Estudo e modelagem da propagação de chamas pela abordagem BML utilizando o STOKES
Palavras-chave em inglês:
Combustion - Mathematical models
Turbulence - Mathematical models
Explosions
Flammable gases - Accidents - Risk assessment
Área de concentração: Engenharia Química
Titulação: Mestra em Engenharia Química
Banca examinadora:
Sávio Souza Venâncio Vianna [Orientador]
Tânia Suaiden Klein
Gabriela Cantarelli Lopes
Data de defesa: 04-03-2021
Programa de Pós-Graduação: Engenharia Química

Identificação e informações acadêmicas do(a) aluno(a)
- ORCID do autor: https://orcid.org/0000-0003-0214-0595
- Currículo Lattes do autor: http://lattes.cnpq.br/0386958928247069

Folha de Aprovação da Defesa de Dissertação de Mestrado da aluna TÁSSIA LINS DA SILVA QUARESMA, aprovada aos quatro dias do mês de março do ano de dois mil e vinte e um pela comissão examinadora constituída pelos doutores:

Prof. Dr. Sávio Souza Venâncio Vianna
Presidente e Orientador
FEQ / UNICAMP
Videoconferência

Prof. Dra. Tânia Suaiden Klein
Escola de Química / UFRJ
Videoconferência

Prof. Dra. Gabriela Cantarelli Lopes
DEQ / UFSCar
Videoconferência

A Ata da defesa com as respectivas assinaturas dos membros encontra-se no SIGA/Sistema de Fluxo de Dissertação/Tese e na Secretaria do Programa da Unidade

To my grandma Luzia.

À minha avó Luzia.

Acknowledgments

I'm grateful to my parents, who have been by my side despite the distance. I value and acknowledge our history as the most important part to the development of my character as a conscious human being.

I thank Rodrigo for the daily support, affection, partnership, love and wisdom. You have encouraged me the most to believe in myself. I'm thankful everyday for having met you (twice?) and for having chosen you. Thank you for choosing me.

I thank my life sisters: Gisele, Sabrina, Stefanie, Julia, Taline & Henrique. How I miss our time together! The memories of our *adventures* in the past really helped me out to go through some hard moments in the last two years. I wish we could get together again in a non-pandemic world ...

Thanks to the lab colleagues: Tati, Karenzita, Mafe & João. Among popcorn, coffees, reboots and laughter, there was always a lot of CFD. Thank you very much for all the kindness of always helping me with so many tasks with willingness and joy. Thank you for being shoulders to cry on, for the fun and teachings, it was a privilege to work with you.

Thanks to Prof. Sávio S. V. Vianna for having received me with open arms in L4R1S4 lab. Your words of motivation and appreciation for the Brazilian scientific research have taught me greatly to become aware of the relevance of our work.

The present work was supported by the National Council for Scientific and Technological Development (CNPq).

Agradecimentos

Sou grata aos meus pais, que mesmo na distância, sempre estiveram comigo. Eu valorizo e reconheço nossa história como a parte mais importante no desenvolvimento do meu caráter como um ser humano consciente do mundo e de mim mesma.

Agradeço ao Rodrigo pelo incentivo diário, carinho, parceria, amor e sabedoria. Obrigada por me ajudar a acreditar em mim mesma. Sou grata todos os dias por ter te conhecido (duas vezes?) e por ter te escolhido. Obrigada por me escolher.

Agradeço às minhas irmãs de vida: Gisele, Sabrina, Stefanie, Julia, Taline & Henrique. Que saudade dos rolês! As lembranças das nossas *aventuras* me ajudaram muito a atravessar alguns momentos difíceis nos dois últimos anos. Quero encontrá-las de novo em um mundo sem pandemia ...

Obrigada aos colegas de laboratório: Tati, Karenzita, Mafe e João. Entre pipocas, cafés, reboots e risadas, sempre teve muito CFD. Agradeço muito toda a gentileza de sempre terem me ajudado em tantas tarefas com muita boa vontade e alegria. Obrigada pelo ombro amigo, diversão e ensinamentos, foi um privilégio trabalhar com vocês.

Agradeço ao Prof. Sávio S. V. Vianna por ter me recebido de portas abertas no laboratório L4R1S4. Suas palavras de motivação e valorização da pesquisa científica brasileira muito me ensinaram a tomar consciência da relevância do nosso trabalho.

O presente trabalho foi realizado com apoio do Conselho Nacional de Desenvolvimento Científico e Tecnológico (CNPq).

"Kant's notion of autonomy stands in stark contrast to this. When we act autonomously, according to a law we give ourselves, we do something for its own sake, as an end in itself. We cease to be instruments of purposes given outside us. This capacity to act autonomously is what gives human life its special dignity. It marks out the difference between persons and things."

Justice - What's the right thing to do?
Michael J. Sandel

"A concepção de Kant sobre autonomia é o absoluto oposto disso. Quando agimos com autonomia e obedecemos a uma lei que estabelecemos para nós mesmos, estamos fazendo algo por fazer algo, como uma finalidade em si mesma. Deixamos de ser instrumentos de desígnios externos. Essa capacidade de agir com autonomia é o que confere à vida humana sua dignidade especial. Ela estabelece a diferença entre pessoas e coisas."

Justiça - O que é fazer a coisa certa?
Michael J. Sandel

Abstract

The numerical modelling of gas explosions in the context of computational fluid dynamics (CFD) is a very important tool to predict flame behaviour and the associated consequences. This is particularly relevant in the presence of obstacles or highly congested areas, where the generation of turbulence may significantly contribute to flame acceleration. In combustion modelling, the effects of turbulence on flame propagation are incorporated in the reaction rate source term. In this context, this work is focused on analysing and improving the reaction rate models implemented in STOKES (*Shock Towards Kinetic Explosion Simulator*), an in-house developed CFD code dedicated to the simulation of gas explosions in complex geometries. STOKES counts on the Bray-Moss-Libby (BML) model for the turbulent reaction rate calculation and a laminar burning model to account for the initial flame development. Flamelets models such as the BML are highly dependant on adjustable constants. This poses a challenge to broaden the applicability of STOKES, since extensive calibration of model constants is required for all new cases. In order to address this main issue, two pragmatic approaches are proposed in the scope of this work. The first is dedicated to the modelling of a dynamic stretch factor to account for the effects of the flow to the flame stretch. The second refers to development of a hybrid model for the turbulent reaction rate by combining the BML model with the fractal concept for modelling the flame length scale of wrinkling. Simulations were conducted in partially obstructed combustion chambers of relatively small sizes, and a semi-confined geometry of large scale dimensions representing a typical process module. Although the proposed dynamic stretch factor lead to a slight improvement in the corresponding flame time arrivals, an unexpectedly enlarged flame region was observed. On the other hand, the hybrid approach showed an improved agreement with literature data when compared to the combustion model originally implemented in STOKES. However, the improvement attained by the hybrid approach was achieved on the account of adjustments in the laminar burning model constants. This observation drew attention to the importance of accurately predicting the initial laminar kernel development as well as the transition from the laminar to the turbulent propagation regimes.

Keywords: Premixed turbulent combustion; BML model; Fractal model; Stretch factor; Accidental gas explosion.

Resumo

A modelagem numérica de explosões de gás no contexto da fluidodinâmica computacional (CFD) é uma importante ferramenta para predizer o comportamento da chama e suas consequências associadas. Esta importância é particularmente relevante na presença de obstáculos ou áreas altamente congestionadas, em que a geração de turbulência pode contribuir significativamente para a aceleração da chama. Na modelagem da combustão, os efeitos da turbulência na propagação das chamas são incorporados no termo fonte da taxa de reação. Nesse contexto, este trabalho se concentra na análise e no melhoramento dos modelos de reação química implementados no STOKES (*Shock Towards Kinetic Explosion Simulator*), um código de CFD desenvolvido por pesquisadores da Unicamp dedicado à simulação de explosões de gás em geometrias complexas. STOKES conta com o modelo Bray-Moss-Libby (BML) para o cálculo da taxa de reação turbulenta e um modelo de queima laminar representa o desenvolvimento inicial da chama. Modelos *flamelet* como o BML são altamente dependentes de constantes ajustadas. Isso representa um desafio à ampliação da aplicabilidade do STOKES, uma vez que é necessária a calibração das constantes dos modelos para todos os novos casos. De forma a endereçar essa questão principal, duas abordagens pragmáticas são propostas no escopo desse trabalho. A primeira é dedicada à modelagem de um fator de estiramento dinâmico para contabilizar os efeitos do escoamento no estiramento da chama. A segunda refere-se ao desenvolvimento de um modelo híbrido para a taxa de reação turbulenta, por meio da combinação do modelo BML com o conceito fractal para a modelagem da escala de comprimento de enrugamento da chama. Simulações foram conduzidas em câmaras de combustão parcialmente obstruídas de tamanhos relativamente pequenos, e uma geometria semi-confinada de comprimento de larga escala representando um módulo de processo. Apesar de o fator de estiramento dinâmico proposto ter levado a uma pequena melhora no tempo de chegada da chama, um aumento inesperado da região da chama foi observado. Por outro lado, a abordagem híbrida mostrou uma melhor concordância com dados da literatura do que o modelo originalmente implementado no STOKES. Entretanto, a melhora atingida pelo modelo híbrido foi obtida em decorrência de ajustes em parâmetros do modelo de queima laminar. Esta observação chamou atenção para a importância de se predizer acuradamente o desenvolvimento inicial laminar do núcleo da chama, bem como a transição do regime de queima laminar para o turbulento.

Palavras Chaves: Combustão turbulenta pré-misturada; Modelo BML; Modelo fractal; Fator de estiramento; Explosão acidental de gás.

List of Figures

List of Tables

Contents

1 Introduction

The numerical modelling of gas explosions has a number of relevant applications in the fields of physics and engineering. Computational fluid dynamics (CFD) simulations of gas explosions have shed light on the underlying mechanisms of flame instabilities and turbulence-flame interaction, aiding the development of new technologies on power generation, the understanding of supernovae, and the prevention of accidental gas explosions.

In process safety studies, the prediction of gas explosion consequences due to the overpressure effects and thermal radiation is no simple task, especially in the presence of obstacles or highly congested areas typically present in industrial plants. The obstacles ahead of the flame front enhances the turbulent flow, creating strong flame instabilities which can contribute to flame acceleration.

An accidental scenario of gas explosion generally starts with a sequence of events: loss of containment, flammable cloud formation, ignition and explosion. In other words, after a leakage the flammable gas is likely to disperse and mix with the atmospheric air, generating a flammable reactant mixture. This mixture can be exposed to an ignition source, culminating in a gas explosion characterised by flame propagation and great amounts of heat release.

A situation similar to that took place at the Buncefield oil storage depot in 2005. One of the petrol storage tanks overfilled after many failures in the control system. The liquid petrol vaporised, forming a vapour cloud that ignited, generating an enormous explosion and fire. Most of the damage was caused by the severe explosion due to flame acceleration when passing over the surrounding trees. The fire continued for five days with significant structural damage, more than 40 people injured, and a financial loss of ten million pounds (CONTROL OF MAJOR ACCIDENTS, 2011)

In combustion science, gas explosions are studied within the context of premixed turbulent combustion, where the numerical modelling of the turbulent reaction rate is a matter of utmost importance. Predicting overpressure peaks, thermal radiation and associated consequences ultimately depends on how fast the flame can process the premixed reactants into products. Because of that, many models for the reaction rate of premixed turbulent flames have been extensively proposed and improved on the basis of different regimes of flame propagation.

This work is focused on analysing and improving the reaction rate models implemented in STOKES, an in-house developed CFD code dedicated to the simulation of gas explosions in complex geometries. STOKES counts on the Bray-Moss-Libby (BML) model for the turbulent reaction rate calculation. Also, a laminar burning model is

implemented to account for the initial laminar flame kernel development. Transition from laminar to turbulent regimes of propagation is taken to occur at a specified turbulent Reynolds number.

However, the effects of flame stretch are disregarded in the BML model implemented in STOKES as originally conceived. Also, the turbulence contribution to the reaction rate is made by means of an empirical correlation, inserting additional constants to the already highly constant-dependent flamelet model. This poses a challenge to broaden the applicability of STOKES, since extensive calibration of model constants is required for all new cases.

Furthermore, STOKES is based on the porosity-parameterised transport equations, according to the Porosity Distributed Resistance (PDR) model. The obstacles are represented by a porous mesh, where additional terms of frictional resistance and turbulence generation are appended to the momentum equations. The various constants of the combustion models are in line with the solution of the reacting flow field where a refined mesh is required to capture the shear layers around obstacles. This is not the case of STOKES. Because of that, additional tuning may be necessary to cope with the PDR approach.

In order to address these issues, two pragmatic approaches are proposed in the scope of this work. The first is dedicated to the modelling of a dynamic stretch factor to account for the effects of the flow to the flame stretch. The second refers to development of a hybrid turbulent reaction rate model that is capable to account for the effects of turbulence without the need of an empirical correlation. This second approach was able to reduce the number of adjustable constants by introducing the fractal concept to the physical modelling of the flame front.

1.1 General objective

This work proposes an improvement of the reaction rate models implemented in the in-house developed STOKES code. As the main general objective, we aim at reducing model dependency on the various adjustable constants, by introducing physical understanding of the phenomenon of flame propagation.

1.1.1 Specific objectives

- Develop a dynamic expression for the stretch factor;
- Relate the stretch factor to the flow velocity field;
- Reduce models dependence on adjustable constants and empirical correlations;

- Develop a model for the integral length scale of wrinkling based on the fractal concept.

2 Fundamental Concepts

Gas explosion is a fascinating phenomenon of great complexity, where a strong coupling between chemical reaction, molecular transport and turbulence take place. The speed at which the flame propagates is a matter of great importance because it is essentially related to the amount of heat release, overpressure peaks and thermal radiation effects.

Many of the underlying mechanisms in gas explosions are not yet fully understood and the relevance of researching in this field is continuously increasing, especially with the prospective use of hydrogen as an energy carrier (MOLKOV *et al.*, 2020; LIPATNIKOV *et al.*, 2018).

This section presents an overview of the fundamental concepts of gas explosions, in order to support further discussions and analyses of this work. Because we are interested in the safety aspects of gas explosions, a brief introduction to accidental gas explosions is provided. Focus is placed on the phenomenological mechanisms of premixed turbulent flames, which are the very essence of gas explosions. Finally, some relevant length scales of turbulence are presented.

2.1 Accidental gas explosions

When a flammable material is released into the atmosphere, a few accidental scenarios are likely to succeed. All accidental scenarios of fire or explosion depend on whether the ignition occurs immediately or after some time (delayed ignition). In the case of an immediate ignition, fuel and oxidiser are not yet mixed, and a fire is expected. Gas explosions on the other hand, are the result of a delayed ignition, in which fuel and oxidiser form a flammable cloud before ignition takes place.

The consequences of a gas explosion may be influenced by many different factors, including

- type of fuel
- size and fuel concentration of the combustible cloud
- location and strength of ignition source
- turbulence levels before ignition, due to leaks or wind
- size, location and type of explosion vent areas
- location and size of structural elements and equipment

- mitigation schemes

Even small variations in these factors can significantly affect the gas explosion behaviour, making consequence estimation a very difficult task (ARNTZEN, 1998).

The overpressure effects are in general the most important aspect in the consequence analysis of gas explosions. It is the main mechanism to trigger even more destructive events (domino effect) (ECKHOFF, 2016). In process safety and loss prevention studies, accidental gas explosions are classified as a major hazard, along with fires and toxic releases (LEES, 2012). Predicting the behaviour of such events is crucial in many quantitative risk analyses, so that reliable means of prevention and mitigation can be proposed.

Turbulence is the governing factor of overpressure generation, as the increase of the propagation rates determines the degree of damage caused by the explosion (LI *et al.*, 2018). In this sense, the intensification of propagation rates by turbulence is a matter of great concern. The presence of obstacles ahead of the flame generates vorticity, intensifying turbulence and leading to faster propagation. In this sense, the occurrence of accidental gas explosions can be catastrophic in highly congested areas, such as those present in industrial process plants (ATKINSON; CUSCO, 2011; LI *et al.*, 2018).

2.2 Premixed turbulent combustion

From a phenomenological point of view, gas explosions are described as a premixed turbulent combustion. As opposed to non-premixed flames, a premixed flame presents the distinctive behaviour of propagation. This behaviour is characterised by the flame displacement in a direction normal to itself and towards the premixed reactants mixture, consuming them continuously as it moves (CANT; MASTORAKOS, 2008).

Propagation takes place thanks to a positive feedback mechanism, where a strong coupling between chemistry, molecular transport and turbulence occurs. The heat released from the combustion reaction increases the products temperature, causing the product gases to expand and creating high pressure and temperature gradients through the flame. Heat is then conducted forwards, preheating the unburned reactants, which enhances mass transport towards the flame. The pressure gradient also pushes the flame ahead, accelerating the conversion of reactants into products and contributing to start the process all over again (POINSOT; VEYNANTE, 2005).

The effect of turbulence on the flame propagation has been extensively described according to Damköhler first and second hypotheses (DAMKöHLER, 1940). In these, turbulence acts to enhance flame propagation in a two-fold manner: (1) by wrinkling the surface of an initially laminar flame and (2) enhancing molecular transport of heat and mass through the flame. The large length scales of turbulence would mainly increase the

flame surface area by wrinkling, whereas the small turbulence scales would amplify the molecular transport through the flame (NIVARTI; CANT, 2017).

Although both of these mechanisms operate together to enhance combustion, wrinkling of the flame surface is the predominant mechanism by which turbulence enhances the flame propagation (NIVARTI; CANT, 2017). This understanding forms the basis of the widely known laminar flamelet concept, which describes a turbulent flame surface as being composed by many small laminar flamelets.

The vast majority of the combustion models for the premixed turbulent flame is based on the laminar flamelet concept. As the concept emerges from Damköhler's first hypothesis, the models generally relate the turbulent reaction rate (or turbulent flame speed) to the wrinkled flame surface. This concept provides the useful relationship

$$u_T A_L = u_L A_T \tag{2.1}$$

where u_T is the turbulent flame speed, A_L is the cross-sectional area, u_L is the laminar burning rate and A_T is the surface area of the wrinkled laminar flame.

However, turbulence increases flame propagation up to a certain point, after which the turbulent flame speed starts to decrease. At sufficiently high turbulence intensities, flame propagation is inhibited, which can eventually lead to flame quenching due to the effects of stretch. This is known as the bending effect, as a reference to what is observed in the curve trend relating the increase in turbulence intensity to the variation of the turbulent flame speed (CANT; MASTORAKOS, 2008).

The effects of stretch were later included in Damköhler's first hypothesis (Equation 2.1) to give the following expression

$$\frac{u_T}{u_L} = I_0 \frac{A_T}{A_L} \tag{2.2}$$

where I_0 is a factor to account for the local mean rates of strain and curvature (NIVARTI, 2017).

For many years, this effect was believed to occur due to the localised disruption of the flame surface, where turbulence would affect the local integrity of the flame. However, recent Direct Numerical Simulation (DNS) data suggest that the bending effect may rise from a kinetic response of the flame rather than structural instability. According to the work of Nivarti & Cant (2017), the bending effect may occur regardless of the local flame quenching.

The turbulence-flame interaction defines different regimes of flame propagation. These are commonly summarised in regime diagrams (also called Borghi diagram) with the help of dimensionless numbers, such as the Reynolds number (Re), the turbulence Damköhler number (Da), and the Karlovitz number (Ka) which can be defined in terms

of the reaction zone thickness (Ka_δ). Figure 2.1 shows the Borghi diagram, where the turbulence length scale L_{turb} normalised by the laminar flame thickness (δ_L) is plotted along the $x-$axis and the turbulence intensity (u') normalised by the laminar flame speed (u_L) is plotted along the $y-$axis.

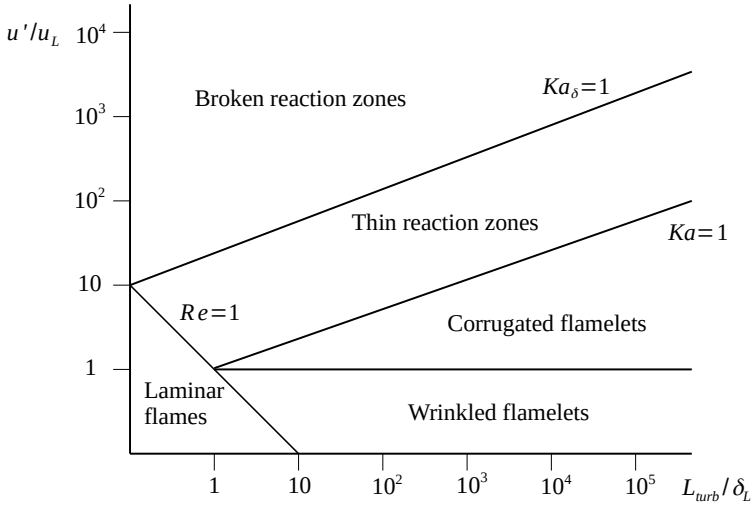

Figure 2.1: A modified Borghi diagram for the regimes of flame propagation. Adapted from Cant & Mastorakos (2008).

The diagram defines the the following regimes of propagation:

- *Laminar flamelet regime*: moderately strong turbulence, with fast chemistry and low strain rates;
- *Corrugated flamelet regime*: higher turbulence intensity causing strong flamelet winkling;
- *Thin reaction zones*: flame structure starts to loose stability due to the entrance of turbulent eddies;
- *Broken reaction zones*: significant local extinction under high turbulence intensity.

The definition of propagation regimes are essential to determine the range of validity of models for the premixed turbulent flame (POINSOT; VEYNANTE, 2005). For instance, a model that describes propagation in the flamelet regime would be fundamentally different from a model dedicated to represent the propagation phenomenon within the regime of broken reaction zone.

Recently, the long-established Damköhler's hypotheses have been revised with the aid of DNS data. The work of Chakraborty *et al.* (2019) suggests that the proportionality between the turbulent flame speed and the flame surface does not follow Damköhler's first hypothesis for turbulent Bunsen burner flames. Also, recent insights on the bending

effect contradicts Damköhler's second hypothesis, which may not always enhance molecular transport (NIVARTI; CANT, 2017), and appears to be valid only in a specific range of the thin reaction zone regime (AHMED *et al.*, 2020).

2.2.1 Flame instabilities

Landau-Darrieus instability

The propagating flame front of a premixed combustion is intrinsically unstable due to many gasdynamic effects, which are associated with the thermal expansion of the combustion products. In the process, the flame front develops concave and convex parts which tend to accumulate heat differently, depending on whether the curvature points towards the reactants or the products region. This mechanism increases flame curvature and it is known as the Landau-Darrieus (LD) instability. The Landau-Darrieus instability can contribute to the increase of the flame speed with the flame radius, which has been incorporated in quasi-laminar burning velocity models to describe the initial stages of flame propagation (CICCARELLI; DOROFEEV, 2008; ARNTZEN, 1998).

Diffusive instabilities

In addition to the LD instability, where gas flows are unbalanced due to thermal expansion, the diffusive fluxes may also not be equivalent through the flame. Especially in cases where mass diffusivity is higher than thermal conduction (Lewis number $\mathrm{Le} < 1$), the local combustion temperature is increased behind the convex part of the flame front, and decreased in concave portions (CICCARELLI; DOROFEEV, 2008). This can generate preferential diffusion and thermal-diffusion instabilities, which accentuates flame curvature, leading to highly unstable flames with increased local burning rates (LIPATNIKOV *et al.*, 2018; FROUZAKIS *et al.*, 2015).

Instabilities and flame stretch

Flame stretch is created by the local rates of flame curvature as well as inhomogeneities of the upstream flow, commonly referred to as strain rates. The response of a premixed flame to stretch is strongly associated with the overall Lewis number of the reactant mixture. As previously mentioned, $\mathrm{Le} < 1$ can create preferential diffusion which has been reported to significantly influence the local rates of strain and curvature (CHAKRABORTY; CANT, 2011).

However, according to Lipatnikov *et al.* (2018), the problem of flame instability arising from non-unity Lewis number and preferential diffusion remains one of the major poorly resolved fundamental issues in combustion science. Because of that, the vast

majority of the numerical models of premixed turbulent flames either neglect the influence of Lewis number on turbulent burning rate or resort to empirical correlations.

Instabilities generated by confinement and obstructions

The presence of confinement and obstructions cause powerful instabilities which can strongly affect flame propagation. These instabilities include the Kelvin-Helmoltz instability, which is related to shear stresses, and the Rayleigh-Taylor instability that takes place when a low density fluid is accelerated towards a fluid with higher density. In compressible flows involving the presence of pressure waves, the Rayleigh-Taylor instability is referred to as the Richtmyer–Meshkov instability (CICCARELLI; DOROFEEV, 2008).

The Rayleigh-Taylor and Richtmyer–Meshkov instabilities are triggered when the flame is accelerated over an obstacle or through a vent. Recently, those have been explored both numerically and experimentally to investigate the deflagration-to-detonation transition (DDT), especially in premixed combustion of hydrogen-air mixtures that are prone to transit to a detonation regime (COATES *et al.*, 2019; DOUNIA *et al.*, 2019; CAI *et al.*, 2018; EMAMI *et al.*, 2015).

Generally speaking, the Landau-Darrieus and diffusive instabilities are considered to be weak in comparison with the Rayleigh-Taylor and Richtmyer–Meshkov instabilities. This is because the presence of obstacles is assumed to have greater contribution to flame acceleration due to the increase in the flame surface area. However, Landau-Darrieus and diffusive instabilities play an essential role in the early stages of propagation, or in cases of unconfined flames (CICCARELLI; DOROFEEV, 2008).

In CFD codes dedicated to the simulation of gas explosion in complex geometries, such as the commercial software FLACS (Gexcon) and the in-house developed STOKES (FERREIRA *et al.*, 2019; FERREIRA; VIANNA, 2019; FERREIRA; VIANNA, 2020), the modelled numerical flame is much thicker than the real flame. For this reason, the aforementioned flame instabilities have almost no effect on the numerical turbulent premixed flame (ARNTZEN, 1998).

To address this issue, a few models have been proposed (VIANNA; CANT, 2014; BIRKBY *et al.*, 2000; ARNTZEN, 1998). These models introduce a laminar burning velocity and/or a quasi-laminar enhancement factor in order to account for the effect of flame instabilities in the initial stages of propagation of a premixed turbulent flame.

2.2.2 The length scales of turbulence

"Big whorls have little whorls,
Which feed on their velocity;
And little whorls have lesser whorls,
And so on to viscosity."

- Richardson (1922)

The quote above refers to the concept of Richardson's energy cascade, which describes a continuous process of kinetic energy transfer from the large length scales down to the smaller ones (DAVIDSON, 2015). In the process, viscosity plays no part as the largest length scales break-up successively into finer and finer structures.

Following this concept, turbulent time and length scales have been incorporated in the modelling of premixed turbulent flames so as to represent the effects of turbulence on the flame surface. The most relevant turbulent length scales to the premixed turbulent combustion modelling are the integral length scale (L_{turb}), the Taylor microscale (λ_T), the Gibson length scale (l_G), and the Kolmogorov length scale (η_K).

The integral length scale corresponds to the largest eddy of the energy cascade, from which the energy dissipation starts. It can be defined as

$$L_{turb} = \frac{k^{3/2}}{\varepsilon} \tag{2.3}$$

where k is the turbulent kinetic energy, and ε is the kinetic energy dissipation rate. As it will be shown, some flamelet models assume the largest length scale of flamelet wrinkling to be of the order of L_{turb}.

The Gibson length scale was introduced by Peters (1986) as the turbulent eddy with circumferential velocity equal to the flamelet velocity, as in

$$l_G = \frac{(u_L^o)^3}{\varepsilon} \tag{2.4}$$

where u_L^o is the unstrained laminar burning velocity.

The Kolmogorov length scale refers to the smallest possible existing eddy in the energy dissipation cascade, after which kinetic energy is dissipated by the fluid viscosity. It can be defined as

$$\eta_K = \left(\frac{\nu^3}{\varepsilon}\right)^{1/4} \tag{2.5}$$

where ν is the cinematic viscosity of the fluid. In the context of premixed turbulent combustion, one of the most important applications of η_K is to evaluate the validation of the laminar flamelet concept. The concept remains valid if the flame thickness is smaller than the smallest length scale in the turbulent flow, that is, the Kolmogorov length scale (PETERS, 1986).

The definition of the Taylor microscale is less straightforward and will not be shown here for the sake of brevity. The Taylor microscale can be used to define a modified version of the Karlovitz number to be used in demarcations of propagation regime diagrams (CANT; MASTORAKOS, 2008).

The Gibson length scale (Equation 2.4) is described as the length scale of turbulence having a minimum turnover velocity capable of wrinkling the flame surface.

That is, eddies smaller than l_G (but larger than η_K) will not wrinkle the flame front. Because of that, l_G has the character of a lower cut-off scale. This property of the l_G scale will be used in the context of fractal dimensions, which will be discussed in Section 3.1. Furthermore, the flame stretch effects are said to be more efficient at the l_G scale, where differential diffusion at non-unity Lewis numbers would affect flame speed (PETERS, 1986).

3 Numerical modelling

A real combustion reaction may involve hundreds of intermediate species as well as hundreds of elementary reversible reactions. This poses a significant challenge to the numerical modelling of combustion reactions, due to current limitations of computational resources.

Despite recent advances in Direct Numerical Simulations (DNS) with detailed reaction mechanisms, where dozens of species transport equations are solved (LAI *et al.*, 2018; BELL *et al.*, 2002), this task remains prohibitive for most problems of practical applications. Moreover, the highly non-linear relation between the production of species mass fractions and temperature makes the reaction rate modelling based on the Arrhenius law even more computationally expensive.

In the numerical modelling of premixed turbulent combustion, this issue is generally addressed assuming that the time scale of turbulence is much larger than the chemical time scale (Damköhler's number $Da \gg 1$). This allows for the assumption that the process in mainly controlled by turbulence, which has given rise to several modelling approaches for the mean turbulent reaction rate. Most of reaction rate closures for premixed turbulent flames are based on the physical analysis of the turbulence-flame interaction rather than the Arrhenius law (POINSOT; VEYNANTE, 2005).

One of the widely used models for the mean turbulent reaction rate is the Eddy Break-Up (EBU) model (SPALDING, 1977). This approach completely neglects the role of chemistry, assuming the flame surface to be infinitely thin and hence the reaction rate to be solely controlled by turbulence. Similar approaches, which are based on infinitely fast chemistry such as the Eddy Dissipation Concept (EDC), are known for having a common deficiency to predict unphysically large reaction rates in the proximity of walls.

Flamelet models are instead based on the structure of the wrinkled surface of the flame, which is assumed to be thin but not infinitely thin. These approaches mainly invoke Damköhler's first hypothesis (Equation 2.1) to develop the concept of Flame Surface Density (FSD) Σ, also called the flame surface area to volume ratio, defined as

$$A_T = \int_V \Sigma \mathrm{d}V \tag{3.1}$$

which can be replaced in Equation 2.1 to give (NIVARTI; CANT, 2017)

$$\frac{u_T}{u_L} = I_0 \frac{1}{A_L} \int_V \Sigma \mathrm{d}V \tag{3.2}$$

The calculation of Σ can be performed by algebraic expressions (BRAY *et al.*,

1984), stochastic approaches (POLE; CHENG, 1988), correlations (ZIMONT; BATTAGLIA, 2006) and fractal theories (LINDSTEDT; VAOS, 1999). Differential equations are also used in other approaches to predict Σ and further details can be found in the review of Driscoll (2008).

The following sections are focused on reviewing examples of algebraic, fractal-based and correlation models, which are relevant to the discussions of the present work.

3.1 Turbulent flame speed

Empirical correlations

A direct description of premixed turbulent flames is given in terms of the global turbulent flame speed u_T. Empirical correlations have been proposed to relate u_T to the turbulence intensity u', leading to expressions of the form (ABDEL-GAYED *et al.*, 1987)

$$\frac{u_T}{u_L} = 1 + C\left(\frac{u'}{u_L}\right)^n \tag{3.3}$$

where n is a model constant which is experimentally determined, and C depends on the integral length scale L_{turb} and the flame thickness δ_L. Plots of the normalised flame speed against the turbulence intensity follow the form of Equation 3.3, where the bending effect can be observed (CANT; MASTORAKOS, 2008).

Fractal models

Fractal theories have also been used to directly represent u_T. Following Damköhler 's first hypothesis and under the assumption that the turbulent flame surface can be geometrically represented by a fractal, Gouldin (1987) introduces the following expression

$$\frac{u_T}{u_L} \simeq \frac{A_T}{A_L} \simeq \left(\frac{\varepsilon_o}{\varepsilon_i}\right)^{D_f - 2} \tag{3.4}$$

where Damköhler's area ratio A_T/A_L is expressed as the ratio between the fractal outer cutoff ε_o and an inner cutoff ε_i, subjected to a power law relation with the fractal dimension *Df*. The outer and inner fractal cutoffs are related respectively to the upper and lower bounds of flame wrinkling, as the result of the interaction between the length scales of turbulence and the flame surface.

The maximum length scale of flame wrinkling is commonly taken as the integral length scale of turbulence $\varepsilon_o \simeq L_{turb}$, whereas the minimum length of wrinkling is found to be estimated as the flamelet thickness δ_L, the Kolmogorov length scale η_K, the Taylor microscale λ_T, and the Gibson length scale l_G (CHEN; MANSOUR, 2003; KULKARNI;

BISETTI, 2020).

Bray (1990) incorporated the fractal concept to model the flame surface density Σ by means of the flame wrinkle factor W

$$W = \int_{-\infty}^{\infty} \Sigma dx = \left(\frac{L_{turb}}{l_G} \right)^{D_f - 2} \tag{3.5}$$

where the integral length scale of turbulence L_{turb} and the Gibson length scale l_G are taken respectively as the outer and inner fractal cutoffs.

The work of Lindstedt & Vaos (1999) proposes a fractal-based approach for the reaction rate closure where the following expression for Σ is derived

$$\langle \Sigma \rangle \propto \frac{1}{L_{turb}} \left(\frac{\eta_K}{L_{turb}} \right)^{2 - D_f} \widetilde{c}(1 - \widetilde{c}) \tag{3.6}$$

where the Kolmogorov length scale η_K is taken as the fractal inner cutoff. This model was later extended in the work of (ALURI *et al.*, 2006) to account for high pressure conditions and Lewis number effects.

3.2 The Bray-Moss-Libby model (BML)

The BML combustion model is one of the most popular formulations applied to the modelling premixed turbulent flames within the flamelet regime. Under the assumption that the flame is a thin interface, the mass fractions of species and temperatures may be expressed as a function of a single reaction progress variable c, which can be defined in terms of the fuel mass fraction (Y_F) as

$$c = \frac{Y_F - Y_{FR}}{Y_{FP} - Y_{FR}} \tag{3.7}$$

where Y_F is the fuel mass fraction and the subscripts R and P refer to reactant and product states respectively, giving $c = 0$ in the unburned gases (reactants) and $c = 1$ in the fully-burned product gases (BIRKBY *et al.*, 2000). Any values lying in the range $0 < c < 1$ characterise the flame region.

The BML formulation is based on the idea that a fixed probe located inside the flame brush will detect reactants for some time and products for almost the rest of the time. Since the flamelet is thin, reacting gas ($0 < c < 1$) is detected only for short intervals. This physical argument is used for developing a probability density function (pdf) for c (CANT; MASTORAKOS, 2008).

The Favre-averaged (density-weighted) form of the transport equation for c is

given

$$\frac{\partial}{\partial t}\overline{\rho}\widetilde{c}+\nabla\cdot(\overline{\rho}\widetilde{\mathbf{u}}\widetilde{c})=\overline{w}-\nabla\cdot(\overline{\rho\mathbf{u}''c''})+\overline{\nabla\cdot(\rho D_c\nabla c)} \tag{3.8}$$

where $\overline{\rho}$ is density, $\widetilde{\mathbf{u}}$ is the vector velocity, $\overline{w}$ is the source term, D_c is the transport coefficient, and ∇ is the nabla operator. The tilde refers to a Favre density weighted average value. The more conventional Reynolds average is denoted by an overbar (BIRKBY *et al.*, 2000).

In Equation 3.8, the two terms on the left hand side are respectively the transient term, and the convective term and the three terms on the right hand side are the reaction rate term, the so-called Reynolds fluxes, and the average effect of molecular transport of c. All three terms on the right hand side are unclosed and require modelling (CANT; MASTORAKOS, 2008).

In the right hand side of Equation 3.8, the last term is commonly omitted under the assumption of high Reynolds number, where effects of molecular transport are weak. The Reynolds fluxes term describes the turbulent transport of c, which is modelled as per the gradient transport by analogy with Fick's law.

Therefore, Equation 3.8 is re-written as shown by Birkby *et al.* (2000)

$$\frac{\partial}{\partial t}\overline{\rho}\widetilde{c}+\nabla\cdot(\overline{\rho}\widetilde{\mathbf{u}}\widetilde{c})=\nabla\cdot\left(\left(\frac{\mu+\mu_t}{\sigma_c}\right)\nabla\widetilde{c}\right)+\overline{w} \tag{3.9}$$

where μ is the fluid viscosity, μ_t is the eddy viscosity, the sum $(\mu+\mu_t)$ denotes the effective viscosity, and σ_c is the turbulent Schmidt number for the reaction progress variable.

The transport equation for the mixture fraction $\widetilde{F}$ (air and fuel) is expressed as

$$\frac{\partial}{\partial t}\overline{\rho}\widetilde{F}+\nabla\cdot(\overline{\rho}\widetilde{\mathbf{u}}\widetilde{F})=\nabla\cdot\left(\left(\frac{\mu+\mu_t}{\sigma_f}\right)\nabla\widetilde{F}\right) \tag{3.10}$$

where σ_t is the turbulent Schmidt number for the mixture fraction. Both σ_c and σ_t are assumed to be equal to 0.7 (FERREIRA, 2018).

In the BML combustion model, the main thermodynamic variables must be coupled to the reaction progress variable. Since in explosion phenomena the Mach number may not be always considered to be low, such link cannot be done under assumptions of constant enthalpy.

Therefore, an additional transport equation must be included to take into account the total energy $\widetilde{E}$ (CANT; BRAY, 1989)

$$\frac{\partial}{\partial t}\overline{\rho}\widetilde{E}+\nabla\cdot\overline{\rho}u\left(\widetilde{E}+\frac{\overline{P}}{\overline{\rho}}\right)=\nabla\cdot\left(\left(\frac{\mu+\mu_t}{\sigma_E}\right)\nabla\left(\widetilde{E}+\frac{\overline{P}}{\overline{\rho}}\right)\right)+\nabla\mathbf{u}\overline{\tau} \tag{3.11}$$

where the total energy $\widetilde{E}$ is defined as

$$\widetilde{E} = \widetilde{e} + \frac{1}{2}\widetilde{u}^2 + \widetilde{k} \tag{3.12}$$

where $\widetilde{e}$ is the internal energy, $\frac{1}{2}\widetilde{u}^2$ is the kinetic energy and $\widetilde{k}$ is the turbulent kinetic energy. The internal energy $\widetilde{e}$ is given by

$$\widetilde{e} = \int_{T_0}^{\widetilde{T}} C_v dT + H\left(Y_{FR}(1-\widetilde{c}) + Y_{FP}\widetilde{c}\right) \tag{3.13}$$

where $\widetilde{T}$ is the Favre-averaged temperature, C_v is the specific heat capacity at constant volume, H is the energy of combustion, and T_0 is the reference temperature.

An additional consequence of variable enthalpy is the dependence of the temperature in the burnt products on the reactant enthalpy at the time of the reaction (BIRKBY *et al.*, 2000). Thus, the density ($\overline{\rho}_P$) in the burned gas, which is constant for constant enthalpy flows, becomes a variable as does the heat release parameter (τ), which is defined as

$$\overline{\tau} = \left(\frac{\rho_R}{\overline{\rho}_P}\right) - 1 \tag{3.14}$$

The pressure $\overline{P}$ is obtained from a equation of state of ideal gas, valid for small changes in molar mass

$$\overline{P} = \frac{\overline{\rho} R \widetilde{T}}{\overline{W}_M} \tag{3.15}$$

where R is the universal gas constant, and $\overline{W}_M$ is the mean molar mass. The Favre mean temperature is given by

$$\widetilde{T} = \frac{\widetilde{e}}{C_{VP}} + T_R(1-\widetilde{c})\left(1 - \frac{C_{VR}}{C_{VP}}\right) - \frac{H}{C_{VP}}\left[(1-\widetilde{c})Y_{FR} + \widetilde{c}Y_{FP}\right] \tag{3.16}$$

and the mean molar mass $\overline{W}_M$ is

$$\overline{W}_M = \frac{W_R(1-\widetilde{c}) + W_P\widetilde{c}(1+\overline{\tau})}{1+\overline{\tau}\widetilde{c}} \tag{3.17}$$

The heat release parameter may then be related to the temperature according to the following equation (BIRKBY *et al.*, 2000)

$$\overline{\tau}\widetilde{c} = \frac{W_R}{W_P}\left[\left(\frac{\widetilde{T}}{T_R} - 1\right) + \left(\frac{W_P}{W_R} - 1\right)\widetilde{c}\right] \tag{3.18}$$

3.2.1 BML reaction rate model

The BML model for the mean turbulent reaction rate $\overline{w}$ introduces the approach of the flamelet crossing frequency. In the spatial variation of the model, the flamelet crossing frequency is the average number of flame crossings of a specified line per unit distance y along this line (BRAY *et al.*, 1989).

The line y is a contour along which the Reynolds-averaged $\overline{c}$ is constant in time. A graph of c against y will result in a square wave function, like a "random telegraph signal", as shown in Figure 3.1.

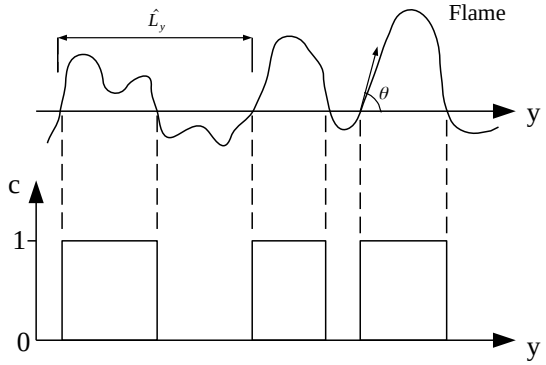

Figure 3.1: Variation of reaction progress variable c along a contour y. Adapted from Bray *et al.* (1989).

In the most familiar version of the mean reaction rate $\overline{w}$, the concept of the flamelet crossing frequency is given in terms of the flame surface density Σ, as in

$$\overline{w} = \rho_R u_L^o I_0 \Sigma \tag{3.19}$$

where ρ_R is the unburned reactants density, u_L^0 is the unstretched laminar burning velocity and I_0 is the stretch factor. An expression for Σ is then defined based on the flamelet crossing frequency analysis, giving

$$\Sigma = \frac{g\overline{c}(1-\overline{c})}{\left|\widehat{\sigma}_y\right|\widehat{L}_y} \tag{3.20}$$

where g is a model constant, $\left|\widehat{\sigma}_y\right| = |\cos\theta|$ is the flamelet orientation factor, and $\hat{L}_y$ is the integral length of flamelet wrinkling, which is also referred to as the mean flame length scale (see Figure 3.1) (POINSOT; VEYNANTE, 2005).

The constant g and $\left|\widehat{\sigma}_y\right|$ are determined experimentally, whereas the integral length of wrinkling $\hat{L}_y$ is determined empirically as

$$\hat{L}_y = c_L L_{turb} \left(\frac{u_L^o}{u'}\right)^n \tag{3.21}$$

where L_{turb} is the integral length scale of turbulence, c_L and n are model constants, which arguably take values of the order of unity.

The influence of turbulence on the mean burning rate is contained in the two last terms of Equation 3.19, namely the stretch factor I_0 and the turbulent area to volume ratio Σ, where $\hat{L}_y$ is the characteristic length scale which controls Σ (BRAY, 1990).

3.2.2 The stretch factor I_0

The mean flame stretch factor I_0 is introduced in the expression of the mean turbulent reaction rate $\overline{w}$ in order to account for the local rates of strain and curvature. As revised in Section 2.2.1, straining arises from the effects of convection within the flow surrounding the flame, whereas curvature is generated by the flame propagation itself. Figure 3.2 shows an illustration of the effects of flame stretch on the flame surface due to local strain and curvature.

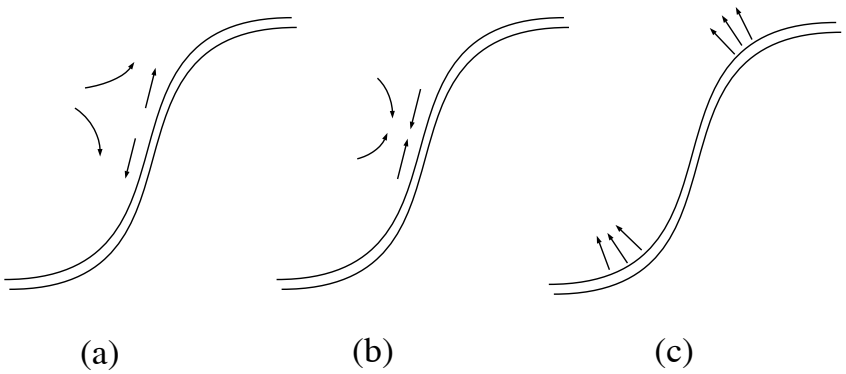

Figure 3.2: Local effects of strain and curvature on the surface of the flame. (a) positive straining; (b) negative straining; (c) concave and convex curvatures. Adapted from Cant & Mastorakos (2008).

The response of a laminar premixed flame to stretch effects is strongly influenced by the magnitude of the overall Lewis number of the reactants mixture, which is the ratio of the thermal diffusivity α to the mass diffusivity D ($Le = \alpha/D$). The effects of non-unity Lewis number become more significant in non-stoichiometric lean premixed flames, where flame curvature can be greatly affected by preferential diffusion. Generally, in stoichiometric mixtures, a $Le \simeq 1$ is considered and the effects of curvature are commonly neglected, under the assumption that turbulence acts to "even out" convex and concave curvatures (CANT; MASTORAKOS, 2008).

The effects of stretch would lead to either an increase or a decrease in the local burning rate and strong stretch can lead to flame extinction (BRAY *et al.*, 1989). The mathematical concept of flame stretch was introduced as the fractional rate of change of

flame surface area $\dot{s} = (1/A)(\mathrm{d}A/\mathrm{d}t)$, which was later defined as

$$\dot{s} = \frac{1}{A}\frac{\mathrm{d}A}{\mathrm{d}t} = a_T + u_d h_m \tag{3.22}$$

where a_T is the local tangential strain rate, h_m is the mean curvature of the surface, u_d is the displacement speed, and $u_d h_m$ is the local propagation rate (NIVARTI, 2017). The local rates a_T and h_m are given by

$$a_T = \nabla \cdot u = \left(\delta_{ij} - N_i N_j\right)\frac{\partial u_i}{\partial x_j} \tag{3.23}$$

$$h_m = \frac{1}{2}\left(h_1 + h_2\right) = \frac{1}{2}\nabla N \tag{3.24}$$

where $\nabla \cdot u$ is the divergence of velocity in surface coordinates, N is the local normal vector pointed into the reactants, h_1 and h_2 are the two main curvatures. A planar laminar flame can undergo straining effects by a divergent local flow field, creating points of inward and outward fluxes (CANT; MASTORAKOS, 2008).

The displacement speed u_d is a kinematic quantity defined by Poinsot *et al.* (1991) as the speed at which the cold side of the flame front moves along its normal with respect to the flow of unburned reactants. The laminar flame speed u_L is a thermochemical quantity, related to the consumption speed of the flame. For a planar unstrained flame $u_d = u_L = u_L^o$ (BRAY *et al.*, 1989).

An expression for the stretch factor I_0 is then related to the local tangential strain rate a_T and to the local mean curvature h_m as

$$I_0 = \int_{-\infty}^{\infty} \mathrm{d}a_T \int_{-\infty}^{\infty} \mathrm{d}h_m \frac{u_L(a_T, h_m)}{u_L^o} P(a_T, h_m) \tag{3.25}$$

where $P(a_T, h_m)$ is a joint pdf of a_T and h_m. DNS data has shown that a_T and h_m are negatively correlated, meaning that they contribute to the rate of change of flame surface area in an opposite manner (CANT; MASTORAKOS, 2008).

The work of Nivarti (2017) suggests that whereas the local tangential strain rate a_T contributes productively to Σ, the mean curvature h_m contributes destructively to Σ, especially under high turbulence intensities. This provided a new insight on the flame bending effect, which is given as the result of a balance between a_T and h_m, leading to a regulation of the flame surface area. This changes the general belief that the bending effect is the result of local flame disruption caused mainly by straining (NIVARTI; CANT, 2017).

A few algebraic approaches have been proposed to calculate I_0. Bray (1990)

suggests an expression where I_0 is modelled as a function of the Karlovitz number Ka as

$$I_0 = \frac{0.117}{(1+\tau)} Ka^{-0.784} x \tag{3.26}$$

which is a correlation obtained from experimental data (ABDEL-GAYED *et al.*, 1987) and is restricted to applications where $Ka > 6.6 \cdot 10^{-3}$. Later, Bray & Cant (1991) proposed an expression for I_0 based both on the Karlovitz and the Markstein number Ma. From parameterisation of DNS data the following equation is proposed

$$I_0 = 1 - 2k_c MaKa^{\frac{1}{2}} \tag{3.27}$$

where the numerical value of k_c is not known.

Chakraborty *et al.* (2019) uses DNS of turbulent Bunsen burner flames to investigate the validity of Damköhler's first hypothesis, which does not hold well on the account of a non-unity stretch factor. His work suggests that the stretch factor is given by the ratio

$$I_0 = \frac{\overline{\rho u_d}}{\rho_0 u_L} \tag{3.28}$$

where ρ_0 is the unburned reactant density. However, his work highlights the difficulty in high-fidelity modelling the flame displacement speed $\overline{\rho u_d}$. This difficult often lead to the approximation $\overline{\rho u_d} = \rho_0 u_L$ which retrieves the original Damköhler's first hypothesis, with $I_0 = 1$.

Nevertheless, in most formulations under low levels of stretch, the stretch factor is taken as a constant parameter and $I_0 \lesssim 1$ (NIVARTI; CANT, 2017).

3.2.3 Correlations of Abu-Orf & Cant (2000) for u_L^o and $\hat{L}_y$

The unstrained laminar burning velocity u_L^o

The ratio $u_L(a_T, h_m)/u_L^o$ (Equation 3.26) between the local laminar burning velocity to the unstrained planar laminar burning velocity may be obtained from flamelet libraries of stretched laminar flamelet solutions, which include detailed chemistry mechanism and molecular transport processes (BRAY; CANT, 1991).

Alternatively, experimental data can be parameterised using a set of correlation functions to generate expressions for computing u_L^o without the need of using the computationally expensive flamelet libraries. One such parameterisation was developed by Abu-Orf & Cant (2000) to give the following expression

$$u_L^o = a\Phi^b e^{-c(\Phi-d)^2} \left(\frac{T_R}{T_0}\right)^{\alpha} \left(\frac{P}{P_0}\right)^{\beta} \tag{3.29}$$

where $a, b, c, d, \alpha, \beta$ are fuel-dependent constants presented in Table 3.1 for methane and propane, Φ is the equivalence ratio, T_R and P are respectively the reactants temperature and pressure, P_0 is the reference pressure, and T_0 is the reference temperature.

Table 3.1: Values of the constants for the laminar flame speed correlation in Equation 3.29 (BIRKBY *et al.*, 2000).

Fuel	a	b	c	d	α	β
Methane (CH_4)	0.6097	–2.554	7.3105	1.2303	2.0	–0.42
Propane (C_3H_8)	0.4342	0.7345	4.5003	0.9813	1.77	–0.25

Assuming that the effects of positive and negative curvatures tend to cancel out on average of the flame surface, a simple linear correlation for the effects of tangential strain rate is given by

$$\frac{u_L(a_T)}{u_L^0} = 1 - a_T t_a, \quad 0 \leq a_T < a_{T\max} \tag{3.30}$$

$$\frac{u_L(a_T)}{u_L^0} = 0 \quad \text{otherwise} \tag{3.31}$$

where t_a is the time scale for straining (CANT; MASTORAKOS, 2008).

The integral length scale of wrinkling $\hat{L}_y$

The importance of a precise closure for $\hat{L}_y$ have been emphasised (BRAY *et al.*, 1989; SHY *et al.*, 1996; CHANG *et al.*, 2001) so that the influence of turbulence on the mean reaction rate can be realistically represented. Equation (3.21) is the initially proposed model for $\hat{L}_y$ based on empirical observations (CHEW *et al.*, 1990). Later, it was found to produce excessively high reaction rates near solid walls due to the direct dependency on L_{turb}.

The work of Abu-Orf & Cant (2000) introduces an alternative model for the characteristic length of wrinkling

$$\hat{L}_y = c_L \delta_L f\left(\frac{u'}{u_L^0}\right) \tag{3.32}$$

where the explicit dependence of L_{turb} from Equation (3.21) is replaced by the laminar flamelet thickness δ_L, defined as

$$\delta_L = \frac{\nu}{u_L^0} \tag{3.33}$$

where ν is the unburned reactants density. According to Birkby *et al.* (2000), δ_L is the diffusive length scale associated with the internal structure and hence the maximum curvature of the laminar flamelet.

The effects of turbulence are accounted via the function f which is an empirical correlation of the form

$$f\left(\frac{u'}{u_L^o}\right) = \left[\left(\frac{1}{1+\frac{C_{w1}}{(u'/u_L^o)}}\right)\left(1-\exp\left[-\frac{1}{1+C_{w2}(u'/u_L^o)}\right]\right)\right]^{-1} \tag{3.34}$$

where C_{w1} and C_{w2} are empirically-determined constants.

As revised elsewhere (BIRKBY *et al.*, 2000), Equation 3.34 seeks to include the bending effect of the turbulent flame speed under high turbulence intensities, also predicting realistic behaviour of reaction rates near walls. Moreover, the purpose of function f is to quantify $\hat{L}_y$ uniquely for the turbulent flame, which is based on the assumption that the turbulent flame will select its own length scale in response to perturbations from the turbulent velocity fields.

3.3 Models for the initial laminar phase

The initial stages of propagation are very much influenced by the intrinsic flame instabilities mentioned in Section 2.2.1. In order to be able to capture such instabilities, a very fine mesh would be required, which is computationally prohibitive especially when the simulation of explosions in complex geometries are of interest.

This issue is addressed by proposing models for the initial laminar burning rate, as the one proposed by Birkby *et al.* (2000)

$$\overline{w}_{lam} = \rho_R u_L C A_{flame} \frac{\widetilde{c}(1-\widetilde{c})}{\Sigma_{nodes}\widetilde{c}(1-\widetilde{c})V} \tag{3.35}$$

where C is a constant taken as $C = 4.2$ for methane, V is the volume of the computational cell, and A_{flame} is the laminar flame surface area, given by

$$A_{flame} = \frac{2}{3}A^{1/2} \tag{3.36}$$

where A is the surface area of the cell. The model was initially developed on the basis of a statistical approach for a 2D triangular adaptive mesh.

Later, A_{flame} was adapted for 3D tetrahedral (VIANNA; CANT, 2014; VIANNA; CANT, 2010) and 3D hexahedral meshes (FERREIRA; VIANNA, 2019), assuming the form of

$$A_{flame} = c_{LAM} V^{2/3} \tag{3.37}$$

where $c_{LAM} = 4/9$. Equation 3.37 is also obtained on a geometric basis for spherical flames where V is the volume of the computational cell in which the progress variable is equal to 0.5.

The work of Vianna & Cant (2014) introduces a blending function to account for the transition from the laminar to the turbulent regime of propagation. The blending function is given by

$$f_\mu = \max\left(0; 1 - \exp\left(-0.008\left(\mathrm{Re}_{\mathrm{turb}} - \mathrm{Re}_{\mathrm{Th}}\right)\right)\right) \tag{3.38}$$

where Re_{turb} is the turbulent Reynolds number and $\mathrm{Re}_{\mathrm{Th}}$ is a threshold value of the turbulent Reynolds number. The $\mathrm{Re}_{\mathrm{Th}}$ value inserts a condition to determine whether the reaction rate will be calculated by the laminar burning model or the turbulent model. This is determined by the expression

$$\overline{w} = f_\mu w_{turb} + \left(1 - f_\mu\right) w_{lam} \tag{3.39}$$

where w_{turb} is the turbulent reaction rate model and w_{lam} is the laminar reaction rate model. For values of Re_{turb} below $\mathrm{Re}_{\mathrm{Th}}$, the function f_μ tends to zero, and the mean reaction rate is given by the laminar model. On the other hand, in regions of the flow where $\mathrm{Re}_{turb} > \mathrm{Re}_{\mathrm{Th}}$, f_μ is close to unity and the turbulent reaction rate model is considered.

4 CFD tool: STOKES

The CFD tool STOKES (*Shock Towards Kinetic Explosion Simulator*) is an in-house developed 3D Navier-Stokes code that has been designed for the simulation of turbulent reacting flows in complex geometries (FERREIRA *et al.*, 2019; FERREIRA; VIANNA, 2019; FERREIRA; VIANNA, 2020).

The code couples the finite volume discretisation method and the Gilbert Johnson Keerthi algorithm for the construction of a porous mesh that is able to account for small obstacles of the geometry, without the need of substantial mesh refinement (FERREIRA *et al.*, 2019).

In the Porosity Distributed Resistance (PDR) method, porosity values are assigned to faces and volumes of each computational cell and must be considered in each conservation equation of the generic differential form

$$\frac{\partial(\rho\phi)}{\partial t} + \frac{\partial\left(\rho u_j \phi\right)}{\partial x_j} = \frac{\partial}{\partial x_j}\left(\Gamma_\phi \frac{\partial \phi}{\partial x_j}\right) + S_\phi \tag{4.1}$$

where ρ is density, u_j is the velocity component in the x_j direction, Γ_ϕ is the transport coefficient, ϕ denotes any variable to be transported in the flow, and S_ϕ is the source term. In STOKES, seven transport equations are solved for each node of the domain, where ϕ becomes mass, energy, momentum, the progress variable c, fuel fraction, k and ε.

The calculated porosity values β are incorporated in the volume-integrated equations, giving the parameterised version of the transport equations of the form

$$\int_V \frac{\partial(\rho\phi)}{\partial t}\beta_V dV = -\int_S \left(\rho u_j \phi\right)\beta_j dS_j + \int_S \Gamma_\phi \frac{\partial \phi}{\partial x_j}\beta_j dS_j + \int_V S_\phi \beta_V dV \tag{4.2}$$

where β_V is the porosity of the cell volume, and β_j is the porosity of the cell face in the j direction.

A modified Lax-Friedrichs method central difference scheme is applied, with the use of an artificial viscosity for smoothing numerical oscillations. Smoothing is performed by means of the smooth factor (SF), which is determined in the setup. The discretised equations are time-marched with a fourth-order Runge-Kutta method. Further details of the code can be found elsewhere (FERREIRA, 2018; FERREIRA *et al.*, 2019; FERREIRA; VIANNA, 2019; FERREIRA; VIANNA, 2020)

4.1 Turbulence model

The governing equations of the turbulent flow are solved considering the Reynolds-Averaged Navier-Stokes (RANS) approach, where the variables of the flow are solved as mean quantities, following Reynolds' decomposition $\phi = \overline{\phi} + \phi'$. Turbulence is closed using the eddy viscosity μ_T concept according to the Boussinesq hypothesis. The two-equation $k-\varepsilon$ model is used to calculate the turbulent eddy viscosity as

$$\mu_T = C_\mu \rho \frac{k^2}{\varepsilon} \tag{4.3}$$

where C_μ is a model constant taken as 0.09.

4.2 Resistance to the flow

The presence of small-scale obstacles that are not solved by the mesh creates additional resistance to the flow, which also contributes to the generation of turbulence. These effects are incorporated as additional source terms in the transport equations of momentum, k and ε.

In the momentum equation, an additional source term (R_j) is included to account for the resistance that unresolved obstacles offer to the mean flow

$$\frac{\partial}{\partial t}(\beta_v \rho \mathrm{u}) + \mathrm{u} \cdot \nabla \left(\beta_j \rho \mathrm{u}\right) = \beta_v \rho g - \beta_v \nabla P + \left[\beta_j \nabla \cdot \tau\right] + R_j \tag{4.4}$$

where R_j is modelled as frictional resistance, as in

$$R_j = -f_j A_w \frac{1}{2} \rho U_j^2 \tag{4.5}$$

where R_j is the frictional resistance in the j direction, f_j is the friction factor, A_w is the wetted area per unit volume ($A_w = A_i \left(\beta^{-1} - 1.0\right)^2$), and U_j is the velocity component in the j direction (VIANNA; CANT, 2010).

The friction factor is calculated differently depending on the orientation of the flow. For flows parallel to the obstacle, f_j is given by

$$f_j = 0.048 Re_D^{-0.2} \tag{4.6}$$

where Re_D is the Reynolds number based on the hydraulic diameter. For flows normal to the obstacle, f_j is calculated by

$$f_j = 0.23 + \frac{0.11}{\left[\left(3\frac{P}{D}\right)^{0.5} - 1\right]^{1.08}} Re_D^{-0.15} \tag{4.7}$$

where D represents the diameter of an obstacle and P is the space between the obstacles (FERREIRA *et al.*, 2019).

The additional turbulence production due to the presence of shear layers S_{k1} and wake effects S_{k2} are accounted for by the following expressions

$$S_{k1} = C_S \mu_{eff} \beta_v \left[(U - U_S)^2 + (V - V_S)^2 + (W - W_S)^2 \right] A_w^2 \tag{4.8}$$

$$S_{k2} = C_B \rho U_j^3 A_w \tag{4.9}$$

where C_S and C_B are model constants which take values of 2.0 and 1.0 respectively, μ_{eff} is the effective viscosity, U, V and W are the velocity components in the x, y and z directions, U_S, V_S and W_S are the effective slip velocities, which are normally taken to be a fraction of the fluid velocity.

The additional turbulence production terms described S_{k1} and S_{k2} are introduced in the source term of the transport equations of both k and ε, giving (FERREIRA *et al.*, 2019; VIANNA; CANT, 2010)

$$\frac{\partial}{\partial t}(\rho\varepsilon) + \nabla \cdot (\rho \mathbf{u} \varepsilon) = \nabla \cdot \left(\left(\mu + \frac{\mu_t}{\sigma_\varepsilon} \right) \nabla \varepsilon \right) + \frac{\varepsilon}{k} (C_{1\varepsilon} f_1 S_T - C_{2\varepsilon} f_2 \rho \varepsilon) \tag{4.10}$$

$$\frac{\partial}{\partial t}(\rho k) + \nabla \cdot (\rho \mathrm{u} k) = \nabla \cdot \left(\left(\mu + \frac{\mu_t}{\sigma_k} \right) \nabla k \right) + S_T - \rho \varepsilon \tag{4.11}$$

where S_T is the source of turbulence production, defined as

$$S_T = 2\mu_t E_{i,j} E_{i,j} + S_{k1} + S_{k2} \tag{4.12}$$

where $\mu_t E_{i,j} E_{i,j}$ represents the turbulence production due to viscous forces and $\rho\varepsilon$ is the viscous dissipation. For further information on the implemented turbulence and PDR models the reader should refer to the work of Ferreira (2018).

4.3 Combustion model

The combustion model implemented in STOKES follows the BML formulation described in Section 3.2. Here we describe some of the models and assumptions implemented in STOKES in its original formulation which has been introduced by the work of Ferreira (2018), Ferreira & Vianna (2020).

A simplified one-step irreversible reaction is considered (i.e. Reactants $\longrightarrow$ Products), which is further reduced to the transport of the reaction progress variable c. The mean turbulent reaction rate is modelled according to the thin flamelet approach of the BML model (Equation 3.19).

The effects of flame stretch are disregarded in STOKES as originally conceived, by assigning the stretch factor as a constant parameter and equals unity $I_0 = 1$. By doing this, the mean local rates of strain and curvature are accordingly neglected (FERREIRA; VIANNA, 2019).

Furthermore, in STOKES original formulation, the integral length scale of flame wrinkling $\hat{L}_y$ is calculated by means of the empirical correlation proposed by Abu-Orf & Cant (2000) (Equation 3.32).

In this sense, replacing the assumption of $I_0 = 1$ and the model for $\hat{L}_y$ in Equation 3.19, the mean turbulent reaction rate is calculated in STOKES by the following expression

$$\overline{w} = \rho_R u_L^o \frac{g\tilde{c}(1-\tilde{c})}{\left|\widehat{\sigma}_y\right|} \frac{1}{c_L \delta_L} \left[\left(\frac{1}{1 + C_{w1}(u'/u_L^o)} \right) \left(1 - \exp\left[-\frac{1}{1 + C_{w2}(u'/u_L^o)} \right] \right) \right] \tag{4.13}$$

where the unstrained laminar burning velocity u_L^o is calculated by the correlation in Equation 3.29, which is also proposed by Abu-Orf & Cant (2000).

4.3.1 Initial laminar burning model

The early stages of propagation are modelled in STOKES with the laminar burning model proposed by Birkby *et al.* (2000) (Equation 3.35), where the laminar flame area A_{flame} is modelled by the expression proposed by Vianna & Cant (2014)

$$A_{flame} = \frac{4}{9} V^{2/3} \tag{4.14}$$

The transition from the laminar burning to the turbulent burning regimes of propagation is determined by the blending function shown in Equation 3.38, where the transition is taken to occur at $\mathrm{Re}_{\mathrm{Th}} = 500$, giving

$$f_\mu = \max\left(0; 1 - \exp\left(-0.008\left(\mathrm{Re}_{\mathrm{turb}} - 500\right)\right)\right) \tag{4.15}$$

which is implemented in Equation 3.39 to calculate the mean reaction rate. In practice, the flame is constrained to burn at the laminar flame speed until the threshold value of the turbulent Reynolds number is reached.

4.3.2 Constants of combustion models

The presence of a large number of adjustable constants and empirical coefficients is a common characteristic of flamelet models. Most of these constants are empirically-determined, such as g and $\left|\widehat{\sigma}_y\right|$ in the BML model, and C_{w1} and C_{w2} in the Abu-Orf & Cant (2000) correlation.

The original STOKES code takes $g = 1.5$ and $\left|\widehat{\sigma}_y\right| = 0.5$ as suggested by Cant & Mastorakos (2008). However, the experimental work of Chang *et al.* (2001) suggest that such values may vary within a specified range. With respect to the constant c_L, in STOKES simulations c_L is left to be calibrated for each simulation case. This means that for each new case, c_L is manually changed in the setup file. Even though many works suggest c_L to be of the order of unity, a large range of $0.23 < c_L < 12.3$ has been reported (RANASINGHE; MALALASEKERA, 2017). Finally, C_{w1} and C_{w2} are taken respectively 1.5 and 4.0, as reported by Abu-Orf & Cant (2000).

In the laminar burning model, there are also two constants that require attention. The first is the constant C in Equation 3.29, which is taken in STOKES as 4.2 as reported by Birkby *et al.* (2000) for methane. In the lack of available data, this constant is kept unchanged for other fuels such as propane. The second constant is called in this work as c_{LAM}, and it is assigned the value of $4/9 \approx 0.44$ in Equation 4.14. Table 4.1 provides a summary of the combustion model constants originally implemented in STOKES as well as the threshold value of turbulent Reynolds number.

Table 4.1: Values of constants and parameters of the combustion models originally implemented in STOKES.

	C	c_{LAM}	g	$\lvert\hat{\sigma}_y\rvert$	C_{w1}	C_{w2}	$\mathrm{Re}_{\mathrm{Th}}$
STOKES	4.2	4/9	0.5	1.5	1.5	4.0	500

However, the various constants of the combustion models are in line with the solution of the reacting flow field where, in general, a refined mesh is required to capture the shear layers around obstacles. In the porosity distributed resistance (PDR) model, the obstacles are represented by a porous mesh, where additional terms of frictional resistance and turbulence generation are appended to the momentum equations. Therefore, there seems to be no guarantee that the reported constants of the combustion modelling hold, meaning that additional tuning may be necessary to cope with the PDR approach.

4.4 Ignition model

Ignition starts by initialising a predefined ignition region (ignition radius) where the reaction progress variable is ramped to the value of 1. At the ignition point, the value of $c = 1.0$ is maintained for a specified period of time (ignition time). The presence of products increases the temperature and decreases the density and hence a flow is induced in front of the flame and the combustion process is initialised (FERREIRA, 2018). Both ignition radius and time are defined in the setup.

4.5 Output files

The output files of the code are generated with a `.vtk` extension to be read and visualised in the open-source program ParaView. The `.vtk` files contain information on the flow solution, including the velocity field, the reaction progress variable, the pressure field, temperature, density, k and ε, the fuel fraction, and the dimensionless numbers (turbulent Reynolds number, Damköhler number, Karlovitz number and Mach number). In the setup file of the code, it is possible to choose the frequency of generation of an output file.

5 Methodology

This work is focused on the analysis and improvement of the combustion models originally implemented in STOKES. Two issues were initially considered, with the first referring to the effects of flame stretch, which were originally disregarded by assigning $I_0 = 1$; and the second being the limitation imposed by the large number of constants of the turbulent reaction rate model, which require tuning.

In order to address these issues, two pragmatic approaches were initially proposed, so as to:

1. develop a dynamic stretch factor to incorporate the effects of flame stretch due to strain - the "BML-dynamic-I_0" approach;
2. reduce the number of adjustable constants of the combustion model by replacing the Abu-Orf & Cant (2000)'s empirical correlation - the "BML-hybrid" approach.

Over the course of time, interesting observations on the flame sensitivity to the initial laminar phase model raised another important issue to be studied. This was addressed within the context of the BML-hybrid, as it will be shown in the following sections.

5.1 The BML-dynamic-I_0: a dynamic stretch factor

Bray & Cant (1991) draws attention to the fact that the stretch factor I_0 is generally different from unity because of the influences of strain and curvature on laminar flames in turbulent flow. Ideally, I_0 should be calculated dynamically with the flow and account for both of these contributions. Proposed models for I_0 found in literature (Equations 3.26 and 3.27) emerge from semi-empirical correlations which introduce even more adjustable constants as well as other uncertainties.

Moreover, even in recent sophisticated DNS investigations (CHAKRABORTY *et al.*, 2019) the difficulty of accurately determining the stretch factor as (Equation 3.28) still remains. Such difficulties are related with the complexity of the joint pdf (Equation 3.26) which correlates the tangential strain rates and curvature.

With this in mind and considering that in low levels of stretch $I_0 \lesssim 1$ (NIVARTI; CANT, 2017), an expression for a dynamic stretch factor is proposed. Considering a stoichiometric fuel-air mixture with $Le = 1$, we neglect the effects of stretch due to curvature and assume that stretch is caused mainly by strain. In this sense, Equation 3.22 is rewritten

$$\dot{s} = \frac{1}{A}\frac{\mathrm{d}A}{\mathrm{d}t} = a_T \tag{5.1}$$

Accordingly, we take the definition of Equation 3.23 to calculate a dynamic stretch factor I_0 based on the local divergence of velocity. The reasoning line is that the divergence of velocity contributes to flame stretching the same way the divergence affects the flow, by representing points of both outward and inward fluxes on the surface of the flame, causing stretch. The proposed dynamic stretch factor is given by a simple algebraic expression of the form

$$I_o = \frac{|\nabla \cdot v|}{\max|\nabla \cdot v|} \tag{5.2}$$

where $|\nabla \cdot v|$ is the absolute value of the divergence of velocity in the flame region $0 < c < 1$, and $\max|\nabla \cdot v|$ is the maximum absolute value of the divergence of velocity from the previous iteration.

The proposed dynamic stretch factor (Equation 5.2) is intended to account for low levels of stretch, where $I_0 \lesssim 1$. Also, it was assumed that positive and negative curvatures cancel out on the average. In the light of this, the I_0 is calculated dynamically in every node identified as the flame region, by normalising the local divergence with the maximum value of the divergence of velocity.

The proposed model for a dynamic I_0 in Equation 5.2 is implemented in Equation 4.13 to obtain a modified expression for the mean turbulent reaction rate in STOKES

$$\overline{w} = \rho_R u_L^o \left(\frac{|\nabla \cdot v|}{\max|\nabla \cdot v|}\right) \frac{g\tilde{c}(1-\tilde{c})}{|\widehat{\sigma}_y|} \frac{1}{c_L \delta_L} \left[\left(\frac{1}{1+\frac{C_{w1}}{(u'/u_L^o)}}\right)\left(1-\exp\left[-\frac{1}{1+C_{w2}(u'/u_L^o)}\right]\right)\right] \tag{5.3}$$

where the unstrained laminar velocity u_L^o is calculated by Equation 3.29. Equation 5.3 is hereafter referred to as the BML-dynamic-I_0 model.

In this approach, all the constants and parameters were taken as the values shown in Table 4.1, with the exception of the c_L constant. In each case study, a fixed value of c_L was set in order to strictly evaluate the effect of the proposed BML-dynamic-I_0.

Results will be compared with experimental data from literature, FLACS simulations and with the "BML-original", which refers to STOKES simulations using the originally implemented combustion model, with $I_0 = 1.0$.

5.2 The BML-hybrid: a fractal-based length of wrinkling $\hat{L}_y$

This second investigation line is conducted independently, with the main purpose of accounting for the effects of turbulence to the reaction rate by means of the length scale of wrinkling $\hat{L}_y$, without the use of an empirical correlation.

We aim at introducing the physical understanding that the surface of the flame

is wrinkled by a range of turbulent eddies of different sizes which are assumed to be of the same order of magnitude of the flame characteristic length of wrinkling $\hat{L}_y$. This concept is related to the assumption that the wrinkled flame front can be geometrically represented by a fractal, as shown in Figure 5.1. In this sense, considering the fractal formulation presented in Equation 3.4, $\hat{L}_y$ can be modelled as the fractal approach, as in

$$\hat{L}_y \propto \left(\frac{\varepsilon_o}{\varepsilon_i}\right)^{Df-2} \propto \left(\frac{L_{turb}}{l_G}\right)^{Df-2} \tag{5.4}$$

where the outer fractal cutoff ε_o is taken as the integral length scale of turbulence L_{turb}, and the inner fractal cutoff ε_i is assumed to be of the order of the Gibson length scale l_G, as indicated in Figure 5.1. The fractal dimension Df is taken as $7/3$, which is equivalent to $n = 1$ in the originally proposed model for $\hat{L}_y$ (Equation 3.21) (BRAY, 1990).

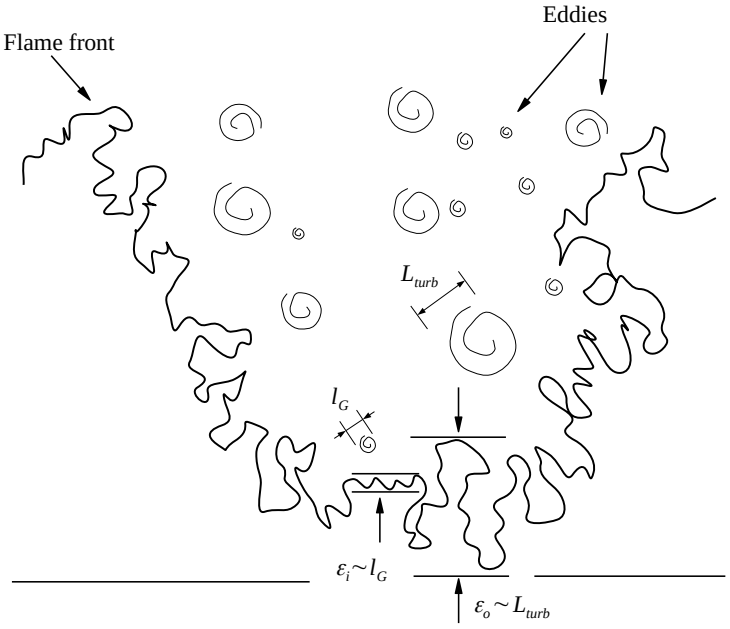

Figure 5.1: Schematic representation of a fractal flame front that is wrinkled by turbulent eddies of different length scales. Adapted from Gouldin *et al.* (1989).

As opposed to what is introduced in the fractal-based model proposed by Lindstedt & Vaos (1999), where vortices of all sizes between the integral and the Kolmogorov length scale contribute to the wrinkling of the flame surface, here we consider that the minimum length scale of turbulence capable of wrinkling the flame is the Gibson length scale (PETERS, 1989). This fractal-based range of wrinkling from l_G to L_{turb} is also in line with what was proposed by Bray (1990) to model Σ as the wrinkling factor W (Equation 3.5).

In this sense, we propose a modification in the model of $\hat{L}_y$ proposed by Abu-Orf & Cant (2000) by replacing the empirical correlation for the function $f(u'/u_L^o)$ (Equation

3.34) by the fractal approach presented in Equation 5.4. A fractal-based approach for $\hat{L}_y$ is proposed as

$$\hat{L}_y = c_L \delta_L \left(\frac{L_{turb}}{l_G} \right)^{D_f - 2} \tag{5.5}$$

where the dependence on the flame thickness δ_L (Equation 3.33) is maintained.

The proposed expression for the integral length scale of wrinkling (Equation 5.5) is implemented in the expression for the flame surface density Σ (Equation 3.20), which is in turn used to calculate the mean turbulent reaction rate by the BML model (Equation 3.19) as

$$\overline{w} = \rho_R u_L^o \frac{g\tilde{c}(1-\tilde{c})}{\left|\widehat{\sigma}_y\right|} \frac{1}{c_L \delta_L} \left(\frac{L_{turb}}{l_G} \right)^{2 - D_f} \tag{5.6}$$

where the unstrained laminar velocity u_L^o is calculated by Equation 3.29.

Equation 5.6 is called the BML-hybrid and it is implemented in STOKES to eliminate the need for the empirical correlation (Equation 3.34) to be used.

Within the BML-hybrid approach, an investigation of the flame response to different values of the constant c_L, and parameters of the laminar burning model, namely c_{LAM} and $\mathrm{Re_{Th}}$ were extensively conducted, leading to new calibrated values.

STOKES simulations using the BML-hybrid will be compared with experimental measurements from literature, FLACS simulations, and STOKES simulations with the originally implemented combustion model. This will be called the "BML-Abu-Orf" model, as a reference to the Abu-Orf correlation (Equation 3.34) which is used to model $\hat{L}_y$. This version also refers to a constant stretch factor equals to unity $I_0 = 1.0$.

5.3 Case studies

In order to evaluate the performance of the proposed models, a few case studies are considered. The case studies are separated in two categories, with the first referring to partially confined combustion chambers of relatively small sizes, and the second referring to a semi-confined geometry, representing a typical chemical process module of large-scale dimensions. This section is focused on describing those cases, presenting the fuel-air mixture considered and some parameters applied to each case.

5.3.1 Combustion chambers

Three partially obstructed combustion chambers of relatively small sizes are considered. Chambers 1, 2 and 3 are depicted in the Figure 5.2a, 5.2b, and 5.2c, respectively. Their walls are fully closed with the exception of their upper end, which remains open. Ignition is placed at the bottom end of the chambers, as indicated by the red point in the Figure 5.2.

The solid surface boundary condition is applied to the chamber walls, where zero normal fluxes of mass, momentum and energy are imposed. The turbulent kinetic energy and the normal gradient of dissipation rate are also taken as zero on the surfaces. The Outflow boundary condition is set on the chambers open upper ends, where the static pressure is specified and the other variables are extrapolated from interior points (FERREIRA, 2018). Pressure and temperature of reference are taken respectively as 100 kPa and 300 K.

The chambers have been described previously in the works of Gubba *et al.* (2011) (Chamber 1), Ibrahim *et al.* (2009), Kent *et al.* (2005) (Chamber 2), and Patel *et al.* (2002) and Sarli *et al.* (2009) (Chamber 3). Their works are used as benchmarks for the evaluation of the results obtained from STOKES simulation applying the proposed BML-hybrid and the BML-dynamic-I_0 models for the calculation of the mean reaction rate.

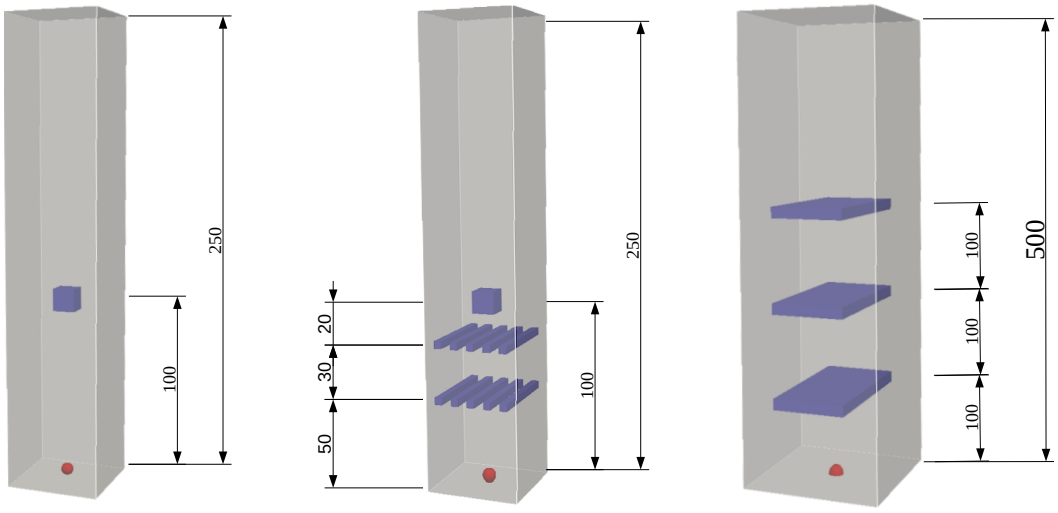

(a) Chamber 1 (b) Chamber 2 (c) Chamber 3

Figure 5.2: Combustion chambers used as case studies. The chambers have a square cross section of (a) 50 x 50 mm in Chamber 1; (b) 50 x 50 mm in Chamber 2; and (c) 150 x 150 mm in Chamber 3. Units of the indicated lengths are in millimetres.

The dimensions of Chamber 1 are 50 x 50 x 250 mm, and it is initially filled with a stoichiometric mixture of propane and air. It is partially obstructed by a solid square obstacle (12 x 12 mm cross section) whose base is 94 mm away from the bottom end of the chamber (GUBBA *et al.*, 2011).

Chamber 2 differs from Chamber 1 only by the presence of two additional turbulent generating baffle plates. Each baffle plate contains 5 bars of 3 x 4 x 50 mm each, separated by a distance of 5 mm from each other. The baffle stations are located at 50 mm and 80 mm from the bottom end, and therefore they are 30 mm apart (IBRAHIM *et al.*, 2009).

Chamber 3 is twice as long as Chambers 1 and 2 and it is filled with a mixture

of methane and air at stoichiometric proportions, before ignition starts. Its dimensions are of 150 x 150 x 500 mm, where three rectangular obstacles of 12 x 75 x 150 mm each are positioned at 100-mm spacings within the chamber (PATEL *et al.*, 2002; SARLI *et al.*, 2009).

For the simulation setup of all combustion chambers, the Courant—Friedrichs—Lewy number (CFL) is taken as 0.4, and the smooth factor (SF) was taken equally as 0.05. A 0.001 m of mesh spacing (Δx) in all directions is considered in Chambers 1 and 2. For Chamber 3, the mesh gap is 0.002 m in all directions. Table 5.1 presents a summary of those values.

Table 5.1: Mesh spacing and numerical methods parameters for the simulation setup of Chambers 1, 2 and 3 using STOKES.

	CFL	SF	$\Delta x(m)$
Chambers 1 and 2	0.4	0.05	0.001
Chamber 3	0.4	0.05	0.002

5.3.2 Chemical process module

The fourth case study is shown in Figure 5.3 and it consists of a chemical process module of large-scale dimensions. A similar module configuration has been described previously by Silgado-Correa *et al.* (2020b), Silgado-Correa *et al.* (2020a) and Ferreira & Vianna (2020). Silgado-Correa *et al.* (2020a), Silgado-Correa *et al.* (2020b) used a similar configuration to study volume prediction of flammable gas clouds, whereas Ferreira & Vianna (2020) investigated gas explosion simulations by comparing STOKES results with FLACS.

In the present work, the module geometry is considered to evaluate the capability of the proposed models to predict flame behaviour in the absence of walls. As opposed to the cases of the combustion chambers where the wall proximity might influence the flame advance, the process module case is placed in an open area where a flammable region is defined. Moreover, this configuration allows for the investigation of flame prediction in a more realistic accidental gas explosion scenario, due to the fact that its large dimensions resembles the actual size of industrial process units.

The module has external dimensions of 24 x 48 x 59 m, as presented in Figure 5.3 where the green area represents the flammable region of 18432 m^3 (24 x 48 x 15 m), where a stoichiometric mixture of methane and air is defined. The green area in Figure 5.3 is obtained by plotting the iso-surface of the fuel fraction in the beginning of the simulation using ParaView.

In the simulation setup of the process module, the CFL number is taken as 0.1, and the smooth factor (SF) was taken as 0.9. After having conducted preliminary tests with mesh spacings of 0.75, 0.65, 0.55 and 0.50 m, the 0.50 m was considered the least

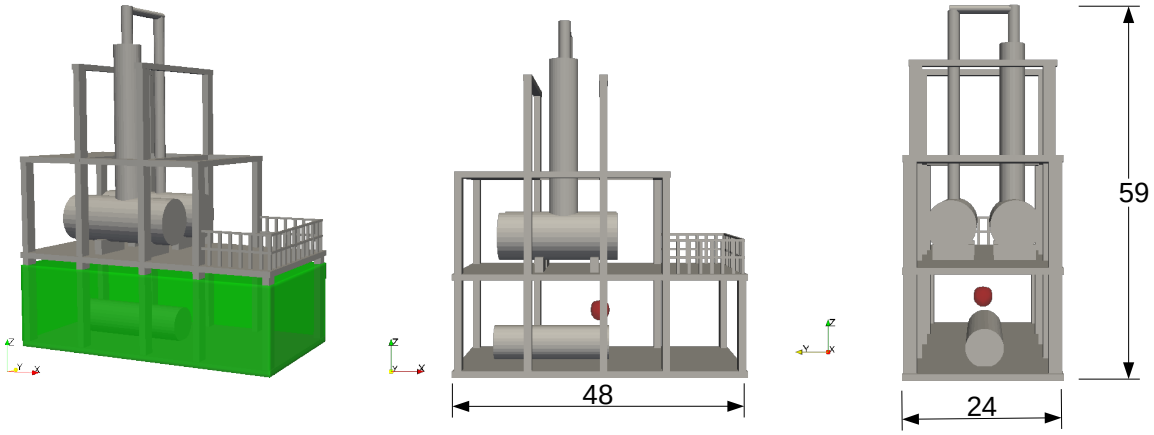

Figure 5.3: Chemical process module with large scale dimensions. The flammable region is represented by the green area. Ignition is indicated by the red point. Units of the indicated lengths are in metres.

possible gap length (Δx) in all directions that could be run in a domain of 170 x 110 x 65 m (Figure 5.4), considering the current computational resources. The values of CFL, SF and Δx applied to the simulation of the chemical process module are presented in Table 5.2.

Table 5.2: Mesh spacing and numerical methods parameters for the simulation setup of the chemical process module using STOKES.

	CFL	SF	$\Delta x(m)$
Chemical process module	0.1	0.9	0.50

Adequate grid independence tests could not be performed, because changes in grid sizes presented a high dependence on CFL and SF numbers, in such a way that numbers shown in Table 5.2 of SF and CFL could not be reproduced for different mesh sizes.

Since the module geometry is located in an open area, the outflow boundary condition is applied to every domain boundary, with the exception of the floor where the solid surface condition is imposed. In the Outflow condition, the static pressure is specified and the other variables are extrapolated from interior points, whereas in the solid surface condition all fluxes are set to zero. Pressure and temperature of reference are taken respectively as 100 kPa and 300 K.

5.4 Estimating flame position and flame speed

The simulation results are normally evaluated on the basis of: (1) the flame position plotted against time; (2) the flame speed plotted against time or (3) the flame speed plotted against the chamber axial distance, (4) the overpressure plotted against time and (5) the rendered flame contours.

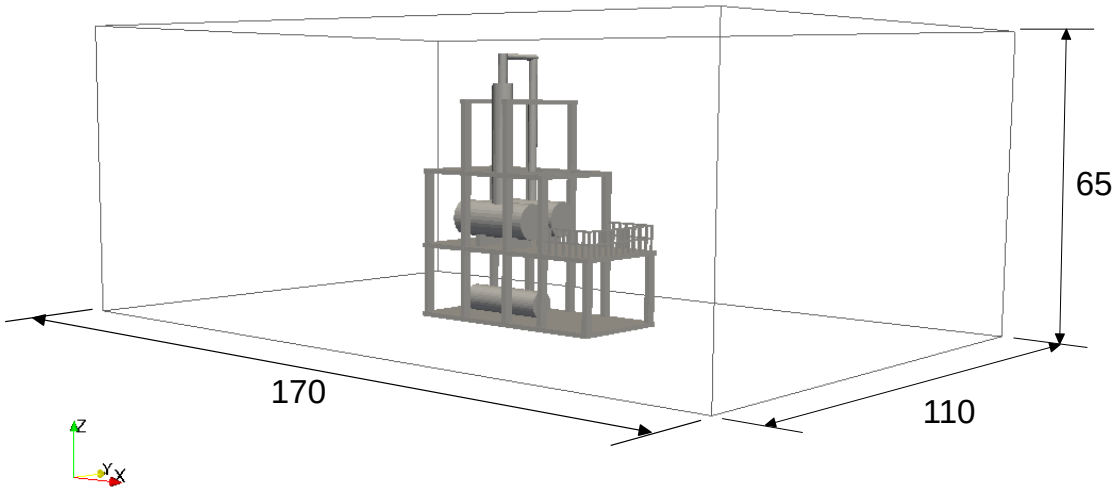

Figure 5.4: Dimensions in metres of the computational domain used in the simulation of gas explosion in the chemical process module case.

In the first version of STOKES, the flame position used to be estimated by means of the ParaView program. With the help of the "Plot Over Line" tool in ParaView, the flame position used to be identified manually, by trying to position the tool arrow over the region of the domain where the reaction progress variable was approximately equals to 0.5, as shown in Figure 5.5.

It was necessary to keep changing the arrow coordinates in "Line Parameters" until the arrow reached the desired position. After that, the coordinate of the arrow in the direction parallel to the flame would be transferred to a spreadsheet, where the axis translation needed to be accounted to calculate the flame position at the corresponding time step. The flame speed was then calculated directly on the spreadsheet as the numerical derivative of the flame position in time.

This process had to be repeated at least 10 times for different time steps (output files) in order to obtain enough points that allowed for a consistent plot of flame position against time to be constructed. This method was therefore extremely time-consuming, not to mention the need of a large number of `.vtk` output files to be generated, which may compromise computer storage space. Moreover, since the estimation had to be performed manually, additional reading errors by the user could jeopardise the accuracy of the results.

In order to address this issue and aiming at making STOKES post-processing more efficient, an improvement in the estimation of flame position and speed is proposed. In this work, both the flame position and the flame speed are calculated directly in the STOKES code and the values are written in two separate output files, namely `flame_position` and `flame_speed`.

The flame position at each iteration is determined by tracking the longest

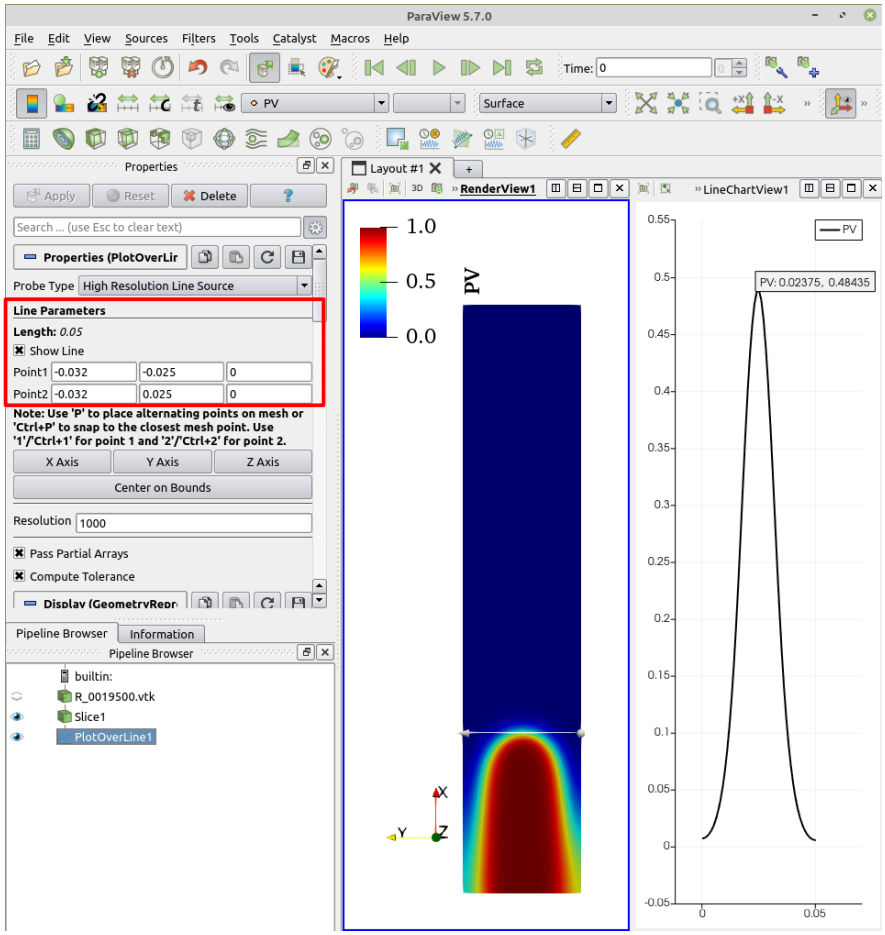

Figure 5.5: Method for estimating the flame position with ParaView in the first version of STOKES.

distance reached by the tip of the flame. A local variable is created to store the maximum value of the x coordinate of the nodes whose reaction progress variable values lie in the range where $0.1 < c < 0.9$, characterising the flame region. The generated output file `flame_position` contains four columns with information on the reaction progress variable, the iteration number, the flow time, and the flame position, respectively.

The flame speed is calculated considering the difference between the flame position at the current iteration and the flame position at the iteration when it was last changed, divided by the difference between the corresponding flow times. This strategy is applied instead of considering the difference between the flame position at the current iteration and the flame position at the previous iteration, because it was observed that the flame position can stay unchanged for many iterations, especially in the beginning of the propagation. The `flame_speed` file also contains four columns which respectively refer to the iteration number, the flow time, the flame position and the flame speed.

Both the flame position and flame speed are calculated in the `combustion.f90` subroutine, and the corresponding output files are opened in the `solver.f90` subroutine

before the iteration loop starts (see Appendix A). The plots are then generated with the graphing utility "gnuplot", where a script file is employed to make the process even easier. Appendix B provides a quick manual on how to run STOKES and additional packages.

The current method for estimating the flame position and flame speed histories directly from the code is a simple solution that allows simulation results to be plotted in a considerably easier manner. This approach represents an enormous advantage when compared to the previous laborious method using ParaView (Figure 5.5). Computer storage space is also spared, because a smaller number of `.vtk` files could be generated only for renderisation purposes. The size of a `.vtk` file normally ranges from 300 MB to 2 GB (depending on the number of elements), whereas the size of a `flame_position` file goes from 2 to 4 MB.

Also, this approach can motivate future code developers of STOKES to implement similar ways to account for the variation of other flow properties with time. One example is measuring the change of flame position in other directions (y and z) in unconfined geometries.

5.5 FLACS simulations

FLACS is a specialised CFD tool for safety applications, such as dispersion analysis and gas explosions (GEXCON, 2018). The software includes a 3D CFD code which relies on the Reynolds-Averaged Navier-Stokes (RANS) equations where the k-$\boldsymbol{\varepsilon}$ turbulence model is considered. Equations are solved on a structured Cartesian grid using a finite volume method, and the SIMPLE pressure algorithm is employed for the highly confined explosion simulation.

As with STOKES, FLACS also uses the distributed porosity concept for representing complex geometries on relatively coarse computational meshes. In this approach, large objects and walls are represented on-grid, whereas smaller objects are represented sub-grid. In simulations, the porosity field represents the local congestion and confinement and this allows sub-grid objects to contribute with flow resistance (drag), turbulence generation and flame folding in the simulations (GEXCON, 2018).

The model for premixed turbulent combustion in FLACS represents turbulent flame propagation as turbulent burning velocity, calculated from diffusion and reaction rate in the numerical flame zone. Coupling between chemical reactions and the local turbulence structures is achieved using the flamelet assumption, whereby the turbulent premixed combustion is represented by an array of laminar flame structures with a finite thickness embedded in the turbulent flow field. The combustion model is based on the flamelet correlation proposed by (BRAY, 1990) for turbulence burning velocity and the beta flame model developed by (ARNTZEN, 1998).

The commercial software FLACS v10.7 is applied in the present work to simulate

gas explosions in all of the case studies described in Section 5.3. These results will be later compared with the results obtained with STOKES.

In FLACS, the geometries and flammable regions of the combustion chambers and the chemical process module were reproduced as described previously. The EULER boundary condition is set to outflows, and the SYMMETRY boundary condition is chosen for ground floor boundaries. The same grid sizes as presented in Tables 5.1 and 5.2 are used in the flammable region. However, both uniform and stretched grids are used, where grid cells are stretched with an increment ratio of 20%.

6 Results and discussion

This chapter presents the simulation results obtained from the proposed models BML-dynamic-I_0 and BML-hybrid for the calculation of the mean turbulent reaction rate in STOKES. The BML-dynamic-I_0 model was tested in the three combustion chambers, whereas the BML-hybrid was tested in all of the three chambers as well as in the process module geometry presented in Section 5.3.

Simulation results obtained with the BML-dynamic-I_0 model are compared with the original version of STOKES as originally conceived, which is called the BML-original. Also, quantitative comparisons against literature (SARLI *et al.*, 2009) data are presented.

For the proposed BML-hybrid, simulation results are compared with the original version of STOKES, with FLACS simulations and with literature experimental data. The original version of STOKES is in this case called the BML-Abu-Orf, as a reference to the empirical correlation that is being replaced, and the stretch factor is assumed to be equals unity ($I_0 = 1.0$).

6.1 BML-dynamic-I_0

The proposed BML-dynamic-I_0 model was implemented in STOKES to simulate gas explosion inside Chambers 1, 2 and 3, which have been described in detail in Section 5.3.1. It is important to mention that in this analysis the only modification in the STOKES code is related to the insertion of the dynamic I_0 in the BML reaction rate model, as an attempt to account for flame stretch due to the effects of strain.

Simulation results are presented in Figure 6.1 where the flame contours are the rendered values of the reaction progress variable c, at different time steps. Results obtained with the BML-original model are shown in Figures 6.1a, 6.1b, 6.1c, whereas the results of the proposed BML-dynamic-I_0 model can be seen in Figures 6.1d, 6.1e, 6.1f.

The flame contours from the BML-original presented a good overall behaviour, where a distinct separation between the unburned reactants (black region, $c = 0$) and the burned products can be observed (white region, $c = 1$). On the other hand, the BML-dynamic-I_0 results show an unexpectedly enlarged flame region, represented by the red colour where $0 < c < 1$.

This is especially observed near the recirculation zones behind the obstacles and at the ignition point, where the turbulent flow field intensifies. This effect is stronger in Chamber 2 (Figure 6.1e), where significantly larger red regions are present due to the presence of two extra turbulent generating baffle plates.

This observations indicate that the proposed BML-dynamic-I_0 acts to diminish

the turbulent rate of reaction in the areas of the chambers where the turbulent flow field is more pronounced. Since the proposed dynamic stretch factor is given by a normalisation of the local divergence of velocity with the maximum divergence of velocity, it is expected that the stretch factor would be lowered by intense divergence and turbulent fields.

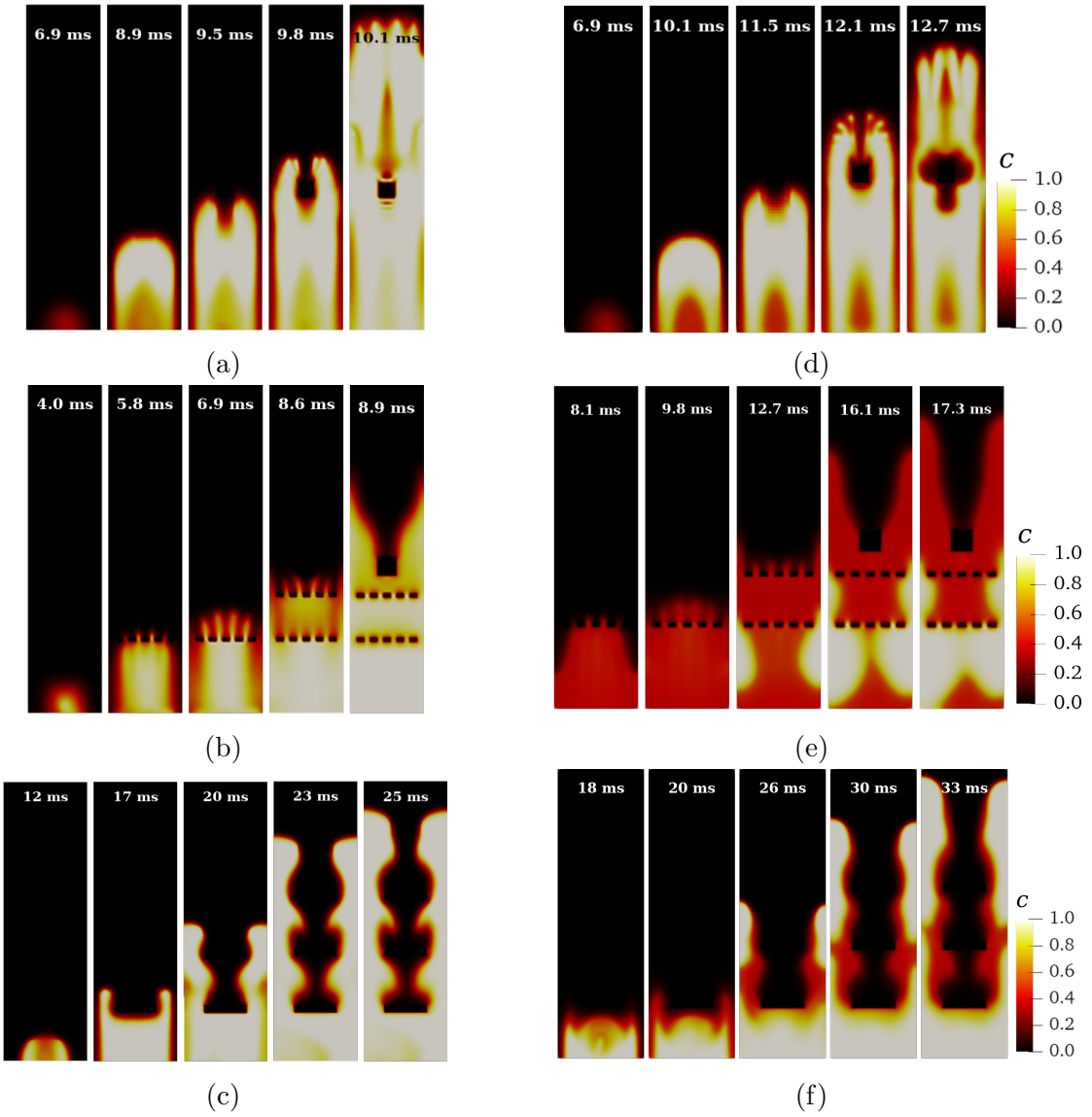

Figure 6.1: Flame contour at different time steps inside Chambers 1, 2 and 3 obtained with BML-original (a), (b), and (c); and using the proposed BML-dynamic-I_0 model (d), (e), and (f).

A physical interpretation of this observation could lead to the idea that the flame is under intense levels of strain in highly turbulent areas of the flow. However, this would not exactly agree with the recent DNS observations (NIVARTI, 2017), which has been discussed in Section 3.2.2, that stretch due to strain acts in fact to increase the flame surface density Σ. A decrease of Σ and hence the local mean burning rates, are instead on the account of the stretch due to curvature, which is neglected in the proposed BML-dynamic-I_0.

At this point it is important to remember that the BML turbulent burning model is only calculated in certain regions of the domain, where the local turbulent Reynolds number exceeds the threshold value of 500. Accordingly, since intense turbulent areas present high turbulent Reynolds numbers where the turbulent reaction rate is bound to be calculated, it is possible to affirm that the enlarged red zones in Figures 6.1d, 6.1e, 6.1f are due to the effect of a lowered turbulent rate of reaction because of the dynamic I_0.

A quantitative analysis of the flame time histories presented in Figure 6.1 was conducted in terms of flame position and flame speed. These can be observed in Figure 6.2, where it is clear that both models overestimate the flame time arrivals (Figures 6.2a, 6.2b, 6.2c) and speed (Figures 6.2d, 6.2e, 6.2f) for all three cases. The initial steps of the flame advance is poorly represented, and in all cases the flame position changes suddenly. However, some improvement on the overall flame time arrivals is attained by the BML-dynamic-I_0.

Plots of Chambers 1 and 2 (Figures 6.2a and 6.2b, respectively) present the two best results with the flame being delayed and getting closer to the experimental data. Nevertheless, no significant change in the curve trend is observed which reflects in nearly unchanged flame speed histories (Figures 6.2d, 6.2e).

In Chamber 2 (Figures 6.2b and 6.2e), both models struggled to capture the final flame acceleration in the presence of the cube. A slight improvement is obtained with the BML-dynamic-I_0, on the account of a clockwise inclination of the curve trend.

Flame position history in Chamber 3 (Figure 6.2c) shows an abnormal peak at around 0.015 seconds, which is probably caused by the flame retreat considering its track at $c = 0.1$. This greatly affects flame acceleration at the proximity of obstacles, as it can be seen in Figure 6.1f.

Therefore, it is clear that the proposed model to calculate the effects of stretch on the flame surface has contributed to reduce the flame advance in Chambers 1 and 2 despite additional loss in quality of the flame contour. However, with respect to the flame position and speed curve shapes, no perceptive improvement is achieved. Flame speed trend was in fact worsened in Chamber 3.

Furthermore, there seems to exist some inconsistencies on the physical argument used to the development of the BML-dynamic-I_0 based purely on strain leading to a local reduction of reaction rates. As previously discussed, in order to achieve a reduction on the reaction rate by inserting the effects of stretch, curvature should be taken into consideration.

In this sense, it is suggested that the normalisation of the divergence of velocity should be revised and future work may look into other approaches based perhaps on non-dimensional numbers of the flow, such as the local Lewis number, which has been proven to be greatly connected to the curvature effects.

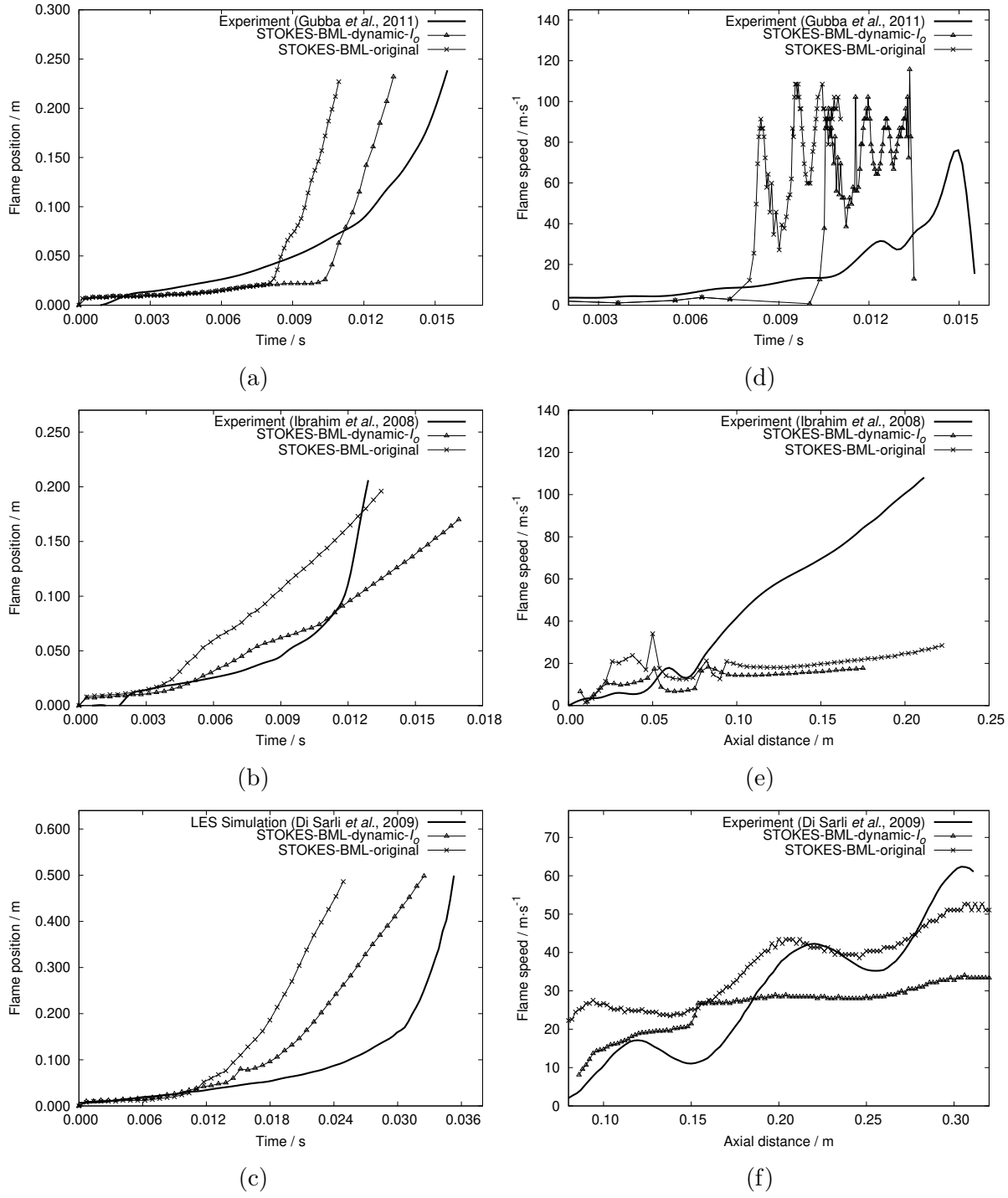

Figure 6.2: Flame position time histories inside Chamber 1 (a), Chamber 2 (b), and Chamber 3 (c); and flame speed plotted against time in Chamber 1 (d), and against the axial distance in Chamber 2 (e), and Chamber 3 (f).

6.2 BML-hybrid

In face of the limitations encountered with the proposed BML-dynamic-I_0 model, efforts were focused on the BML-hybrid approach. As it will be presented in this section, the BML-hybrid proved to be more reliable, allowing for further investigations on model constants.

Although the BML-hybrid was applied to all four geometries, namely the three combustion chambers and the process module (Section 5.3), Chambers 1 and 3 were chosen to evaluate flame response to variations in model constants.

In this sense, an extensive sensitivity analysis was performed in Chambers 1 and 3 considering variations in the constant c_L of the length of wrinkling $\hat{L}_y$ model, in c_{LAM} of the laminar burning model, and in $\mathrm{Re_{Th}}$ parameter, which determines the transition from the laminar to the turbulent propagation regimes.

6.2.1 Chamber 1

Varying constant c_L

The calibration of the constant c_L is generally the first step taken towards model evaluation in STOKES. The flame response to different values of c_L is presented in the Figure 6.3, where the analysis is conducted in terms of flame position (Figures 6.3a and 6.3d), flame speed 6.3b and 6.3e), and overpressure 6.3c and 6.3f). One should bear in mind that we investigate the models coupling with the porosity PDR model in which the boundary layer is not solved.

Figures 6.3a, 6.3b and 6.3c refer to the reaction rate model originally implemented in STOKES, namely the BML-Abu-Orf. These are compared with the results obtained from the proposed BML-hybrid model, which can be observed in the Figures 6.3d, 6.3e and 6.3f.

The graphs titles refer to the following: Geometry-Model-Reynolds threshold-Ignition radius- Ignition time-c_{LAM} constant-c_L constant. The overpressure values are taken by a monitoring point located at the chamber outlet, and flame position is obtained by tracking the longest distance reached by the iso-value $c = 0.1$ at each time step.

From the experimental data of the flame position time series, it can be noticed that the flame moves at a relatively small rate until it encounters the obstacle at 0.1 metre, after which it is accelerated. This effect can be better observed in the flame speed time history, where a first bump at approximately 0.013 seconds indicates the flame acceleration when approaching the obstacle, followed by a small speed loss when passing over it. At this moment, a maximum overpressure peak of 34 mbar is registered. The subsequent smaller overpressure peaks are due to the consume of trapped unburned reactants up and

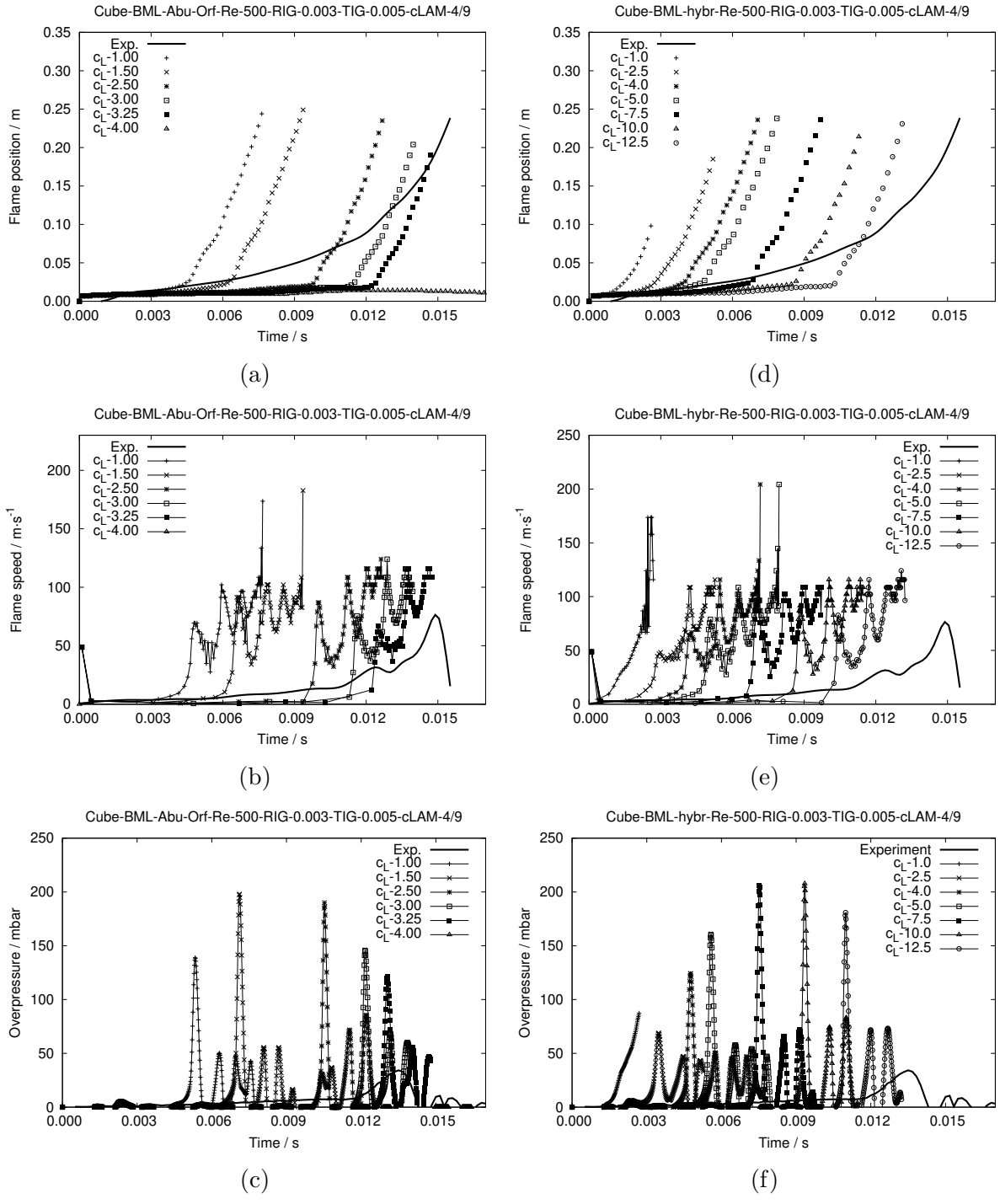

Figure 6.3: Variations of the c_L constant in the models BML-Abu-Orf (a; b; c) and BML-hybrid (d; e; f) in Chamber 1. (a) and (d) Flame position; (b) and (e) Flame speed; (c) and (f) Overpressure at the chamber outlet. Values of $\mathrm{Re_{Th}}$ and c_{LAM} are taken respectively as 500 and 4/9.

down stream of the solid obstacle (GUBBA *et al.*, 2011).

It can be noticed from Figures 6.3a and 6.3d that variations in the constant c_L do not significantly affect the shape of the flame time histories of both of the BML-Abu-Orf and BML-hybrid models. The flame moves at a very low rate in the early stages

of propagation, until it is suddenly accelerated. This behaviour deviates from what it is observed in the experimental data, in which the flame acceleration occurs gradually, in an exponential-like manner.

This is also observed in the flame speed time series of both models (Figures 6.3b and 6.3e). Since the flame speed is calculated as the rate of change of flame position, no significant change is observed in the shape of the flame speed curves Figures 6.3b and 6.3e. Therefore, increases in c_L act mainly to delay the moment at which the flame position (and speed) is significantly changed.

It would be expected that the more c_L is increased, the slower the flame would propagate, since c_L is inversely proportional to the mean reaction rate. This should consequently diminish the rate of energy release, leading to lower overpressure peaks. This relation can only be observed for c_L values lying in the range $1.5 < c_L < 3.25$ in the BML-Abu-Orf case. On the other hand, when c_L is changed from $c_L = 1.0$ to $c_L = 1.50$ or $c_L = 2.5$ an unexpected behaviour is observed, that is, the overpressure peaks rise with the increase of c_L.

When the same analysis is made for the BML-hybrid, similar deviations from the expected c_L-overpressure relation are observed (Figures 6.3d and 6.3f). For the range $1.0 < c_L < 10.0$, the overpressure increases unexpectedly with the increase of c_L. Moreover, although no significant change in overpressure prediction is noticed for changes in c_L from 7.5 to 10.0, an improvement is noticed when increasing the c_L value from 7.5 or 10.0 to 12.5, which leads to slightly smaller overpressure peaks.

The overall analysis of Figure 6.3 leads to a preliminary conclusion that both models, BML-Abu-Orf and BML-hybrid, overpredict the overpressure peaks for all the values of c_L considered. However, this effect is more pronounced in the BML-hybrid, where higher values of c_L are required to adjust the flame position to the experimental data. Best agreement using the BML-Abu-Orf is attained with $c_L = 3.25$, whereas in the BML-hybrid, $c_L > 12.5$ is required.

Even though most of the reported literature related to the BML model suggests values of c_L around unity, other values have been reported within the range of $0.23 < c_L < 12.3$ (RANASINGHE; MALALASEKERA, 2017). Moreover, these are in line with the solution of the reacting flow field based on the discretisation of the standard Navier-Stokes equations. In this sense, the validity of the model constants range becomes questionable once the porosity-parameterised Navier-Stokes equations are considered, as in the case of the STOKES code.

Varying c_{LAM}

After performing the sensitivity analysis based on variations in c_L, a new sensitivity analysis in terms of c_{LAM} was conducted. The fixed value of $c_L = 3.0$ was

assigned in both the BML-Abu-Orf and the BML-hybrid models so as to allow the flame response evaluation strictly on the account of changes in c_{LAM}, which is a constant of the laminar burning model.

The overall analysis of Figure 6.4 indicates that variations in c_{LAM} significantly change the shapes of flame position curves (Figures 6.4a, 6.4d), as opposed to what was observed in variations in c_L. As c_{LAM} is decreased, the flame tends to smooth out its acceleration, leading to better representation of the initial moments of flame advance, especially in the BML-hybrid model.

Also, the improvement due to a decrease in c_{LAM} seems to reach a minimum value of 0.1, as lower values may lead to inconsistencies in the flame position histories, as it can be observed in the result from BML-hybrid model (Figure 6.4d). Significant improvements are also observed for $c_{LAM} \approx 0.1$ in both the flame speed (Figure 6.4b, 6.4e) and overpressure curves (Figure 6.4c, 6.4f).

Therefore, these observations lead to an calibrated value of $c_{LAM} \approx 0.1$ for a fixed value of $c_L = 3.0$. It is clear however that further adjustments are needed for both models, in order to achieve better agreement. Figure 6.4 shows that the BML-hybrid is still overpredicting the overall flame behaviour.

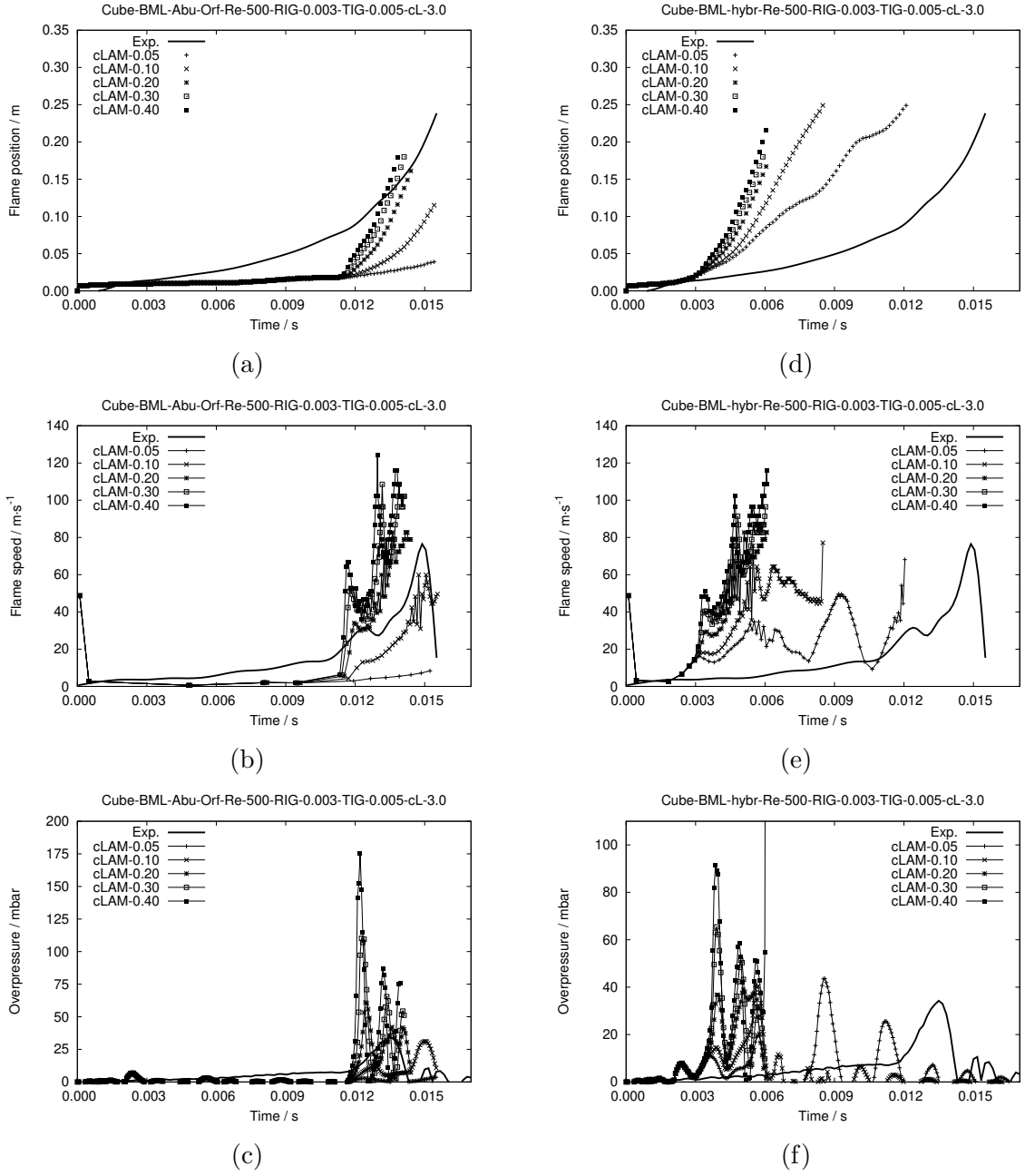

Figure 6.4: Variations of c_{LAM} constant in the models BML-Abu-Orf (a; b; c) and BML-hybrid (d; e; f) in Chamber 1. (a) and (d) Flame position; (b) and (e) Flame speed; (c) and (f) Overpressure at the chamber outlet. Values of Re_{Th} and c_L are taken respectively as 500 and 3.0.

Varying Re_{Th}

Following the investigations on the laminar burning model, focus is now placed on variations of the threshold value of the turbulent Reynolds number Re_{Th}, which are presented in Figure 6.5. Here we fix $c_L = 1.0$ and $c_{LAM} = 4/9$ as originally proposed by literature.

The overall analysis of Figure 6.5 seems to agree with the observations of Vianna

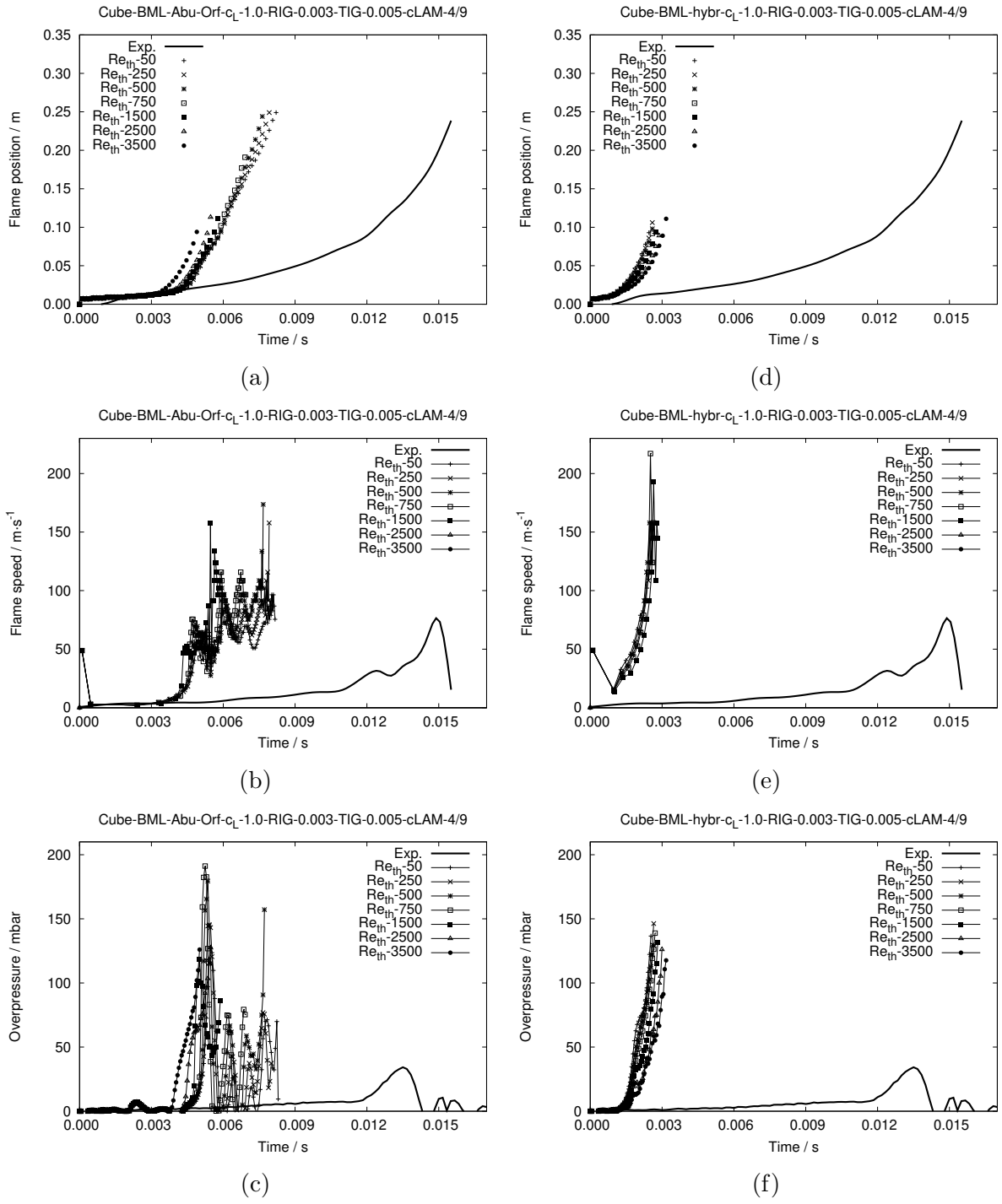

Figure 6.5: Varying the Re_{Th} in the models BML-Abu-Orf (a; b; c) and BML-hybrid (d; e; f) in Chamber 1. (a) and (d) Flame position; (b) and (e) Flame speed; (c) and (f) Overpressure at the chamber outlet. Values of c_L and c_{LAM} are taken respectively as 1.0 and 4/9.

& Cant (2014), where no substantial changes are observed on the flame behaviour with variations in Re_{Th}. Flame behaviour is greatly overpredicted by both the BML-Abu-Orf and the BML-hybrid.

Varying $\mathbf{Re_{Th}}$ with $\mathbf{c_{LAM} = 0.1}$

Another sensitivity analysis to variations in $\mathrm{Re_{Th}}$ is conducted, only now considering fixed values of $c_L = 2.0$ and $c_{LAM} \approx 0.1$ in both models.

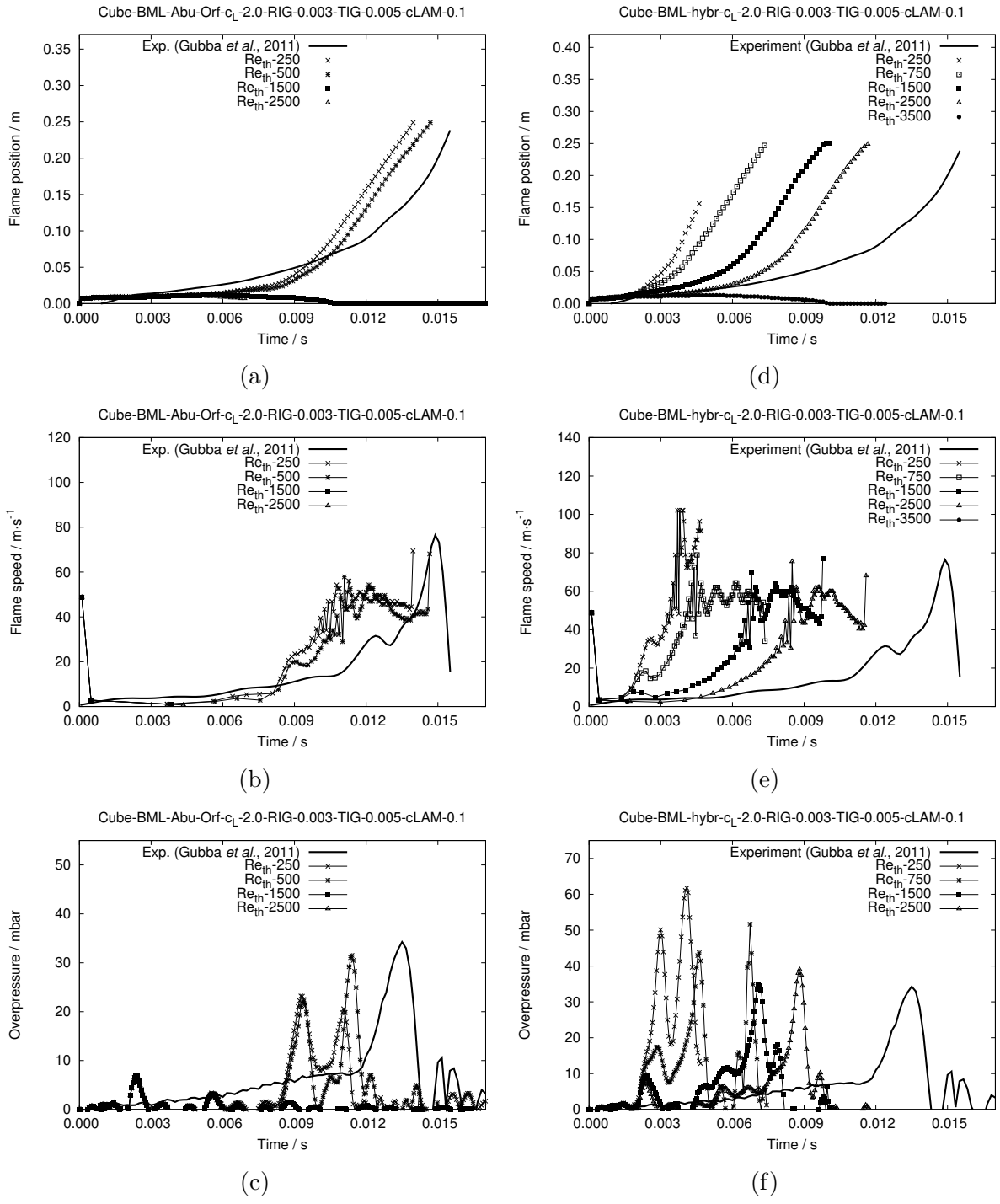

Figure 6.6: Varying $\mathrm{Re_{Th}}$ threshold in the models BML-Abu-Orf (a; b; c) and BML-hybrid (d; e; f) in Chamber 1. (a) and (d) Flame position; (b) and (e) Flame speed; (c) and (f) Overpressure at the chamber outlet. Values of $\mathrm{Re_{Th}}$ and c_L are taken respectively as 500 and 3.0.

Bearing in mind that $\mathrm{Re_{Th}}$ determines the transition from the laminar to the turbulent regimes of propagation, increases in $\mathrm{Re_{Th}}$ are expected to delay the flame. This is because when transition is taken to occur at a higher $\mathrm{Re_{Th}}$, the laminar burning is calculated in more regions of the domain. However, this was not observed when $\mathrm{Re_{Th}}$ was varied with the value fixed at $c_{LAM} = 4/9$, as proposed by the original model (VIANNA; CANT, 2014).

Figure 6.6 shows a remarkable improvement in the overall flame behaviour when $\mathrm{Re_{Th}}$ is varied with a fixed value of $c_{LAM} \approx 0.1$. The shapes of the curves of flame position, speed and overpressure, are greatly improved as $\mathrm{Re_{Th}}$ is changed with $c_{LAM} \approx 0.1$. As opposed to the original model, where the flame is almost insensitive to changes in $\mathrm{Re_{Th}}$ for $c_{LAM} = 4/9$ (Figure 6.5), variations in the $\mathrm{Re_{Th}}$ for $c_{LAM} \approx 0.1$ produce a notable effect on the flame time arrivals (Figure 6.6d), especially in the BML-hybrid model.

Also, it can be concluded that the sensitivity to changes in $\mathrm{Re_{Th}}$ is only observed when c_{LAM} is reduced to the value of 0.1. Because the analysis of Figure 6.3 showed nearly no improvement in curve shapes to changes in c_L, it is possible to affirm that sensitivity to $\mathrm{Re_{Th}}$ is on the account of the reduced $c_{LAM} \approx 0.1$.

With respect to the calibrated value of $\mathrm{Re_{Th}}$, analysis of the flame position histories (Figures 6.6a, 6.6d) indicate that transition from laminar to turbulent should occur at around $\mathrm{Re_{Th}} \approx 2500$ in the case of the BML-hybrid. In the case of the original BML-Abu-Orf model, the value of $\mathrm{Re_{Th}} \approx 500$ remains to be the most appropriate.

Both models however, were benefited from the calibration of $c_{LAM} \approx 0.1$. Figure 6.6a shows that the sharp rise of the flame position curve was satisfactorily smoothed in the BML-Abu-Orf case as well, which makes Figures 6.6a, 6.6b and 6.6c the best results of STOKES using the the Abu-Orf correlation. Although these improvements may motivate future investigations, they will not be addressed from this point forward in the present work. They are presented here with the intention of shedding light on the relevance of the laminar burning model. Furthermore, the overall purpose of this analysis is to show the improvements achieved by the proposed BML-hybrid in comparison with the original version of STOKES. Because of that, results that will be presented further in this work comparing the BML-hybrid with the BML-Abu-Orf will consider the BML-Abu-Orf as the "untouched" version of STOKES, that is, $c_{LAM} = 4/9$, $\mathrm{Re_{Th}} = 500$ and using the Abu-Orf correlation.

All in all, these findings highlight the importance of adequately representing the initially laminar phase of the flame propagation, especially when the turbulent burning model is known for having a tendency to produce unphysically high burning rates along walls, as in the case of the BML model. This is due to the direct dependence of $\hat{L}_y$ on the L_{turb}, which was eliminated by the Abu-Orf & Cant (2000) model but re-introduced by the proposed fractal-based approach in the BML-hybrid model. In the wall proximity, L_{turb} decreases, leading to reductions on the modelled $\hat{L}_y$. This in turn leads to an increase

in the reaction rate, which explains the need for higher c_L values as well as the need for resorting to the laminar burning model calibration.

In this sense, the extensive previous analysis lead to the calibrated values $c_{LAM} = 0.09$ and $\mathrm{Re_{Th}} = 2500$, which are used respectively in the laminar burning model and in the laminar-to-turbulent BML-hybrid blending function. Therefore, the transition from the laminar to the turbulent regime of propagation is taken to occur at $\mathrm{Re_{Th}} = 2500$, meaning that the laminar burning model is calculated in regions of the domain with $\mathrm{Re_{Th}} < 2500$, and the turbulent burning model is used in nodes where $\mathrm{Re_{Th}} > 2500$. This threshold value is in line with the transition Reynolds number of internal flows, however further investigations are needed before drawing any conclusions about the relation between them.

In possession of the new calibrated values of the laminar burning model ($c_{LAM} = 0.09$ and $\mathrm{Re_{Th}} = 2500$), new calibrations of c_L were conducted with the BML-hybrid. Plots of flame position against time are shown in Figure 6.7. Results of flame speed and overpressure were omitted for brevity and because it will be discussed later only for the best result, which is achieved with $c_L = 3.5$. The overall analysis of Figure 6.7 shows that as c_L is increased, the representation of the initial stages of flame development are improved.

Also, it becomes evident from Figure 6.7 that the improvement in the curve trend was achieved on the account of the calibration of c_{LAM} and $\mathrm{Re_{Th}}$ and that the effect of changes in c_L is mainly to shift the curves horizontally, as previously observed in Figures 6.3a and 6.3d.

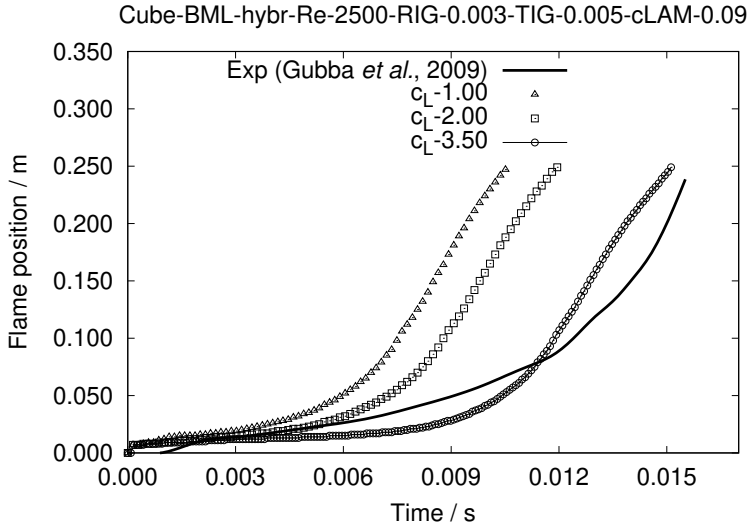

Figure 6.7: Time histories of flame position inside Chamber 1 for different values for c_L using the BML-hybrid with $c_{LAM} = 0.09$ and $\mathrm{Re_{Th}} = 2500$.

Best results

From this point forward, it is important to clarify that whenever the model BML-hybrid is mentioned, it will be also referring to the calibrated values of $c_{LAM} = 0.09$ and $Re_{Th} = 2500$. In addition, the results related to the BML-Abu-Orf maintain the values $c_{LAM} = 4/9$ and $Re_{Th} = 500$ so that comparisons can be made with the STOKES code with the original combustion model, as reported by Ferreira *et al.* (2019), Ferreira & Vianna (2019).

Figure 6.8 shows the flame contours at different time steps using the BML-Abu-Orf model (Figure 6.8a), the BML-hybrid (Figure 6.8b), and FLACS simulation (Figure 6.8c). The images from STOKES simulations are obtained by the renderisation of the reaction progress variable c, whereas in FLACS the variable PROD refers to the mass fraction of combustion products (PROD = 0.279 is equivalent to $c = 1.0$).

Three different colour scales are used to merely emphasise visually that three different simulation approaches are being used. In Figure 6.8, the BML-Abu-Orf results are shown in x-ray colours, the BML-hybrid in black body radiation colours and FLACS in tones of orange. The differences in colours do not affect the analysis that will be presented.

Figure 6.8a is the best result obtained from the original STOKES code implementing the BML-Abu-Orf model, where no modification in the combustion model is carried out and c_L is adjusted to 3.25. Figure 6.8b refers to the proposed BML-hybrid model with $c_L = 3.5$, which also includes the calibrated values of $c_{LAM} = 0.09$ and $Re_{Th} = 2500$.

Although some differences can be noticed in the flame contours, Figure 6.8 presents very good overall agreement in the flame propagation behaviour in the three simulation cases. Separation between the unburned reactants and burned products is clearly observed as well as the flame region where the progress variable ranges $0 < c < 1$.

The first difference is related to the flame tendency to propagate along the walls of the chamber. Whereas in the BML-hybrid (Figure 6.8b) and in the FLACS (Figure 6.8c) simulation the flame limits tend to grow towards the side walls before reaching the obstacle, in the BML-Abu-Orf model (Figure 6.8a) this tendency occurs after the flame passes the obstacle, causing a slight loss in flame symmetry.

With respect to the flame contour around the recirculation zones behind the obstacle, another relevant difference is observed. The BML-hybrid and FLACS simulation show a well-defined wake formation behind the cube, which cannot be explicitly identified in the BML-Abu-Orf simulation (Figure 6.8a). This observation becomes evident when the vector velocity field is shown near the obstacle in Figure 6.9.

Figure 6.9 shows the vector velocity field zoomed in the obstacle region taken from Figures 6.8a (BML-Abu-Orf) and 6.8b (BML-hybrid) at 14.5 ms and 13.0 ms, respectively. Although the simulation times are different, the purpose is to evaluate approximate stages of flame development.

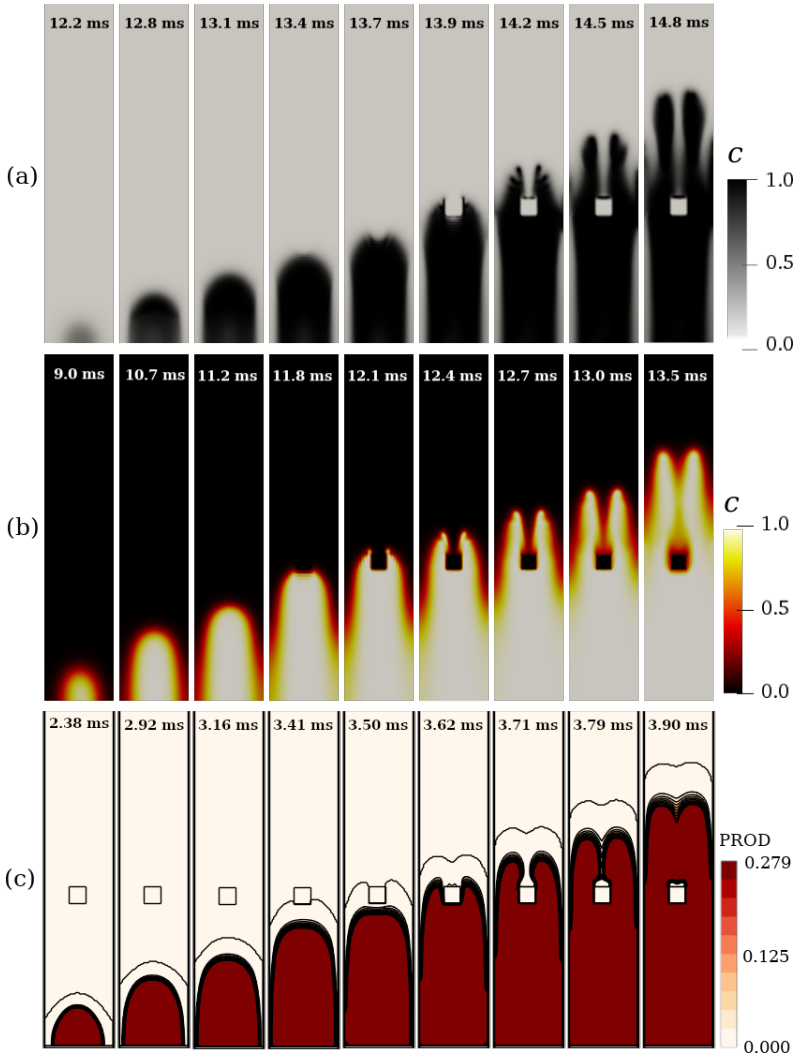

Figure 6.8: Flame contour inside Chamber 1 at different time steps. (a) STOKES simulation with BML-Abu-Orf; (b) STOKES simulation with BML-hybrid; (c) FLACS simulation.

Figure 6.9a shows the maximum magnitude of the velocity vector in the x direction three times higher than in the proposed BML-hybrid simulation. The abnormally large velocity field generated by the flame may be strengthening the recirculation zone, as indicated by the bigger reverse vectors behind the obstacle. Moreover, the velocity vectors in Figure 6.9a flow in an unorganised fashion, leading the flame towards the side walls of the chamber. On the other hand, the flow around the obstacle attained by the proposed BML-hybrid (Figure 6.9b) shows an improved and well behaved flow and wake region.

Plots of flame position, overpressure and speed, from simulations of Figure 6.8 are shown respectively in Figures 6.10a, 6.10b, and 6.10c. A significant improvement was achieved by the BML-hybrid model, when it is compared to FLACS simulation and the originally implemented BML-Abu-Orf model. The problem of the sudden rise of the flame position curve was diminished by the proposed approach, which consequently improved both flame speed and overpressure predictions of flame explosion in Chamber 1.

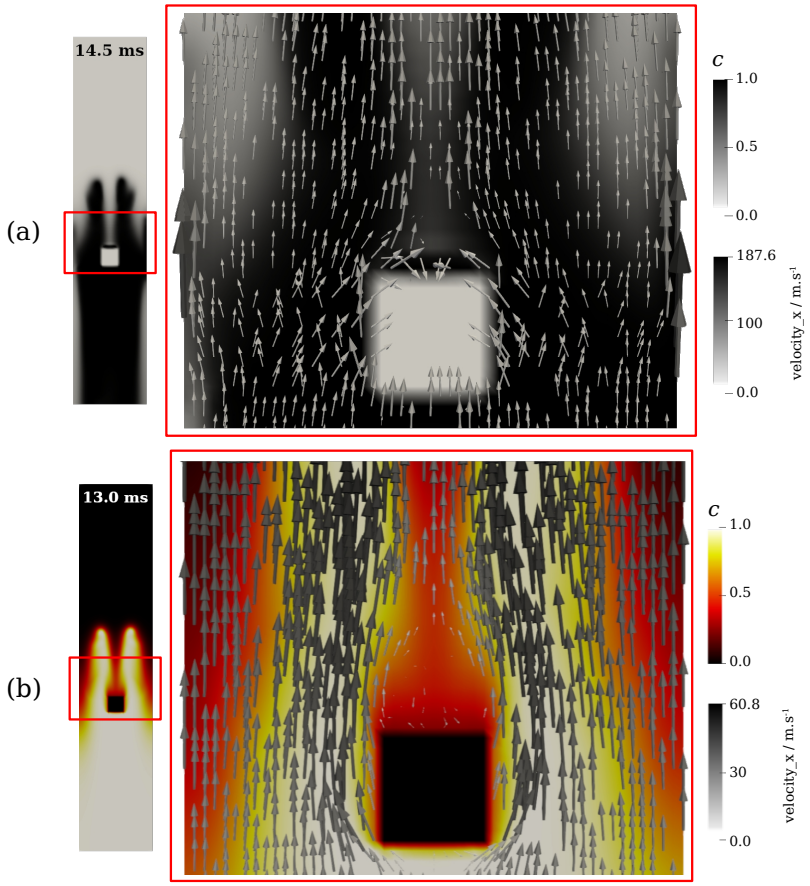

Figure 6.9: Vector velocity field zoomed in the obstacle region in Chamber 1. (a) STOKES simulation with BML-Abu-Orf at 14.5 ms; (b) STOKES simulation with BML-hybrid at 13.0 ms.

FLACS results indicate the software limitation to represent flame explosion in small-scale geometries, where flame position time history and overpressure peaks are greatly overpredicted (Figure 6.10d). The normalisation of FLACS overpressure with the maximum peak from the experimental results shows a deviation of around 21 times above the experimental data.

6.2.2 Chamber 2

Although Chamber 2 is presented here secondly for the sake of organization, it was the last of the three combustion chambers to be tested with the proposed BML-hybrid model. Because of that, it has not been tested for variations in c_{LAM} and $\mathrm{Re}_{\mathrm{Th}}$ as Chamber 1 and 3 were. Instead, the calibrated values of $c_{LAM} = 0.09$ and $\mathrm{Re}_{\mathrm{Th}} = 2500$ were directly used, and only calibration of the constant c_L was performed.

Figure 6.11 shows flame contours obtained from STOKES simulations with the original BML-Abu-Orf model (Figure 6.11a), the BML-hybrid (Figure 6.11b), and FLACS simulation (Figure 6.11c). For the BML-Abu-Orf, $c_L = 2.0$, and for the BML-hybrid,

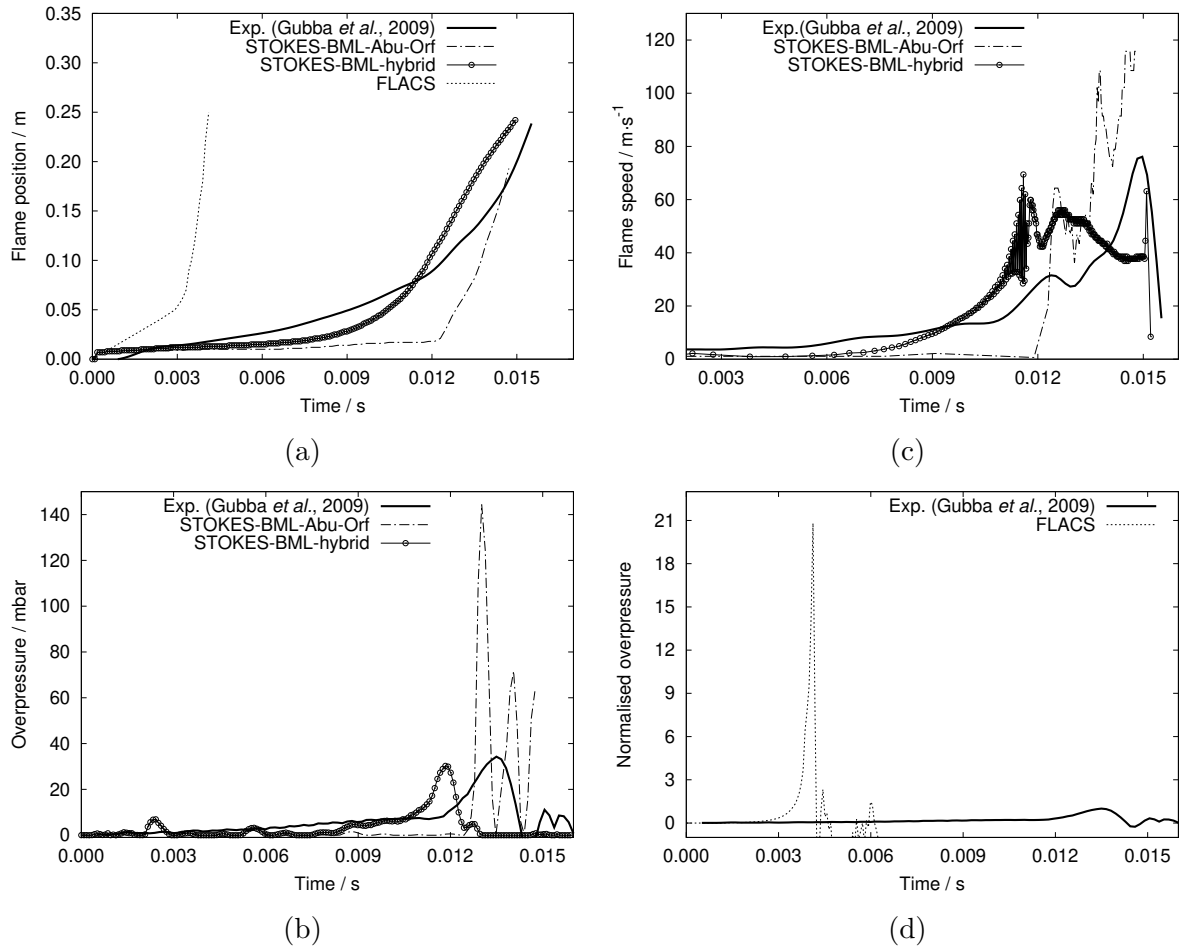

Figure 6.10: Plots of flame position (a), overpressure (b), flame speed (c), and normalised overpressure (d) from simulations in Chamber 1 using STOKES with the BML-Abu-Orf, the BML-hybrid and FLACS.

$c_L = 7.0$. It can be observed that the BML-hybrid simulation presents a clear separation between the reactants and products, whereas in the BML-Abu-Orf simulation the progress variable does not distinctively reach the $c = 1$, especially in the first simulation time steps.

In all the simulations of Figure 6.11, the flame tends to propagate along the walls after passing over the cubic obstacle. Large Eddy Simulation (LES) performed by Ibrahim *et al.* (2009), shows the flame preferentially propagating along the axial direction, instead of along the walls. This may indicate the inherent limitation of flamelet models in the RANS approach, which are know for having a tendency to accelerate along walls. FLACS simulation (Figure 6.11c) a flame propagation around three times faster than STOKES simulations.

The flame time histories of simulations in Figure 6.11 are presented in Figure 6.12. The plots of flame position against time (Figure 6.12a) show a slight improvement obtained with the BML-hybrid when compared with the BML-Abu-Orf case. Both models struggled with capturing the final flame acceleration when passing over the cubic obstacle after 0.012 s. This effect is clearly shown in Figure 6.12b, where after the cubic obstacle

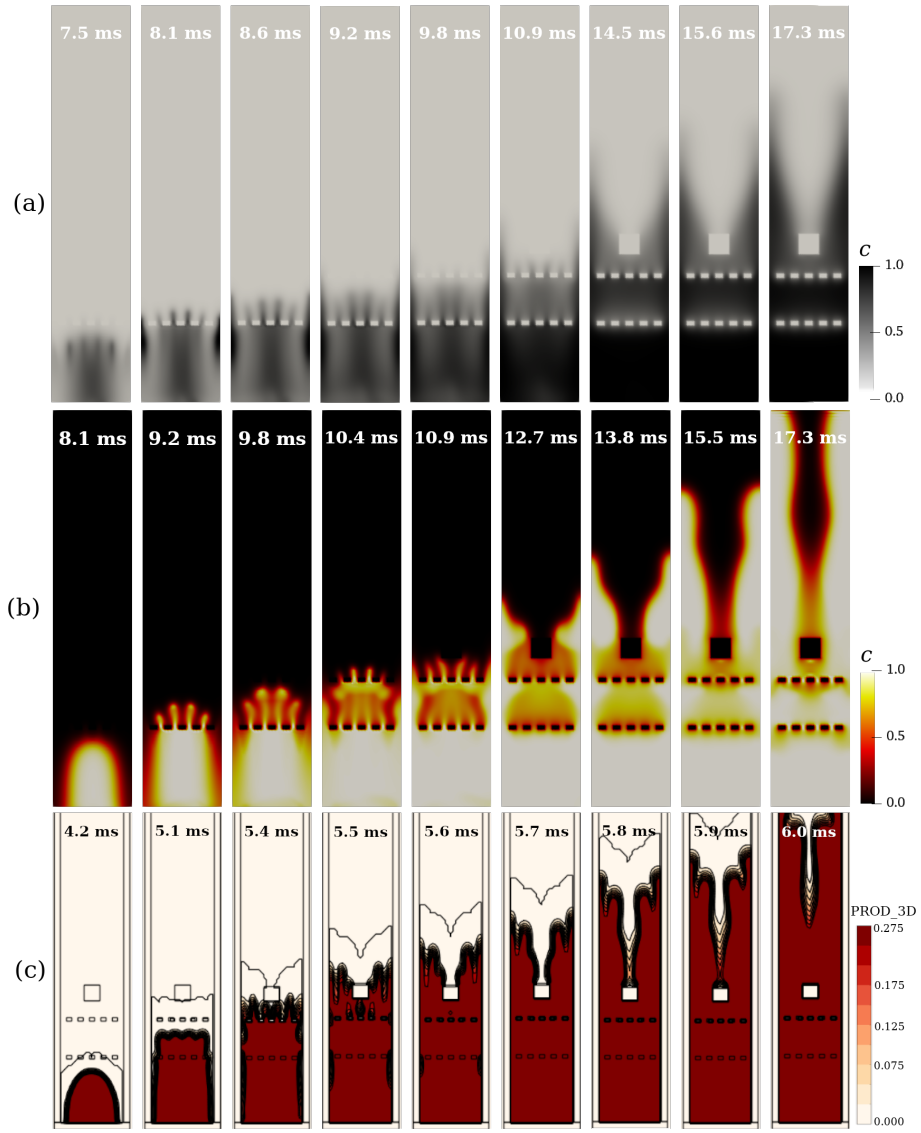

Figure 6.11: Flame contour inside Chamber 2 at different time steps. (a) STOKES simulation with BML-Abu-Orf; (b) STOKES simulation with BML-hybrid; (c) FLACS simulation.

located at 0.1 m, the flame is incapable of continuing to accelerate.

6.2.3 Chamber 3

Several analyses were conducted for Chamber 3 in order to evaluate the effect of variations in c_L, c_{LAM} and Re_{Th} and results can be observed in Appendix C in Figures C.1, C.2, and C.3, respectively. Similar conclusions to the simulations in Chamber 1 can be drawn, meaning that initially, both the BML-Abu-Orf and the BML-hybrid models overpredict the flame propagation inside the chamber. This limitation is improved in the BML-hybrid approach by setting $c_{LAM} = 0.09$ and $Re_{Th} = 2500$, as previously suggested by the results in Chamber 1.

Figure 6.13 shows the flame contours at different time steps inside Chamber 3

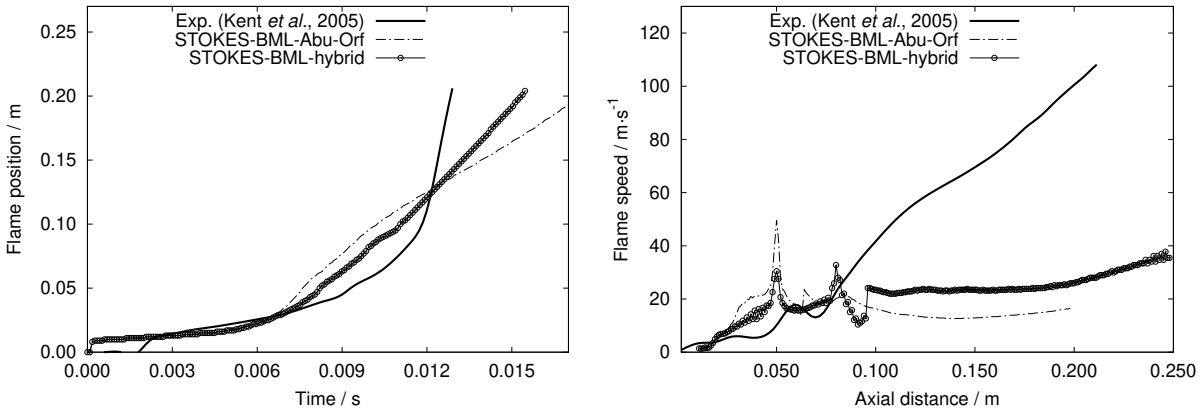

(a) (b)

Figure 6.12: Plots of flame position (a) and flame speed (C) from STOKES simulations in Chamber 2 comparing the BML-Abu-Orf and the BML-hybrid models.

from simulations using the BML-Abu-Orf model (Figure 6.13a), the proposed BML-hybrid (Figure 6.13b), and FLACS simulation (Figure 6.13c). Figure 6.13a refers to the best result obtained from the original STOKES code, with the unchanged BML-Abu-Orf model where only c_L is calibrated to a value of 4.0. Figure 6.13b shows the best result from the BML-hybrid, where $c_L = 10.0$, $c_{LAM} = 0.09$ and $Re_{Th} = 2500$. It can be observed that the flame propagation tendency is quite similar to each other in all of the three cases, where the three zones of reactants, products and flame are consistent and can be clearly identified.

The experimental and LES simulation data reported by Patel *et al.* (2002) and Sarli *et al.* (2009) are taken as benchmarks for the evaluation of flame explosion in Chamber 3. The rate of change in flame position is small in the beginning of propagation (Figure 6.14a) until the flame reaches the first obstacle located at 0.1 m inside the chamber. At this moment the flame acceleration is increased and, after passing over the obstacle, the acceleration drops due to the expansion of the flame (bumps observed in Figure 6.14c). The presence of a sequence of three obstacles strongly accelerates the flame, which reaches the third obstacle at a speed ten times higher than that upstream of the first obstacle (SARLI *et al.*, 2009). After passing the third obstacle, the dominant pressure peak is produced at around 0.037 seconds (Figures 6.14b and 6.14d).

Analysis of Figure 6.14 shows an improvement in the prediction of flame position (Figure 6.14a) and in the flame speed plotted against the chamber axial distance (Figure 6.14c). The three bumps of the flame against the obstacles are better described by the BML-hybrid model, where the speed builds up from 10 m/s to 50 m/s. In the BML-Abu-Orf model, even though the speed is overestimated in the first and in the second obstacles, it fails to reproduce the progressive speed increase at passing the third obstacle.

The pressure history inside Chamber 3 (Figure 6.14b) is underpredicted by STOKES simulations regardless the combustion model used. In terms of relative errors,

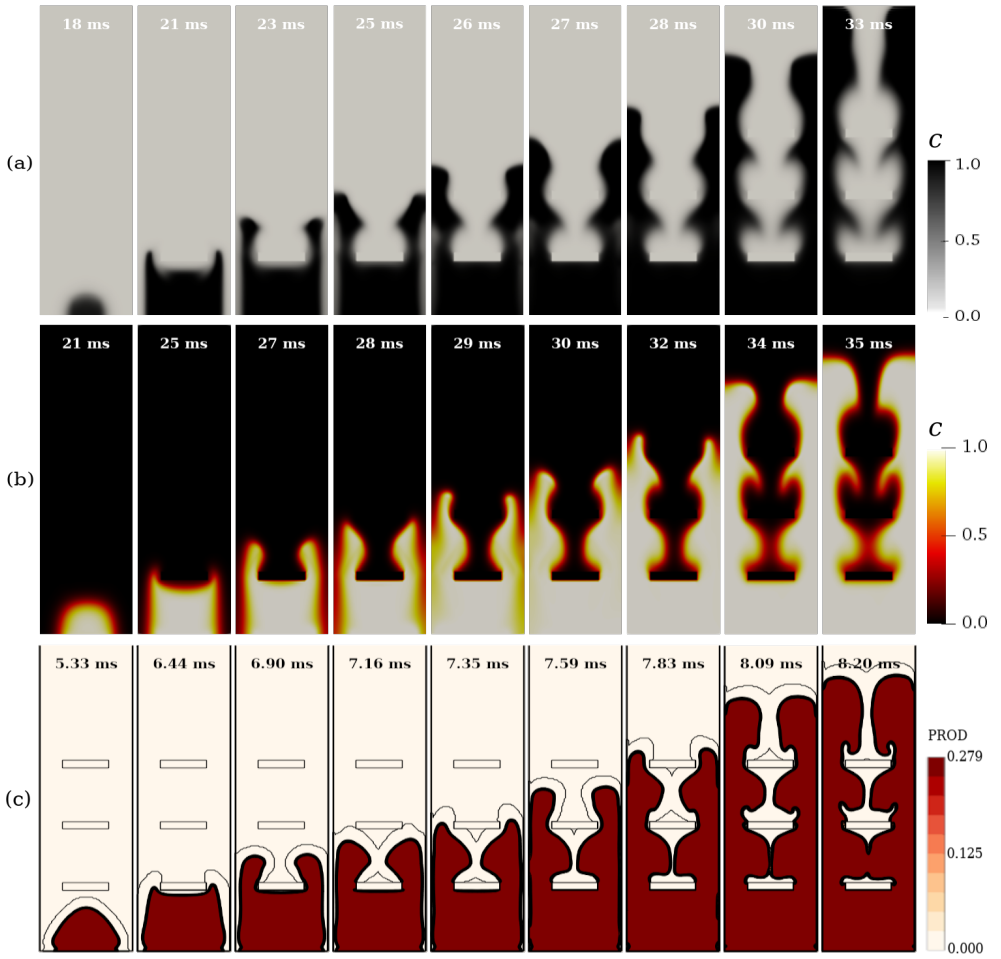

Figure 6.13: Flame contour inside Chamber 3 at different time steps. (a) STOKES simulation with BML-Abu-Orf; (b) STOKES simulation with BML-hybrid; (c) FLACS simulation.

the maximum overpressure estimation is around 75% lower than the experimental and LES simulations reported by Patel *et al.* (2002) and Sarli *et al.* (2009). Despite this underestimation, the proposed BML-hybrid presented a dominant overpressure peak, which is in better agreement with the experimental data than the original BML-Abu-Orf, where the existence of three peaks of the same order of magnitude can be observed.

FLACS simulation of explosion in Chamber 3 consistently overestimates the rate of change of flame position and pressure peaks for small geometries, as already mentioned in the Chamber 1 analysis. Once again the prediction of the normalised overpressure (normalised by the maximum peak of experimental data) is around 21 times higher than the experimental data.

6.2.4 Chemical process module

After having conducted detailed investigation of the flame sensitivity to variations in model parameters c_L, c_{LAM}, and Re_{Th}, in Chambers 1 and 3, the BML-hybrid was

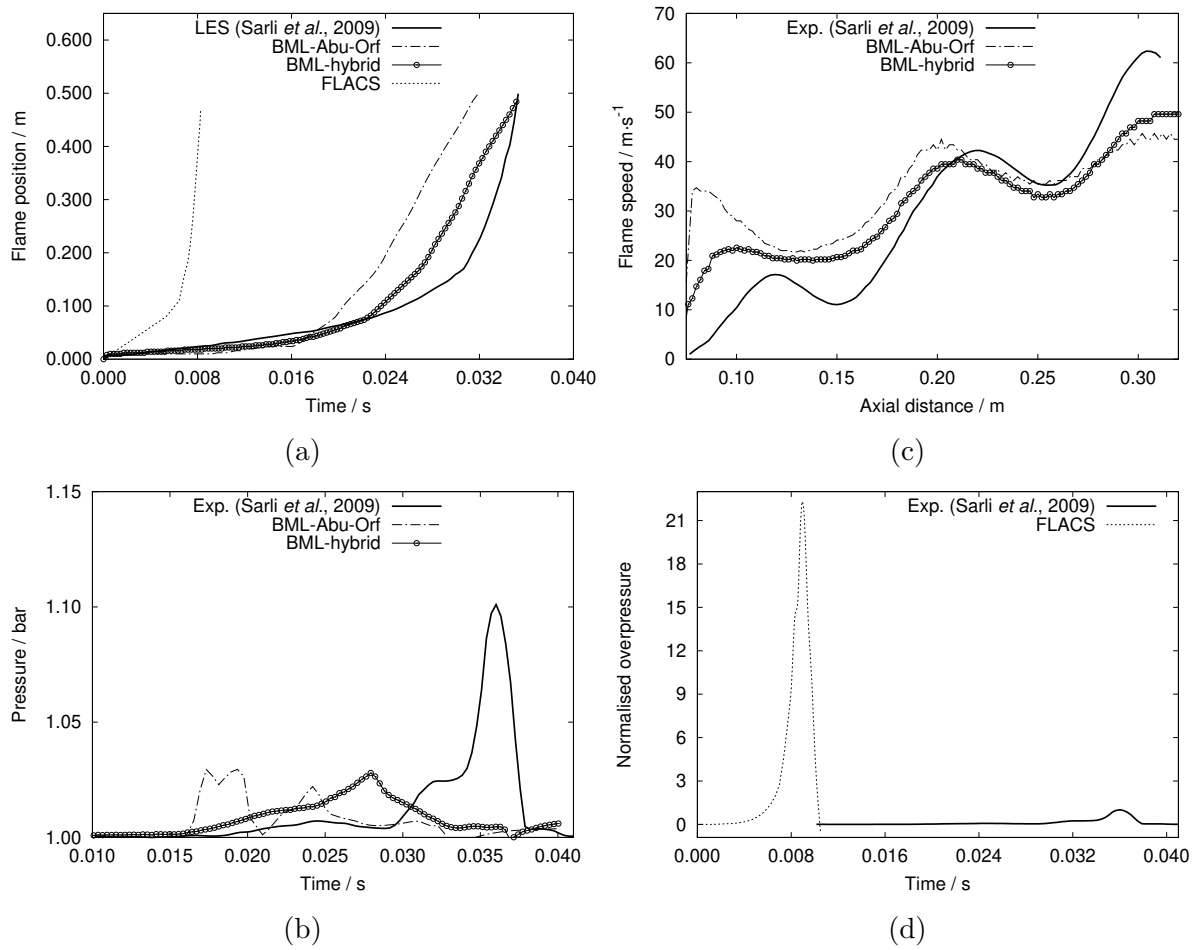

Figure 6.14: Plots of flame position (a), overpressure (b), flame speed (c), and normalised overpressure (d) from simulations in Chamber 3 from STOKES simulations with the BML-Abu-Orf, the BML-hybrid and FLACS simulation.

applied to simulate an explosion in a large-scale chemical process module. The purpose of this simulation case was not only to evaluate the model performance in a typical engineering facility of real-scale dimensions, but especially to analyse flame evolution in the absence of nearby walls, as opposed to what we had in the chambers cases.

The values of c_{LAM} and $\mathrm{Re_{Th}}$ were set to 0.09 and 2500, respectively, and c_L was tuned to the value of 5.0. Table 6.1 presents a summary of the main setup values applied to this case, including the ignition time (TIMEIG) and the ignition radius (RIG). The mesh spacing (Δx), the smooth factor (SF), and the Courant–Friedrichs–Lewy number (CFL) were presented in Table 5.2.

Table 6.1: Model constants and numerical method parameters used in the simulation setup of the explosion simulation in the process module geometry using STOKES.

	c_L	c_{LAM}	$\mathrm{Re_{Th}}$	TIMEIG (s)	RIG (m)	Δx (m)
BML-hybrid	5.0	0.09	2500	0.15	1.5	0.50

The grid used in STOKES simulation and FLACS simulation is shown in

Figures 6.15a and 6.15b, respectively. Geometry and domain sizes agree with each other and with what was described in the Methodology (Section 5).

(a)

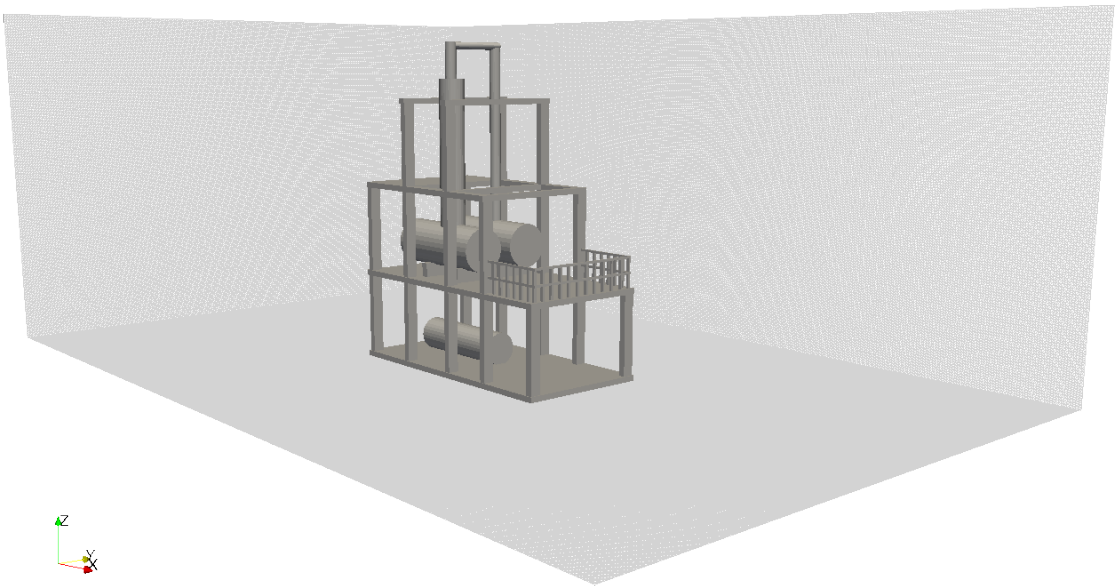

(b)

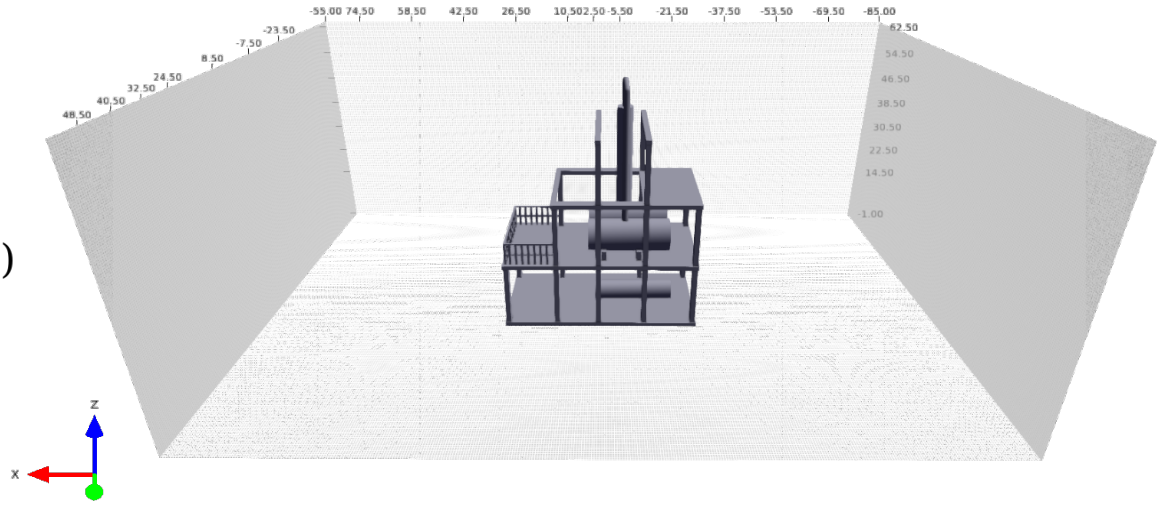

Figure 6.15: Grid lines of (a) STOKES simulation in planes XY (Z = -1 m), YZ (X = -85 m) and XZ (Y = 55 m); and (b) FLACS simulation in planes XY (Z = -1 m), YZ (X = 85 m and X = -85 m) and XZ (Y = -55 m) showing uniform mesh size of 0.50 m in all directions.

No grid independence tests could be performed for STOKES simulations, because changes in grid sizes presented a high dependence on CFL and SF numbers, in such a way that numbers shown in Table 6.1 of SF and CFL could not be reproduced for different mesh sizes (0.60, 0.75 m). This issue should be investigated in future work. Initially, a uniform grid was used in FLACS as presented in 6.15b for the sake of comparison with STOKES' grid. Later, stretched grids of different sizes were considered in other

FLACS simulations, as it will be discussed later in this section.

Figure 6.16 shows a comparison between STOKES-BML-hybrid (Figure 6.16a) simulation and FLACS simulation (Figure 6.16b), with respect to the development of the flame iso-surface. An iso-surface of $c = 0.1$ is considered in (Figure 6.16a). Relatively good qualitative agreement of the flame kernel evolution is observed, however, the initial stages of flame propagation is developed faster in the STOKES-BML-hybrid than in FLACS simulation. Furthermore, flame contours of FLACS simulation indicate a tendency of the flames to go upwards, which is not observed in STOKES simulation.

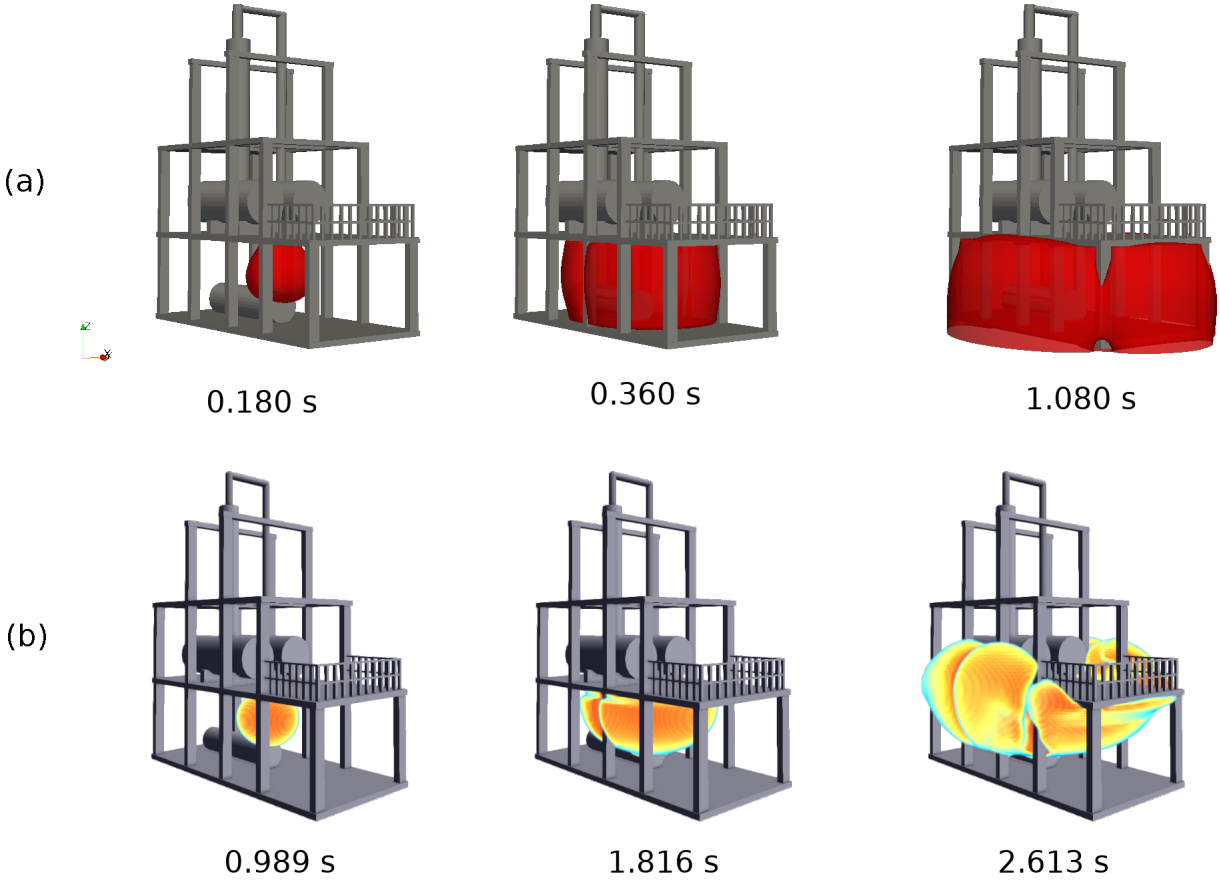

Figure 6.16: Explosion simulation at different time steps in the chemical process module. (a) Iso-surface c = 0.1 from STOKES simulation using the BML-hybrid; and (b) FLACS simulation corresponding to the uniform grid in Figure 6.15b.

The accelerated flame growth in the early stages of propagation in the STOKES-BML-hybrid case may be related to the ignition model limitations. A physically large ignition radius of 1.5 m had to be considered in order to enclose at least three computational cells. Moreover, the ignition time is equally very large, meaning that the cells within the ignition radius are ramped to $c = 1.0$ and is forced to be kept at this value until the flame is able to propagate on its own. This introduces a few uncertainties and may be affecting the evaluation of the early stages of flame propagation.

The rate of change of flame position in the positive X direction in the module

is depicted in Figure 6.17a. The shape of the graph makes it clear that the flame develops more rapidly until around 0.3 s, after which its displacement rate is attenuated. At this time, the flame reaches a distance of approximately 10 metres in the positive X direction, where a monitor point is defined to capture pressure variations (Figure 6.17b). The monitor coordinates are (10,0,9), which is located 10 metres away from the point of ignition (0,0,9).

At the time the flame front ($c = 0.1$) passes the monitor at around 0.3 s, an overpressure peak of approximately 50 mbar is sensed (Figure 6.17b). It is followed by an expected drop in pressure due to the gas expansion of the combustion products, which tends to equalise with the atmospheric pressure after some time. The pressure oscillation observed at the very beginning of propagation is probably the effect of the ignition model. The maximum overpressure reached in the whole domain is presented in Figure 6.17c, where a maximum peak of nearly 150 mbar was reached at 0.2 s. The equivalent FLACS simulation registered a maximum overpressure of 10 mbar, as it can be seen in Figure 6.18. Both pressures shown in STOKES and FLACS correspond to total pressures (static pressure + dynamic pressure).

Further comments on the initial stages of flame development are now made, highlighting the influence of the turbulent Reynolds number variation. Figure 6.19 shows the corresponding range of Re_t in the domain, which is compared to the range of the progress variable c. It is possible to see that at 0.007 s, the Re_t value goes up to 5333 in the centre of the flame, but starts to decrease especially after the ignition time ceases (0.15 s). As a consequence, at 0.180 s the maximum c drops, and no product region can be seen. However, at 0.324 s the regions of reactants, products and flame are regenerated, after which the flame continues to grow, leading to what is shown in Figure 6.16.

Especial attention should be payed to the fact that the maximum turbulent Reynolds number significantly decreases after some time. When the maximum Re_t drops below the threshold $\mathrm{Re}_{\mathrm{Th}}$ value of 2500, it means that only the laminar burning model is being considered in the calculation of the reaction rate. Therefore, even though the module geometry presents a moderate degree of confinement where the Re_t number is not expected to be significant, the turbulent reaction rate should be dominant. Controversially, Figure 6.19 shows that this is not the case, and instead, the laminar burning rate is being considered.

In the light of this observation, it is important that future work on the combustion model implemented in STOKES focuses on the investigation of the laminar-to-turbulent transition. The present work provides enough evidence to support the hypothesis that a blending function based on the local turbulent Reynolds number may not be adequate to simulate explosions in geometries with a low degree of confinement, as in the case of the process module.

Despite such observations, temperature and density profiles (Figures 6.20 and 6.21, respectively) are similar in both STOKES simulation with the BML-hybrid and

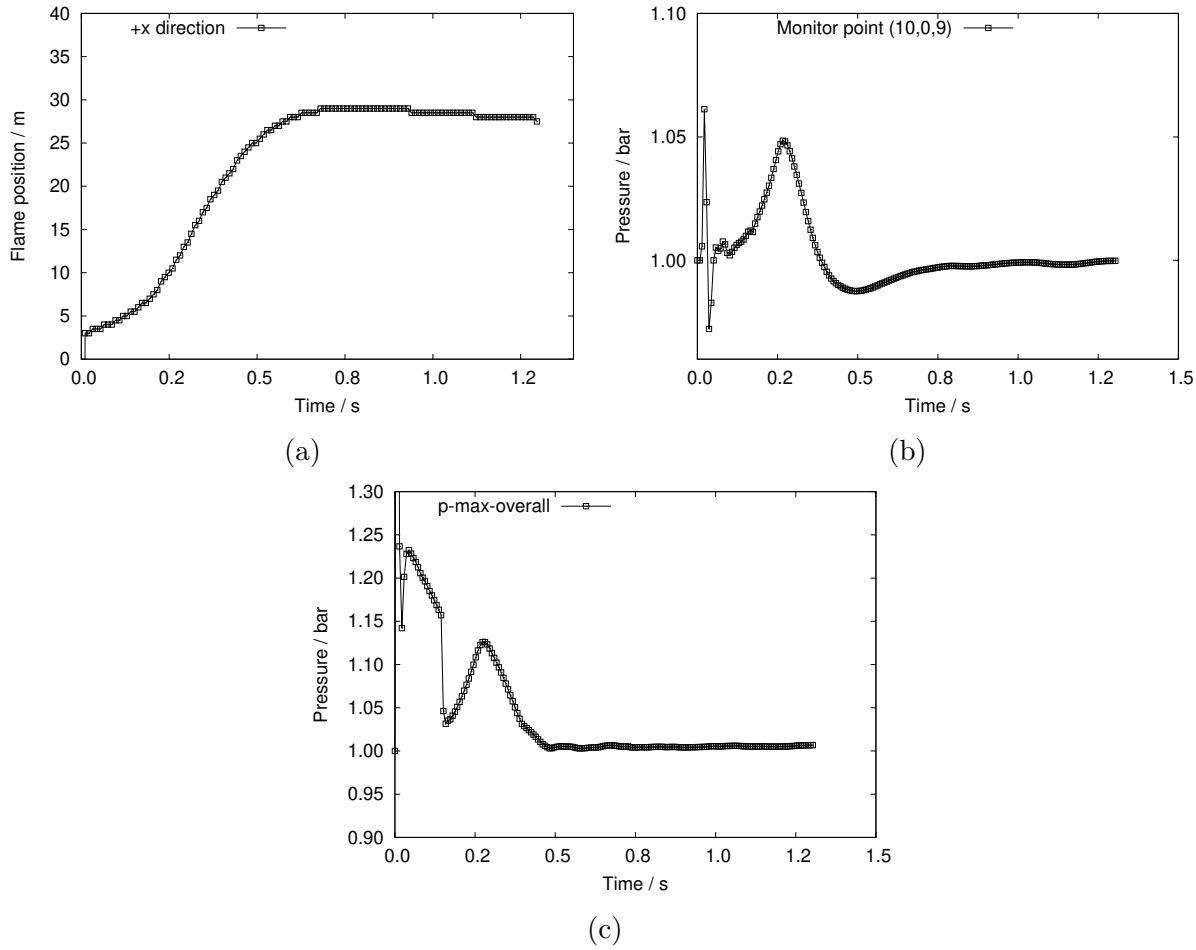

Figure 6.17: Plots of (a) flame position time history in the positive X direction; and (b) pressure time history captured by a monitor point located at (10,0,9) metres and (c) maximum pressure time history in the whole domain, obtained from STOKES simulation using the BML-hybrid.

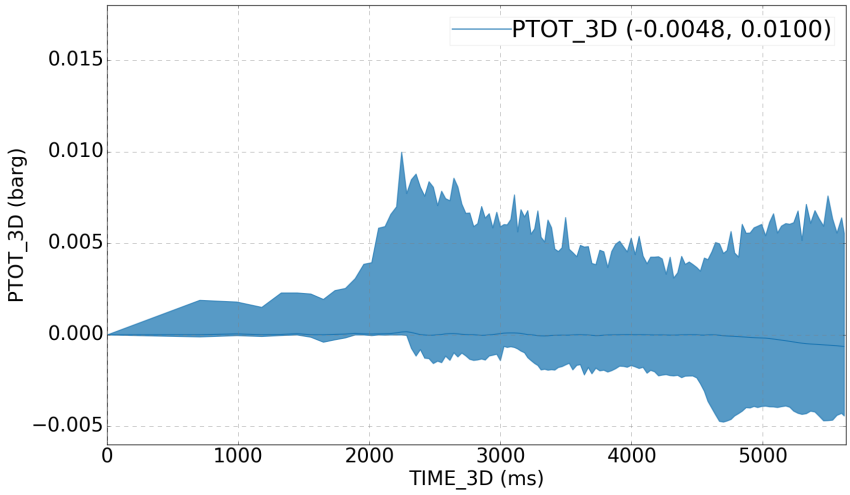

Figure 6.18: Total overpressure time history of explosion simulation in the process module conducted in FLACS, using uniform mesh $\Delta x = 0.50$ m.

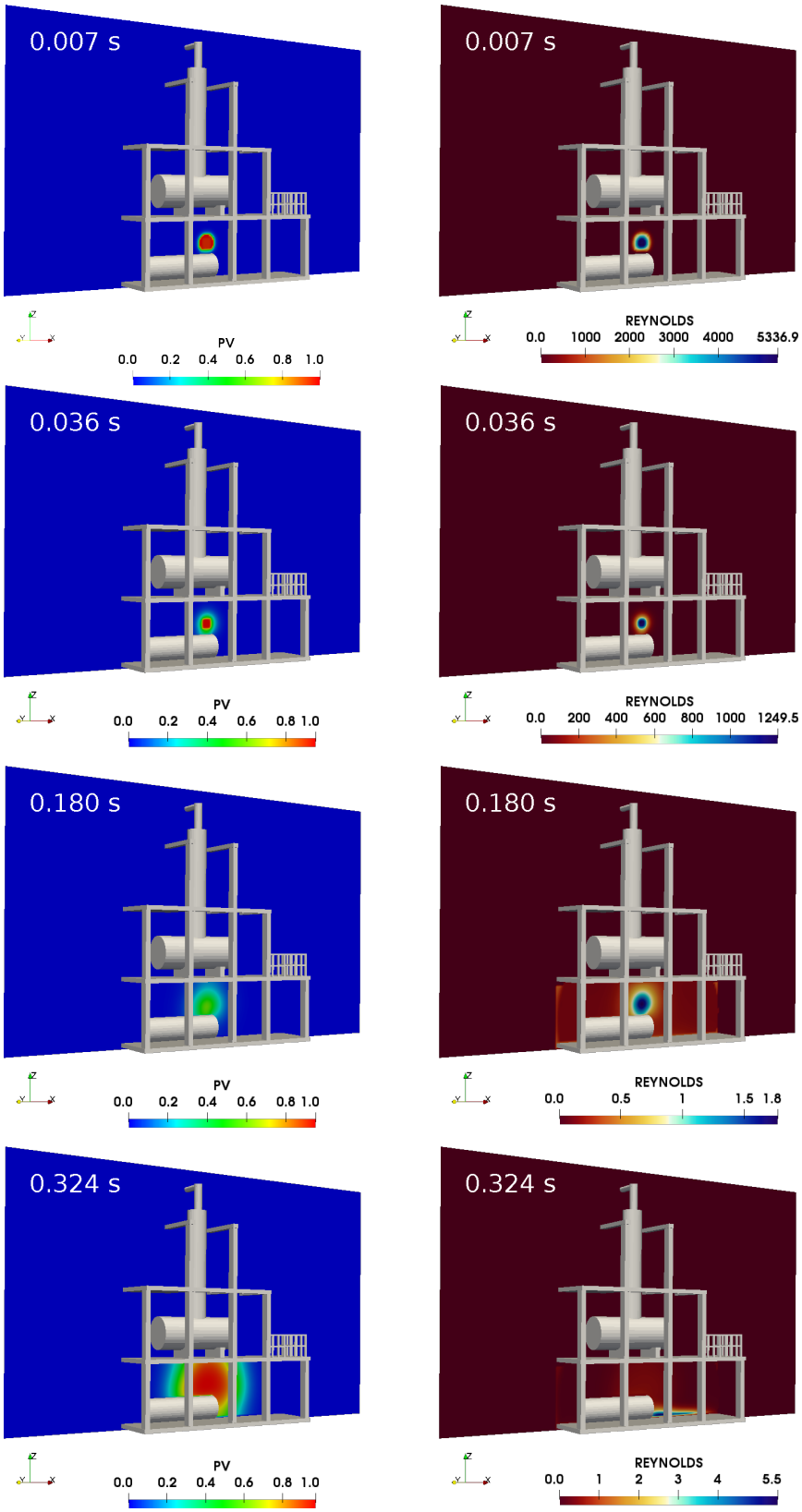

Figure 6.19: Progress variable and turbulent Reynolds number variation in the initial stages of flame propagation. Explosion simulation using STOKES with the proposed BML-hybrid model.

FLACS simulation. For approximate stages of flame development, which are taken at 0.360 s in STOKES (Figures 6.20a) and at 2.162 s in FLACS (Figures 6.20b), the maximum temperature reached is of the order of 2000 K in both cases (1994 K in STOKES and 2220 K in FLACS). This is also the case of density limits, which range from around 0.2 to 1.2 in STOKES (Figure 6.21a) and from 0.1 to 1.2 in FLACS (Figure 6.21b).

Figures 6.22a and 6.22b show respectively the pressure profile at 0.360 s in STOKES with the BML-hybrid, and the overpressure profile at 2.162 s in FLACS simulations. Once again these time steps are chosen as an attempt to perform a qualitative analysis considering approximate stages of flame development. The maximum overpressure predicted in STOKES using the BML-hybrid in the selected plane reaches 70 mbar, whereas FLACS simulation presents a maximum of 2.28 mbar in the selected plane and time step.

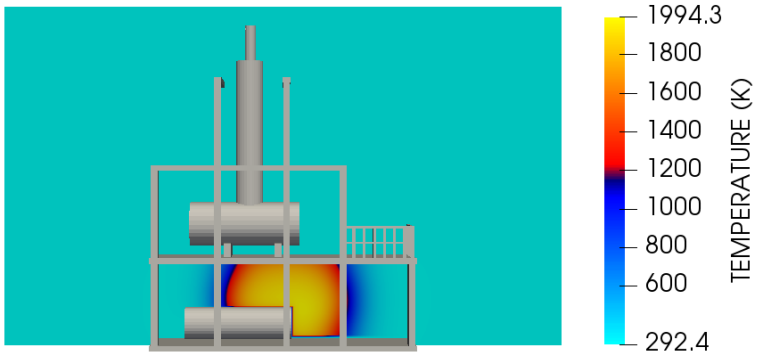

(a)

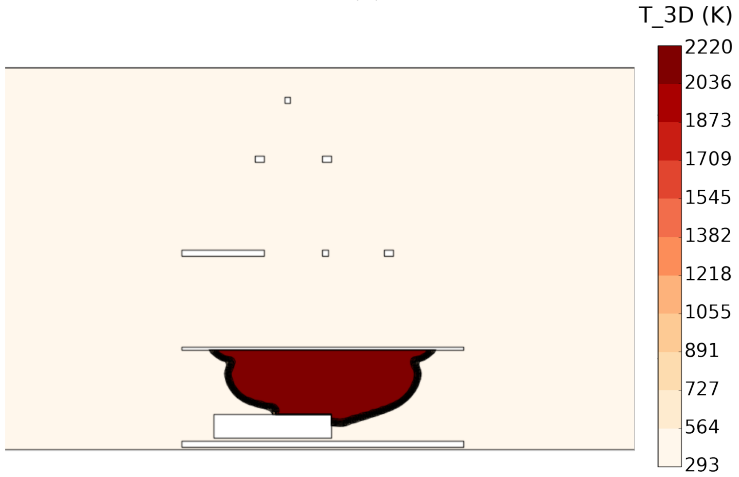

(b)

Figure 6.20: Temperature profile of gas explosion simulations in the process module using (a) STOKES with BML-hybrid at 0.360 s; and (b) FLACS at 2.162 s with uniform grid.

In order to address this discrepancy of overpressure prediction between STOKES and FLACS simulations, four new runs were performed in FLACS. In the new cases, the geometry and setup were kept unchanged and stretched meshes of different sizes were considered. Mesh sizes of 0.50, 0.25 and 0.15 m were used in the flammable region, from

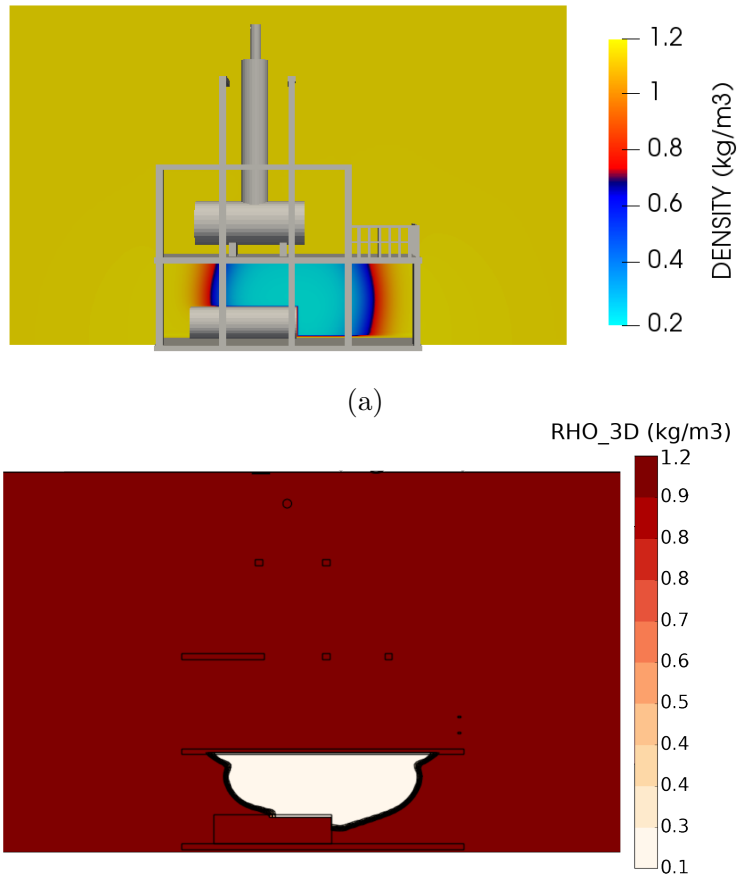

Figure 6.21: Density profile of gas explosion simulations in the process module using (a) STOKES with BML-hybrid at 0.360 s; and (b) FLACS at 2.162 s with uniform grid.

where grid cells were stretched with an increment ratio of 20%.

Details of mesh, domain and maximum overpressure of all five cases run in FLACS are presented in Table 6.2. Case 1 refers to the uniform grid case presented in Figures 6.15b, 6.16b and 6.18. Case 2 refers to the same domain as Case 1, only now using a stretched grid, as shown in Figure 6.23. Cases 3-5 have domains dimensions of 360 x 180 x 60.5 m, stretched grids, and minimum grid sizes of 0.50, 0.25 and 0.15 m. Larger domains are applied in Cases 3-5 in order to guarantee that results would not be affected by boundary proximity.

Results of total overpressure of Cases 2-5 (stretched grids) are presented as time histories in Figure 6.24. It is possible to observe that for all mesh sizes and domains the maximum overpressure takes place little after 2.0 s. On the other hand, magnitudes of peak overpressures are different.

In the stretched mesh of $\Delta x = 0.50$ m (Figure 6.24a), the maximum overpressure reached in the whole simulation was 15.7 mbar, corresponding to a 36.3% of deviation from the first case presented in Figure 6.22 using the uniform mesh. When a larger domain is used with half of the mesh size ($\Delta x = 0.25$ m, Figure 6.24d), the maximum overpressure

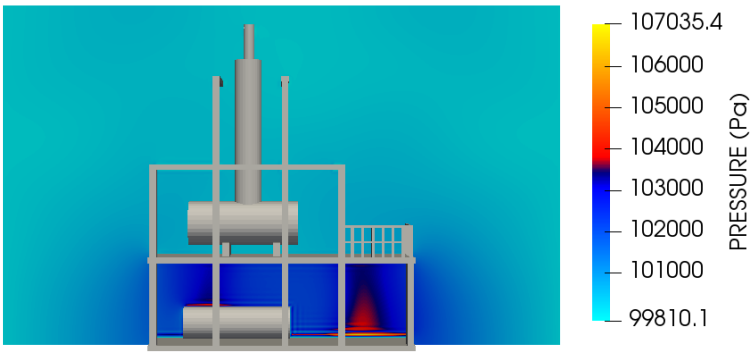

(a)

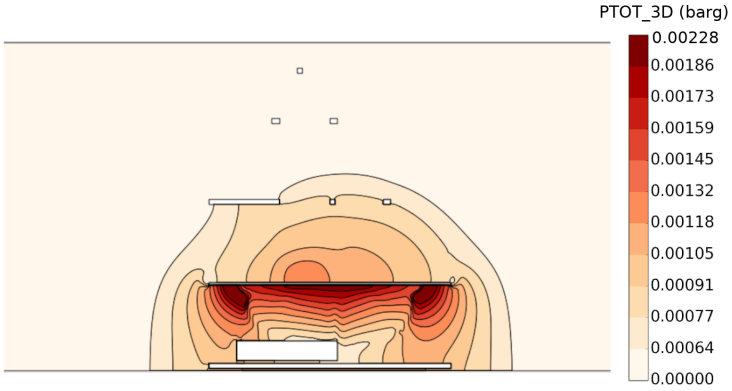

(b)

Figure 6.22: Pressure profile of gas explosion simulations in the process module using (a) STOKES with BML-hybrid at 0.360 s; and (b) FLACS at 2.162 s with uniform grid.

Table 6.2: Summary of mesh details and maximum overpressures obtained from FLACS simulations in the chemical process module case.

Case	Δx (m)	Domain dim. (m)	Stretch inc. (%)	Max. overpressure (mbar)
1	0.50	170 x 110 x 65	-	10.0
2	0.50	170 x 110 x 65	20	15.7
3	0.50	360 x 180 x 60.5	20	16.0
4	0.25	360 x 180 x 60.5	20	12.0
5	0.15	360 x 180 x 60.5	20	21.3

peak reaches 12 mbar. At last, the refined case ($\Delta x = 0.15$ m, Figure 6.24d) with the same domain volume as Figure 6.24d, deviates 77.5% from the previous one, reaching a maximum overpressure peak of 21.3 mbar. Therefore, it becomes clear that no grid independence is attained within the mesh sizes considered. Mesh sizes smaller than 0.15 m could not be run considering the current lab computational resources.

From Table 6.2 it is possible to realise that none of the FLACS simulations produced a maximum overpressure close to those observed in STOKES simulation. It is important to bear in mind that the overpressures presented in Table 6.2 were extracted from Figure 6.24 and therefore they correspond to the maximum overpressure reached in

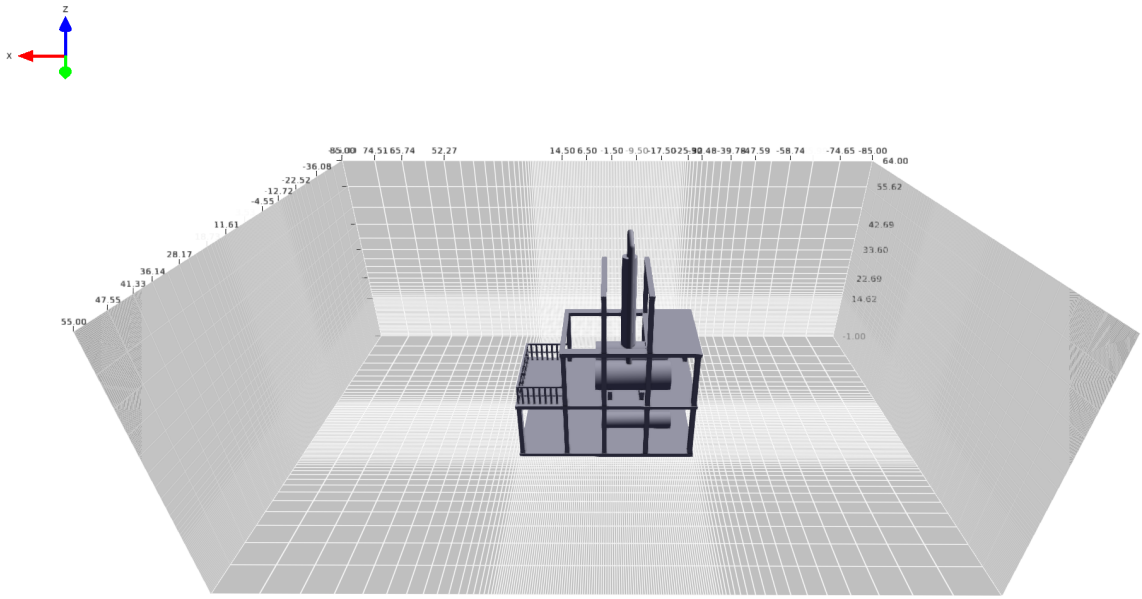

Figure 6.23: Grid lines of FLACS simulation in planes XY (Z = -1 m), YZ (X = 85 m and X = -85 m) and XZ (Y = -55 m) mesh size of 0.50 m in flammable region, with 20% stretch growth.

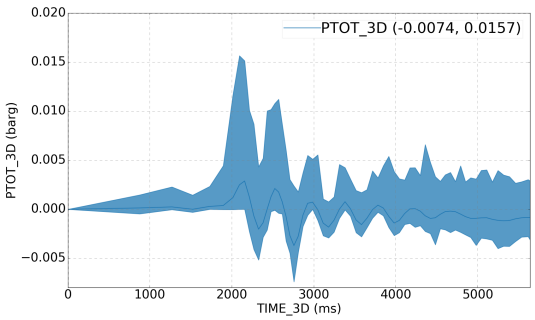

(a) $\Delta x = 0.50$ m, domain 170 x 110 x 65 m.

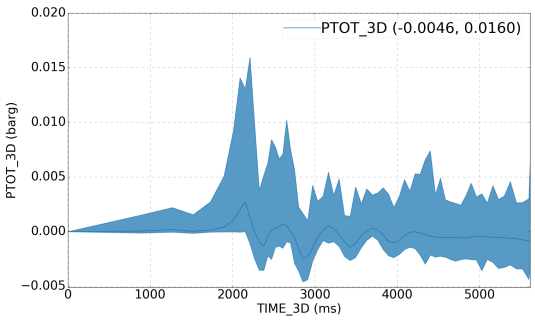

(b) $\Delta x = 0.50$ m, domain 360 x 180 x 60.5 m.

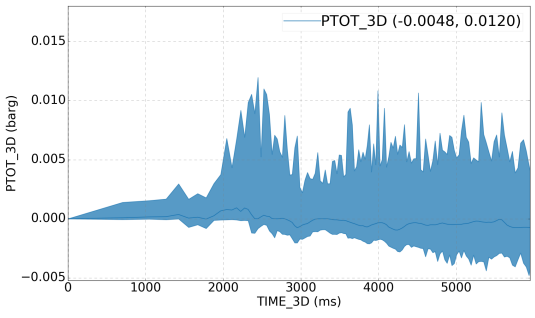

(c) $\Delta x = 0.25$ m, domain 360 x 180 x 60.5 m.

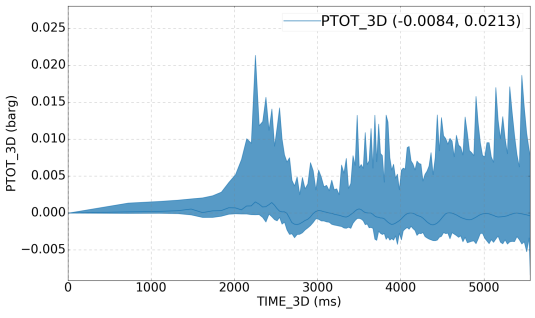

(d) $\Delta x = 0.15$ m, domain 360 x 180 x 60.5 m.

Figure 6.24: Total overpressure in FLACS simulations using stretched meshes and different domain volumes.

the whole domain. These values can be qualitatively compared to STOKES results using the BML-hybrid presented in Figure 6.17c, where the maximum overpressure of 150 mbar was attained.

Comments on the limitations of FLACS

At this point it is important to highlight the limitations of FLACS when simulating gas explosions. In the User's Manual v10.7, there are a few points which require attention. The first and most important refers to the grid guidelines, stressing that grid sizes smaller than 0.20 m should be avoided. This restriction is related to the nature of FLACS subgrid models, which are probably calibrated to larger geometries, where meshes larger than 0.20 are expected. Also, it is said that convergence of results with increasing spatial and temporal resolution cannot be expected for gas explosion simulations (GEXCON, 2018).

Other very important issues of FLACS include overpressure underprediction in unconfined congested geometries and very high quasi-laminar burning velocities in narrow channels and pipes. These, along with the mesh size limitations, corroborate with most of the results obtained in the present work using FLACS.

Therefore, FLACS limitations in predicting flame position and pressures in the combustion chambers cases, may be related to the reduced mesh sizes of 1-2 mm. Also, the chambers can be considered as narrow channels, where the high values of the quasi-laminar burning velocities may be related to the significantly overpredicted results.

At last, the analysis of FLACS results in the chemical process module case should take into consideration the software limitation when simulating gas explosions in unconfined congested geometries. Even though the module is taken as semi-confined with low degree of congestion, all overpressures predicted by FLACS seem to be quite low. This is however an assumption solely based on the significantly large flammable volume of 18432 m^3 at stoichiometric proportions (Figure 5.3), since there are no experimental measures to validate neither of the simulations in the chemical process module case.

7 Conclusions and future work

A few general conclusions can be drawn based on the simulation results presented in this work. The first is that the proposed BML-dynamic-I_0 may not have been the most coherent approach to incorporate the effects of stretch due to strain in the BML model, and further work on this matter is required. The second is that the fractal-based approach for the BML-hybrid seemed to be a promising alternative to the use of empirical correlations in the model. The BML-hybrid was able to reduce the number of adjustable constants, but dependency on c_L calibration still remains.

7.1 BML-dynamic-I_0

The results obtained from the BML-dynamic-I_0 model showed a slightly improvement in the corresponding flame time arrivals for Chambers 1, and 2. However, no significant change in the curves trend were noticed, leading to nearly unchanged flame speed histories. In fact, flame position history in Chamber 3 presented an abnormal peak, which is incompatible with the corresponding experimental data. This was probably responsible for a loss of agreement in the flame speed trend of Chamber 3 case.

The BML-dynamic-I_0 simulations showed an unexpectedly enlarged flame region, which is especially observed near the recirculation zones behind the obstacles and at the ignition point, where the turbulent flow field intensifies. This analysis indicates that the model acts to diminish the turbulent rate of reaction in the areas of the chambers where the turbulent flow field is more pronounced. Since the proposed dynamic stretch factor is given by a normalisation of the local divergence of velocity to the maximum divergence of velocity, it is expected that the stretch factor would be lowered by intense divergence and turbulent fields.

Furthermore, there seems to exist some inconsistencies on the physical argument used to the development of the BML-dynamic-I_0 based purely on strain leading to a local reduction of reaction rates. As previously discussed, in order to achieve a reduction on the reaction rate by inserting the effects of stretch, curvature should be taken into consideration.

In this sense, it is suggested that the normalisation of the divergence of velocity should be revised and future work may look into other approaches based perhaps on non-dimensional numbers of the flow, such as the local Lewis number, which has been proven to be greatly connected to the curvature effects.

7.2 BML-hybrid

Considering the analysis of the numerical simulations conducted in STOKES, it is possible to conclude that the proposed BML-hybrid presents the best results for explosion simulation in partially obstructed chambers of relatively small sizes. Best agreement is attained with respect to flame position and flame speed time histories. This represents an improvement from the originally implemented model (BML-Abu-Orf), which considers an empirical correlation for the modelling of the integral length of wrinkling.

In regard to the overpressure prediction, the BML-hybrid was able to significantly improve the maximum overpressure peak for Chamber 1, in comparison to the BML-Abu-Orf, which greatly overestimated the peaks for this case. Both models struggled to reproduce the maximum overpressure for Chamber 3, where an underestimation of about 75% was observed.

However, the improved results of the BML-hybrid approach are obtained once adjustments in the laminar burning model are conducted. In fact, prior to the laminar phase analysis, the BML-hybrid presented even higher dependency on the constant c_L than the original BML-Abu-Orf. This is because the fractal approach of the BML-hybrid retrieves a direct dependency on the turbulence length scales.

Nevertheless, the improved BML-hybrid is considered to embody the adjusted laminar model parameters so that a clear comparison to the original version of STOKES could be performed. Future work may include the calibrated laminar burning model with the empirical correlation of Abu-Orf & Cant (2000).

After extensive analysis in small combustion chambers, the BML-hybrid with the calibrated laminar phase was applied to the large-scale process module. Qualitative representation of flame evolution is well represented when compared to the corresponding FLACS simulation. However, the BML-hybrid model presented faster flame development in the early stages of propagation, which may be influenced by the limitations of the ignition model. Future works on this matter should address the need for large ignition radii and times.

Another important conclusion is drawn from the process module case. After some time, the maximum turbulent Reynolds number drops below the threshold value for the laminar-to-turbulent transition of propagation, meaning that the flame grows only on the account of the laminar burning model. Even though the module geometry presents a moderate degree of confinement, where the Re_t number is not expected to be significant, the turbulent reaction rate should be dominant.

In this sense, the present work provides enough evidence to support the hypothesis that a blending function based on the local turbulent Reynolds number may not be adequate to simulate explosions in geometries with a low degree of confinement, as in the case of the process module. This raises concern of a blending function based on the

local values of Re_t.

Bibliography

ABDEL-GAYED, R.; BRADLEY, D.; LAWES, M. Turbulent burning velocities: a general correlation in terms of straining rates. *Proceedings of the Royal Society of London. A. Mathematical and Physical Sciences*, The Royal Society London, v. 414, n. 1847, p. 389–413, 1987.

ABU-ORF, G. M.; CANT, R. S. A turbulent reaction rate model for premixed turbulent combustion in spark-ignition engines. *Combustion and flame*, Elsevier, v. 122, n. 3, p. 233–252, 2000.

AHMED, U.; HERBERT, A.; CHAKRABORTY, N.; KLEIN, M. On the validity of damköhler's second hypothesis in statistically planar turbulent premixed flames in the thin reaction zones regime. *Proceedings of the Combustion Institute*, Elsevier, 2020.

ALURI, N. K.; MUPPALA, S. R.; DINKELACKER, F. Substantiating a fractal-based algebraic reaction closure of premixed turbulent combustion for high pressure and the lewis number effects. *Combustion and Flame*, Elsevier, v. 145, n. 4, p. 663–674, 2006.

ARNTZEN, B. J. Modelling of turbulence and combustion for simulation of gas explosions in complex geometries. Norges teknisk-naturvitenskapelige universitet, 1998.

ATKINSON, G.; CUSCO, L. Buncefield: A violent, episodic vapour cloud explosion. *Process Safety and Environmental Protection*, Elsevier, v. 89, n. 6, p. 360–370, 2011.

BELL, J. B.; DAY, M. S.; GRCAR, J. F. Numerical simulation of premixed turbulent methane combustion. *Proceedings of the Combustion Institute*, Elsevier, v. 29, n. 2, p. 1987–1993, 2002.

BIRKBY, P.; CANT, R.; SAVILL, A. The application of a laminar flamelet model to confined explosion hazards. *Flow, turbulence and combustion*, Springer, v. 63, n. 1-4, p. 361, 2000.

BRAY, K.; CHAMPION, M.; LIBBY, P. A. The interaction between turbulence and chemistry in premixed turbulent flames. In: *Turbulent Reactive Flows*. [S.l.]: Springer, 1989. p. 541–563.

BRAY, K.; LIBBY, P. A.; MOSS, J. Flamelet crossing frequencies and mean reaction rates in premixed turbulent combustion. *Combustion Science and Technology*, Taylor & Francis, v. 41, n. 3-4, p. 143–172, 1984.

BRAY, K. N. C. Studies of the turbulent burning velocity. *Proceedings of the Royal Society of London. Series A: Mathematical and Physical Sciences*, The Royal Society London, v. 431, n. 1882, p. 315–335, 1990.

BRAY, K. N. C.; CANT, R. Some applications of kolmogorov's turbulence research in the field of combustion. *Proceedings of the Royal Society of London. Series A: Mathematical and Physical Sciences*, The Royal Society London, v. 434, n. 1890, p. 217–240, 1991.

CAI, X.; LIANG, J.; DEITERDING, R.; MAHMOUDI, Y.; SUN, M. Experimental and numerical investigations on propagating modes of detonations: Detonation wave/boundary layer interaction. *Combustion and flame*, Elsevier, v. 190, p. 201–215, 2018.

CANT, R.; BRAY, K. A theoretical model of premixed turbulent combustion in closed vessels. *Combustion and flame*, Elsevier, v. 76, n. 3-4, p. 243–263, 1989.

CANT, R.; MASTORAKOS, E. *An introduction to turbulent reacting flows*. [S.l.]: Imperial College Press, 2008.

CHAKRABORTY, N.; ALWAZZAN, D.; KLEIN, M.; CANT, R. S. On the validity of damköhler's first hypothesis in turbulent bunsen burner flames: A computational analysis. *Proceedings of the Combustion Institute*, Elsevier, v. 37, n. 2, p. 2231–2239, 2019.

CHAKRABORTY, N.; CANT, R. Effects of lewis number on flame surface density transport in turbulent premixed combustion. *Combustion and Flame*, Elsevier, v. 158, n. 9, p. 1768–1787, 2011.

CHANG, N.; SHY, S.; YANG, S.; YANG, T. Spatially resolved flamelet statistics for reaction rate modeling using premixed methane-air flames in a near-homogeneous turbulence. *Combustion and flame*, Elsevier, v. 127, n. 1-2, p. 1880–1894, 2001.

CHEN, Y.-C.; MANSOUR, M. S. Geometric interpretation of fractal parameters measured in turbulent premixed bunsen flames. *Experimental thermal and fluid science*, Elsevier, v. 27, n. 4, p. 409–416, 2003.

CHEW, T.; BRAY, K.; BRITTER, R. Spatially resolved flamelet statistics for reaction rate modeling. *Combustion and Flame*, Elsevier, v. 80, n. 1, p. 65–82, 1990.

CICCARELLI, G.; DOROFEEV, S. Flame acceleration and transition to detonation in ducts. *Progress in energy and combustion science*, Elsevier, v. 34, n. 4, p. 499–550, 2008.

COATES, A. M.; MATHIAS, D. L.; CANTWELL, B. J. Numerical investigation of the effect of obstacle shape on deflagration to detonation transition in a hydrogen–air mixture. *Combustion and Flame*, Elsevier, v. 209, p. 278–290, 2019.

CONTROL OF MAJOR ACCIDENTS. *Buncefield: Why did it happen?* [S.l.]: HSE Bootle, 2011.

DAMKöHLER, G. The effect of turbulence on the flame velocity in gas mixtures. 1940.

DAVIDSON, P. A. *Turbulence: an introduction for scientists and engineers*. [S.l.]: Oxford university press, 2015.

DOUNIA, O.; VERMOREL, O.; MISDARIIS, A.; POINSOT, T. Influence of kinetics on ddt simulations. *Combustion and Flame*, Elsevier, v. 200, p. 1–14, 2019.

DRISCOLL, J. F. Turbulent premixed combustion: Flamelet structure and its effect on turbulent burning velocities. *Progress in Energy and Combustion Science*, Elsevier, v. 34, n. 1, p. 91–134, 2008.

ECKHOFF, R. K. *Explosion hazards in the process industries*. [S.l.]: Gulf Professional Publishing, 2016.

EMAMI, S.; MAZAHERI, K.; SHAMOONI, A.; MAHMOUDI, Y. Les of flame acceleration and ddt in hydrogen–air mixture using artificially thickened flame approach and detailed chemical kinetics. *international journal of hydrogen energy*, Elsevier, v. 40, n. 23, p. 7395–7408, 2015.

FERREIRA, T. D. *Development of a 3D Navier-Stokes solver combined with the Gilbert-Johnson-Keerthi Distance Algorithm for simulation of turbulent reacting flow in complex geometries*. Tese (Doutorado) — University of Campinas, 2018.

FERREIRA, T. D.; SANTOS, R. G.; VIANNA, S. S. V. A coupled finite volume method and gilbert–johnson–keerthi distance algorithm for computational fluid dynamics modelling. *Computer Methods in Applied Mechanics and Engineering*, Elsevier, v. 352, p. 417–436, 2019.

FERREIRA, T. D.; VIANNA, S. S. Collision of convex objects for calculation of porous mesh in gas explosion simulation. *Journal of Loss Prevention in the Process Industries*, Elsevier, p. 104347, 2020.

FERREIRA, T. D.; VIANNA, S. S. V. The gilbert johnson keerthi distance algorithm coupled with computational fluid dynamics applied to gas explosion simulation. *Process Safety and Environmental Protection*, Elsevier, v. 130, p. 209–220, 2019.

FROUZAKIS, C. E.; FOGLA, N.; TOMBOULIDES, A. G.; ALTANTZIS, C.; MATALON, M. Numerical study of unstable hydrogen/air flames: shape and propagation speed. *Proceedings of the combustion institute*, Elsevier, v. 35, n. 1, p. 1087–1095, 2015.

GEXCON, A. Flacs v10.7 user's manual. *Confidential report, Gexcon AS, Norway*, 2018.

GOULDIN, F.; BRAY, K.; CHEN, J.-Y. Chemical closure model for fractal flamelets. *Combustion and flame*, Elsevier, v. 77, n. 3-4, p. 241–259, 1989.

GOULDIN, F. C. An application of fractals to modeling premixed turbulent flames. *Combustion and flame*, Elsevier, v. 68, n. 3, p. 249–266, 1987.

GUBBA, S. R.; IBRAHIM, S. S.; MALALASEKERA, W.; MASRI, A. R. Measurements and les calculations of turbulent premixed flame propagation past repeated obstacles. *Combustion and Flame*, Elsevier, v. 158, n. 12, p. 2465–2481, 2011.

IBRAHIM, S. S.; GUBBA, S. R.; MASRI, A. R.; MALALASEKERA, W. Calculations of explosion deflagrating flames using a dynamic flame surface density model. *Journal of Loss Prevention in the Process Industries*, Elsevier, v. 22, n. 3, p. 258–264, 2009.

KENT, J.; MASRI, A.; STARNER, S.; IBRAHIM, S. A new chamber to study premixed flame propagation past repeated obstacles. In: THE UNIVERSITY OF ADELAIDE ADELAIDE, AUSTRALIA. *5th Asia-Pacific conference on combustion*. [S.l.], 2005. p. 17–20.

KULKARNI, T.; BISETTI, F. Surface morphology and inner fractal cutoff scale of spherical turbulent premixed flames in decaying isotropic turbulence. *Proceedings of the Combustion Institute*, Elsevier, 2020.

LAI, J.; KLEIN, M.; CHAKRABORTY, N. Direct numerical simulation of head-on quenching of statistically planar turbulent premixed methane-air flames using a detailed chemical mechanism. *Flow, Turbulence and Combustion*, Springer, v. 101, n. 4, p. 1073–1091, 2018.

LEES, F. *Lees' Loss prevention in the process industries: Hazard identification, assessment and control*. [S.l.]: Butterworth-Heinemann, 2012.

LI, R.; MALALASEKERA, W.; IBRAHIM, S.; LIU, B. On the mechanism of pressure rise in vented explosions: A numerical study. *Process Safety and Environmental Protection*, Elsevier, v. 117, p. 551–564, 2018.

LINDSTEDT, R.; VAOS, E. Modeling of premixed turbulent flames with second moment methods. *Combustion and flame*, Elsevier, v. 116, n. 4, p. 461–485, 1999.

LIPATNIKOV, A. N.; CHAKRABORTY, N.; SABELNIKOV, V. A. Transport equations for reaction rate in laminar and turbulent premixed flames characterized by non-unity lewis number. *International Journal of Hydrogen Energy*, Elsevier, v. 43, n. 45, p. 21060–21069, 2018.

MOLKOV, V.; CIRRONE, D.; SHENTSOV, V.; DERY, W.; KIM, W.; MAKAROV, D. Dynamics of blast wave and fireball after hydrogen tank rupture in a fire in the open atmosphere. *International Journal of Hydrogen Energy*, Elsevier, 2020.

NIVARTI, G.; CANT, S. Direct numerical simulation of the bending effect in turbulent premixed flames. *Proceedings of the Combustion Institute*, Elsevier, v. 36, n. 2, p. 1903–1910, 2017.

NIVARTI, G. V. *The bending effect in turbulent flame propagation*. Tese (Doutorado) — University of Cambridge, 2017.

NIVARTI, G. V.; CANT, R. S. Scalar transport and the validity of damköhler's hypotheses for flame propagation in intense turbulence. *Physics of Fluids*, AIP Publishing LLC, v. 29, n. 8, p. 085107, 2017.

PATEL, S.; JARVIS, S.; IBRAHIM, S.; HARGRAVE, G. An experimental and numerical investigation of premixed flame deflagration in a semiconfined explosion chamber. *Proceedings of the Combustion Institute*, Elsevier, v. 29, n. 2, p. 1849–1854, 2002.

PETERS, N. Laminar flamelet concepts in turbulent combustion. In: ELSEVIER. *Symposium (International) on Combustion*. [S.l.], 1986. v. 21, n. 1, p. 1231–1250.

PETERS, N. Length and time scales in turbulent combustion. In: *Turbulent Reactive Flows*. [S.l.]: Springer, 1989. p. 242–256.

POINSOT, T.; VEYNANTE, D. *Theoretical and numerical combustion*. [S.l.]: RT Edwards, Inc., 2005.

POINSOT, T.; VEYNANTE, D.; CANDEL, S. Quenching processes and premixed turbulent combustion diagrams. *Journal of Fluid Mechanics*, Cambridge University Press, v. 228, p. 561–606, 1991.

POLE, S.; CHENG, W. Statistical calculations of spherical turbulent flames. In: ELSEVIER. *Symposium (International) on Combustion*. [S.l.], 1988. v. 21, n. 1, p. 1473–1481.

RANASINGHE, C. P.; MALALASEKERA, W. An improved formulation of the bray-moss-libby (bml) model for si engine combustion modelling. *Loughborough University*, 2017. Disponível em: ⟨https://hdl.handle.net/2134/26353⟩.

SARLI, V. D.; BENEDETTO, A. D.; RUSSO, G.; JARVIS, S.; LONG, E. J.; HARGRAVE, G. K. Large eddy simulation and piv measurements of unsteady premixed flames accelerated by obstacles. *Flow, turbulence and combustion*, Springer, v. 83, n. 2, p. 227–250, 2009.

SHY, S.; JANG, R.; GEE, K. *et al.* Three-dimensional spatial flamelet statistics for premixed turbulent combustion modeling. In: ELSEVIER. *Symposium (International) on Combustion*. [S.l.], 1996. v. 26, n. 1, p. 283–289.

SILGADO-CORREA, K. J.; FERREIRA, T. D.; VIANNA, S. S. Leak release momentum and the convective flow influence on the calculation of flammable cloud. *Journal of Loss Prevention in the Process Industries*, Elsevier, v. 65, p. 104123, 2020.

SILGADO-CORREA, K. J.; FERREIRA, T. D.; VIANNA, S. S. The nature of flammable cloud volumes in semi-confined environment under the influence of flow of air. *Journal of Loss Prevention in the Process Industries*, Elsevier, v. 68, p. 104293, 2020.

SPALDING, D. B. Development of the eddy-break-up model of turbulent combustion. In: ELSEVIER. *Symposium (International) on Combustion*. [S.l.], 1977. v. 16, n. 1, p. 1657–1663.

VIANNA, S. S.; CANT, R. S. Initial phase modelling in numerical explosion applied to process safety. *Process Safety and Environmental Protection*, Elsevier, v. 92, n. 6, p. 590–597, 2014.

VIANNA, S. S. V.; CANT, R. S. Modified porosity approach and laminar flamelet modelling for advanced simulation of accidental explosions. *Journal of loss prevention in the process industries*, Elsevier, v. 23, n. 1, p. 3–14, 2010.

ZIMONT, V.; BATTAGLIA, V. Joint rans/les approach to premixed flame modelling in the context of the tfc combustion model. *Flow, turbulence and combustion*, Springer, v. 77, n. 1-4, p. 305–331, 2006.

A Source code

This appendix shows parts of STOKES's source code where modifications were included as part of this work. Most of the code changes were performed in the subroutine `combustion.f90`, which is provided here in its complete version. Modifications in other subroutines are shown here only as separate code lines for the sake of brevity.

A.1 Combustion subroutine

```
subroutine  combustion(TIMEC,TIME_NC)
    use common_block
    implicit none
    real (kind = dp ) :: GSIGC1
    integer (kind = 4 ) :: NN
    real (kind = dp ) :: A,B,C,D,ALPHA,BETA
    real (kind = dp ) :: LFL,UFL,PREF,TREF,FST
    real (kind = dp ) :: HFUEL,CFUEL,HCOMB,RCONST
    real (kind = dp ) :: WMF,WMA,WMP,WMR
    real (kind = dp ) :: CPP,CPF,CPA,CPR,CVR,CVP
    real (kind = dp ) :: YFR,YFP,GAR,TUNB,E,ROT,PVAR,TEMP,TAUC
    real (kind = dp ) :: EQUIV,ROUNB,UP,TERM1,TERM2,TERM3,TERM4
    real (kind = dp ) :: FMU,EQAVG,TIMEC,TIME_NC
    real (kind = dp ) :: UL(NNODE),SPVLAM(NNODE),vaux(NNODE)
    real (kind = dp ) :: LTURB(NNODE),SIGMAL,TAYLORM,TERMOREY
    real (kind = dp ) :: LM(NNODE),ETA(NNODE),LG(NNODE)
    real (kind = dp ) :: PAUX,XNMAX,PAUX2,FACEL
    real (kind = dp ) :: DELTAS,DELTATF
    !
    !*********************************************************************
    !       COMBUSTION MODEL PARAMETERS
    !*********************************************************************

    GSIGC1 = GG/(SIGHAT*CC1)

    !       print*,'COMBUSTION CONSTANTS'
    !       print*, GG
    !       print*, SIGHAT
    !       print*, CC1
    !       print*, CW1
```

```
!       print*, CW2
!       print*, GSIGC1

!*****************************************************************
!       Set the fuel properties
!*****************************************************************
!
! METHANE
!
IF(FLUID.EQ.1) THEN

    LFL = 0.53
    UFL = 1.6
    PREF = 1.0E5
    TREF = 300.0
    FST = 0.054969543
    !
    HFUEL = 4.
    CFUEL = 1.

    WMF=16.04
    WMA=28.96
    WMP=27.63

    HCOMB=50.01E6
    RCONST=8.3135E3

    CPP=1.4896E3
    CPF=2.2537E3
    CPA=1.0045E3

    A = 0.6097
    B = -2.554
    C = 7.3105
    D = 1.2303
    ALPHA = 2.0
    BETA = -0.42

END IF

! PROPANE
```

```
!
IF(FLUID.EQ.2) THEN

    LFL = 0.52
    UFL = 2.4
    PREF = 1.0E5
    TREF = 300.0
    FST = 0.060218978
    !
    HFUEL=8.
    CFUEL=3.

    WMF=44.0
    WMA=28.96
    WMP=27.63

    PREF=1.0E5
    TREF=300.
    HCOMB=46.36E6
    RCONST=8.3135E3

    CPP=1.4896E3
    CPF=2.2537E3
    CPA=1.0045E3

    A = 0.42431
    B = 0.73447
    C = 4.50025
    D = 0.98129
    ALPHA = 1.77
    BETA = -0.25

END IF
!
!***********************************************************************

CVP=CPP-(RCONST/WMP)

!***********************************************************************
!       Calculate
!***********************************************************************
```

```
!
OPEN(unit=400,file='comb.dat')

! Make sure XNMAX is less than xtrans in cube.parameters.dat
XNMAX   = xtrans
PAUX2   = 0.0

DO NN=1,NNODE

    IF((FF(NN)/RO(NN).GT.0.03).AND.(FF(NN)/RO(NN).LT.0.085)) THEN

        EQUIV = FF(NN)/(RO(NN)-FF(NN))*(1.0-FST)/FST

        YFR = FF(NN)/RO(NN)
        YFP = WMF*AMAX1( 0.,0.5*(YFR*(HFUEL/4.+CFUEL)/WMF - &
            0.21*(1.-YFR)/WMA) )

        WMR = YFR*WMF+(1.-YFR)*WMA
        CPR = YFR*CPF+(1.-YFR)*CPA
        CVR = CPR-(RCONST/WMR)
        GAR = CPR/CVR
        !
        TUNB = TREF*(P(NN)/PREF)**((GAR-1.)/GAR)
        ROUNB = P(NN)*WMR/(RCONST*TUNB)

        TERM1 = A*(EQUIV**B)*EXP(-C*(EQUIV-D)*(EQUIV-D))
        TERM2 = ((TUNB/300.)**ALPHA)*((P(NN)/1.0E5)**BETA)
        UL(NN) = TERM1*TERM2
        UP = (2.*TK(NN)/(RO(NN)*3.))**0.5
        !
        E = 0.5*(VX(NN)**2. + VY(NN)**2. + VZ(NN)**2.)
        ROT = (ROE(NN)-RO(NN)*E)/CVP+TUNB*(RO(NN)-PV(NN))*(1.- &
             (CVR/CVP))-(HCOMB/CVP)*(YFR*(RO(NN)-PV(NN))+PV(NN)*YFP)
        TAUC = (ROT/TUNB-RO(NN)+(WMP/WMR-1.)*PV(NN))*WMR/(WMP*RO(NN))
        PVAR = PV(NN)/RO(NN)
        PVAR = min(max(PVAR,0.0),1.)

        IF(PVAR.LT.1e-4)PVAR=0.E0

        !*****************************************************************
        !Tassia: running different models for charact. length scale Ly
```

```
!*****************************************************************

!   Original code

!               TERM3   = 1./(1.+(CW1/(UP/UL(NN))))
!               TERM4   = 1.-EXP(-1./(1.+(CW2*(UP/UL(NN)))))
!               SPV(NN) = VOLN(NN)*TERM3*TERM4*UL(NN)/VMUL*PVAR* &
!                            (1.-PVAR)*ROUNB*UL(NN)*ROUNB

!   Fractal approach - Kolmogorov length scale as inner cut-off

!               LTURB(NN) = (UP**3.)/(TE(NN)/RO(NN))
!               ETA(NN)   = (VMUL**3./(TE(NN)/RO(NN)))**(0.25)
!               LM(NN)    = (LTURB(NN)/ETA(NN))**(0.33)

!   Fractal approach - Gibson length scale as inner cut-off

LTURB(NN) = (UP**3.)/(TE(NN)/RO(NN))
LG(NN)    = (UL(NN)**3.)/(TE(NN)/RO(NN))
LM(NN)    = (LTURB(NN)/LG(NN))**(0.33)

SPV(NN)   = VOLN(NN)*ROUNB*UL(NN)*ROUNB*PVAR*(1.-PVAR)* &
    UL(NN)/(VMUL*LM(NN))

SPV(NN)   = SPV(NN)*GSIGC1

!*****************************************************************
! Tassia: considering stretch factor in flame nodes
!*****************************************************************

!IF(PAUX.GE.0.37.AND.PAUX.LE.0.63)THEN
!    SPV(NN) = IO(NN)*SPV(NN)*GSIGC1
    !        write(555,"(i10,i20,e20.8)")NSTEP,NN,IO(NN)
!ELSE
!    SPV(NN) = SPV(NN)*GSIGC1
!END IF
!*****************************************************************

!              if(NN.eq.1) print*, GSIGC1

!            Calculate Turbulent Reynolds number
```

```
      TERMOREY = AMAX1(TE(NN),1.E3*RO(NN))
      RETT(NN) = 2.*TK(NN)*TK(NN)*(0.09**0.75)/( 3.*VMUL*TERMOREY)

      !           TDF - November 2017
      !            Calculate Damkholer and Karlovitz number

      !               SIGMAL = VMUL/UL(NN)

      DA(NN) = RETT(NN)*UL(NN)*UL(NN)/(UP*UP )
      !        KA(NN) = SIGMAL*UP/( UL(NN)*TAYLORM )

      KA(NN) = 1./DA(NN)

      !ssvv June 2017. Reynolds number calculation based on the
      ! Richardson energy cascade
      !               vaux(NN)=sqrt(VX(NN)**2+VY(NN)**2+VZ(NN)**2)
      !               RETT(NN) = (0.09*RO(NN)*TK(NN)**(2.0))/(VMUL* &
      !                           TE(NN))

      !           Quasi laminar burning velocity SQL

      !            SQL(NN) = UL(NN)*(1+2.*RIG)**(0.5)

      SPVLAM(NN) = VOLN(NN)*4.2*ROUNB*AFLAME*PVAR*(1.-PVAR)*UL(NN)/SUMSPV
      !            SPVLAM(NN) = VOLN(NN)*4.2*ROUNB*AFLAME*PVAR* &
      !                (1.-PVAR)*SQL(NN)/SUMSPV

      !****************************************************************
      ! Tassia: new Ret threshold for laminar-turbulent transition burn
      !****************************************************************

      !   FMU = AMAX1(0.,(1.-EXP(-0.008*(RETT(NN)-500.))))
      FMU = AMAX1(0.,(1.-EXP(-0.008*(RETT(NN)-2500.))))
      SPV(NN) = FMU*SPV(NN) + (1. - FMU)*SPVLAM(NN)

      !****************************************************************
      !   if (NSTEP.eq.2000)   write(400,*) SPVLAM(NN), RETT, FMU
    ELSE
      SPV(NN) = 0.0
    END IF
```

```
      !****************************************************************
      ! Tassia: Determining flame position
      !****************************************************************
      PAUX  = PV(NN)/RO(NN)
      IF((PAUX.GE.0.10).AND.(PAUX.LE.0.90)) THEN
          IF(XN(NN).GE.XNMAX) THEN
              XNMAX = XN(NN)
              PAUX2 = PAUX
          END IF
      ENDIF
      !****************************************************************

  END DO

  IF ( (TIMEC.GT.TIME_NC).AND.&
      ( (TIMEC - TIME_NC).LT.TIMEIG ) )THEN
      DO NN=1,NNODE
          IF((FF(NN)/RO(NN).GT.0.03).AND.(FF(NN)/RO(NN).LT.0.085)) THEN
              EQAVG = SQRT((XN(NN)-XIG)**2.+(YN(NN)-YIG)**2.+ &
                    (ZN(NN)-ZIG)**2.)
              IF(EQAVG.LT.RIG) THEN
                  PVAR = PV(NN)/RO(NN)
                  SPV(NN) = VOLN(NN)*(0.95 - PVAR)*1.0E3
              END IF
          ELSE
              SPV(NN) = 0.0
          END IF

          !****************************************************************
          ! Tassia: Determining flame position
          !!***************************************************************
          PAUX  = PV(NN)/RO(NN)
          IF((PAUX.GE.0.10).AND.(PAUX.LE.0.90)) THEN
              IF(XN(NN).GE.XNMAX) THEN
                  XNMAX = XN(NN)
                  PAUX2 = PAUX
              END IF
          ENDIF
          !****************************************************************
      END DO
```

```
END IF


!**********************************************************************
! Tassia: Calculating flame speed FVEL in m/s
!**********************************************************************

FPOS(NSTEP) = XNMAX
print*,"deltas= ",(FPOS(NSTEP)-FPOS(LCHANGE)),"lchange= ",LCHANGE, &
            "XN1(NSTEP)= ",FPOS(NSTEP),"XN1(LCHANGE)= ",FPOS(LCHANGE)
IF(FPOS(NSTEP).GT.FPOS(LCHANGE)) THEN
    FVEL(NSTEP)  = (FPOS(NSTEP)-FPOS(LCHANGE))/(NSTEP-LCHANGE)/DELTAT
    write(104,*) NSTEP,NSTEP*DELTAT,FPOS(NSTEP),FVEL(NSTEP)
    call flush (104)
    LCHANGE = NSTEP
END IF

!**********************************************************************
! Tassia: Measuring flame position
!**********************************************************************

! Writing flame position in file 101

write(101,*) PAUX2,NSTEP,NSTEP*DELTAT,FPOS(NSTEP)
call flush (101)
!**********************************************************************

return
END
```

A.2 Turbulence subroutine

```
DIVMAX=0.0
DO NC=1,NCELL
!**********************************************************************
! Tassia: maximum absolute value of divergence of velocity per iteration
!**********************************************************************

IF(ABS(DIV).GE.DIVMAX) THEN
    DIVMAX=ABS(DIV)
```

```
END IF
!*********************************************************************
    DO NN=1,8

        !*************************************************************
        ! Tassia: calculating local stretch factor I0
        !*************************************************************

        IF(NSTEP.GE.2) THEN
            I0(KK)=ABS(DIV)/DIVNSTEP(NSTEP-1)
            !               PRINT*,'stretch factor =',I0(KK)
        END IF
        !*************************************************************
    END DO
END DO
```

A.3 Solver subroutine

```
open(unit=101,file="flame_position",action="write",position="append")
open(unit=104,file="flame_speed",action="write",position="append")
open(unit=75,file="pressure",action="write",position="append")

TIME = 0.0

LCHANGE  = 1

DO 1000 NSTEP = 1,NSTEPS

    !*********************************************************************
    ! Monitoring pressure
    !*********************************************************************
    AVGP  = 0.0
    CONTA = 0
    MAXP1 = 0.0
    PMAX  = 0.0

    DO NN=1,NNODE
        EQAVG = SQRT((XN(NN)-XMON)**2.+(YN(NN)-YMON)**2.+(ZN(NN)-ZMON)**2.)
        IF(EQAVG.LT.RMON) THEN
            AVGP = AVGP + P(NN)
```

```
            CONTA = CONTA + 1.
            if (P(NN).gt.MAXP1) MAXP1 = P(NN)
        END IF
        if (P(NN).GT.PMAX)  PMAX  = P(NN)
    END DO

    MAXP2 = AVGP/real(CONTA)

    write(75,*) NSTEP, NSTEP*DELTAT, MAXP1, MAXP2, PMAX
    call flush (75)
    !*********************************************************************
```

B STOKES quick manual

This appendix serves as a tutorial for running a simple case in STOKES. All the steps that need to be followed, from the geometry design to the post-processing, are presented in this section, including orientation on how to install, customise and run additional packages. The information provided in this section refers to installation and running procedures within the GNU/Linux environment.

Before starting, the user should be in possession of the following files:

1. `mystl.zip`
2. `PDR-Flow-Solver.zip`
3. `solver_lam2_KA_DA_frac_fp_fs.zip`
4. `flow`

As good practice, it is recommended the creation of a main directory named **STOKES**, which should contain the directories **01–Geometry**, **02–Porosity**, **03–Simulation**, **04–Files**. The files listed above should be saved in the **04–Files** directory. Avoid the use of spaces, dots (.) and underscore (_) in folder names.

B.1 Geometry with Blender

The geometry design (CAD model) is performed within the free and open source software Blender. However, Blender needs to be customised in order to be able to export CAD files in the `.stl` format (stereolithography). This is performed by adding the `mystl` directory to the `Addons` directory in Blender. The following sections will cover Blender installation, customisation, and an example of geometry design and exportation as a `.stl` file.

B.1.1 Blender installation

In order to avoid compatibility problems, it is recommended that version **2.79b** is used. This is a previous Blender version which is no longer available from the repositories of GNU/Linux distributions. Because of that, the user should download the older version directly from Blender website:

`https://www.blender.org/download/previous-versions/`

where it is possible to have access to all versions of the **2.79** family:

`https://download.blender.org/release/Blender2.79/`

for a 64 bits computer with GNU/Linux distributions, the following file is recommended:

`blender-2.79b-linux-glibc219-x86_64.tar.bz2`

the compressed file can be saved in any desired directory. However, it is recommended that the compressed file is saved in a directory named **Blender** for tidiness purposes.

In **Blender** directory, right-click on the compressed file and click on **Extract Here**:

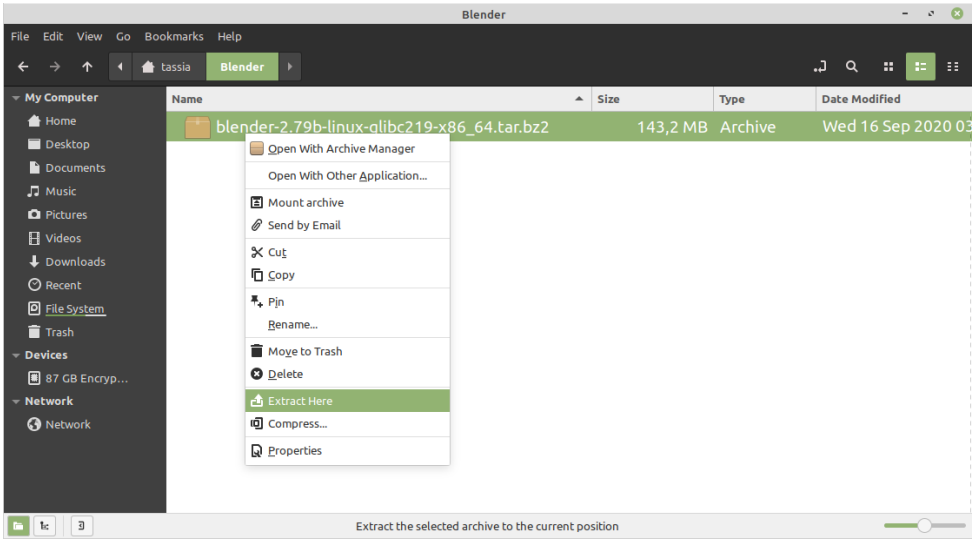

The extracted folder `blender-2.79b-linux-glibc219-x86_64` already contains the program itself, so no actual installation is needed. To open Blender, double-click on `blender-2.79b-linux-glibc219-x86_64` and then double-click on the executable `blender`:

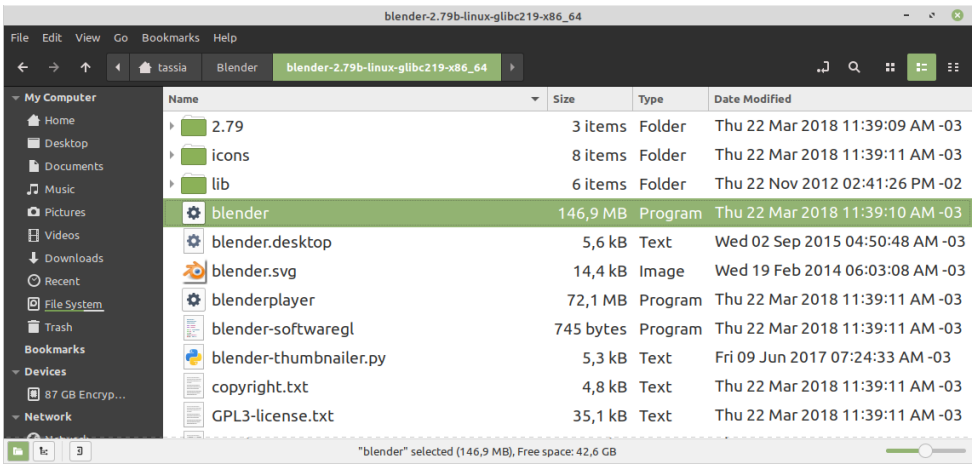

B.1.2 Customising Blender

In order to customise Blender to generate CAD files with the `.stl` format, the directory `mystl` must be added to Blender's `addons` directory.

The `addons` directory is located in the following path:

`/Blender/blender-2.79b-linux-glibc219-x86_64/2.79/scripts/addons`

In the directory `addons`, paste the directory `mystl`:

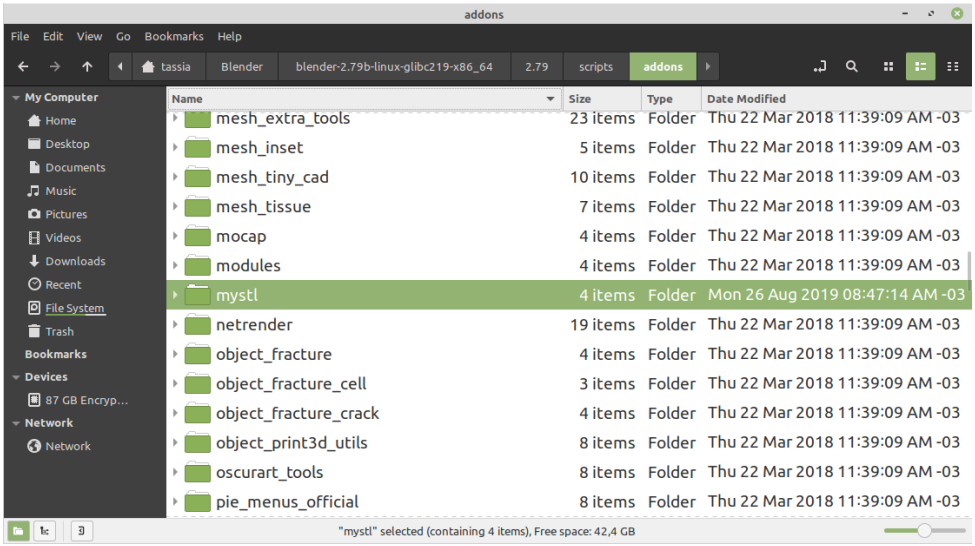

After that, go back to the root directory `blender-2.79b-linux-glibc219-x86_64` and double click on the executable `blender` to open Blender.

Once Blender is open, go to **File** > **User Preferences...** > **Addons**:

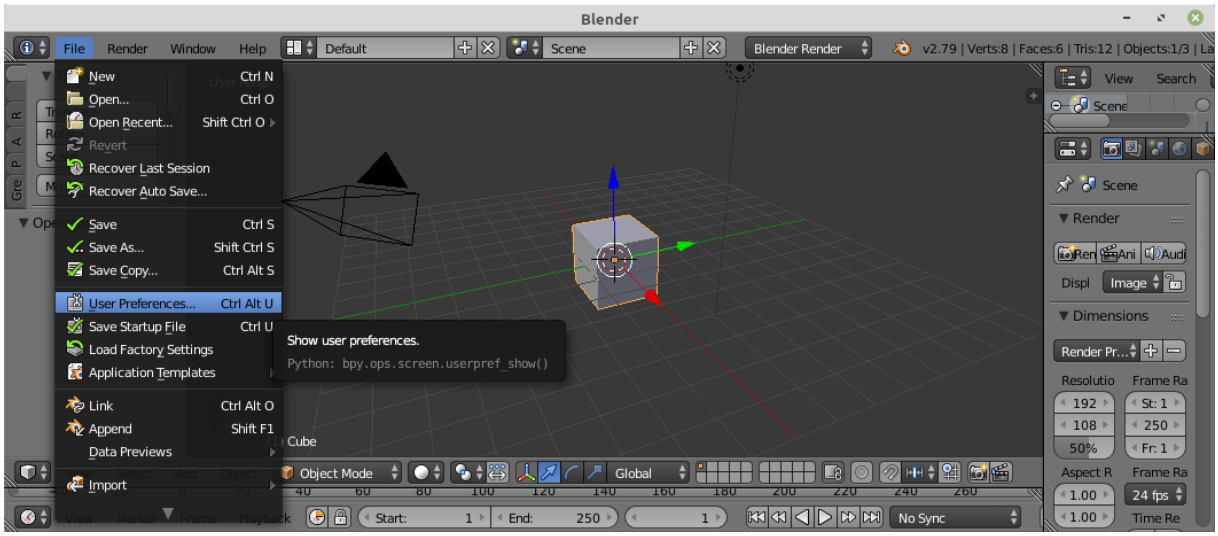

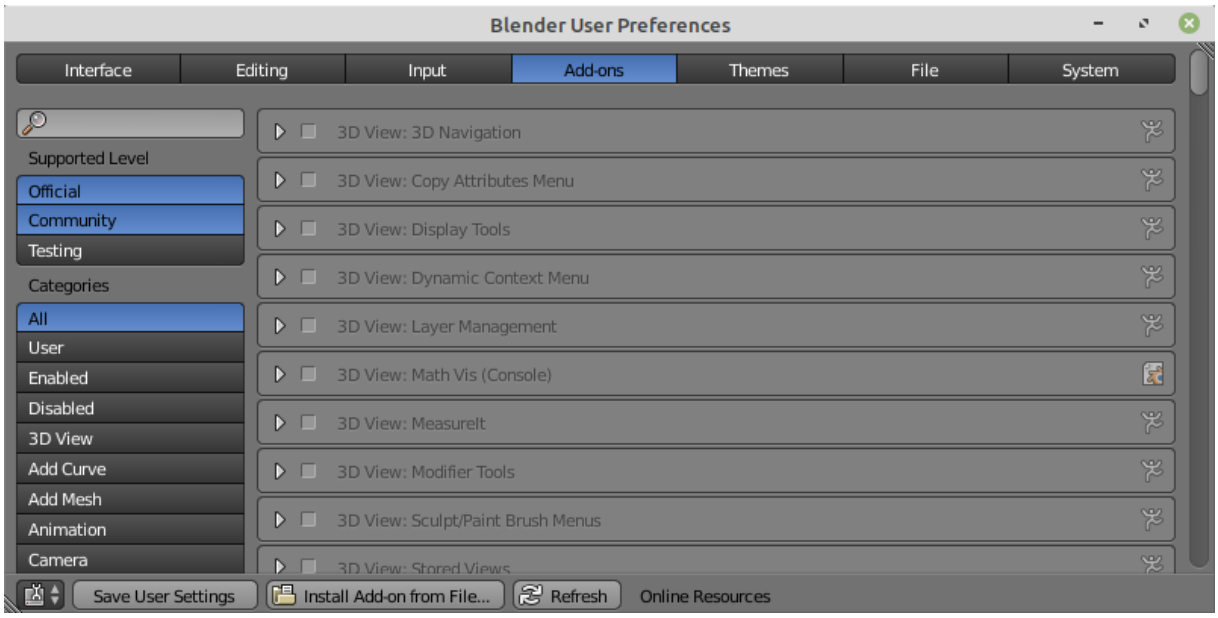

In **Addons**, scroll down and untick the **Import-Export: STL format** box and tick the new **Import-Export: My STL format** box:

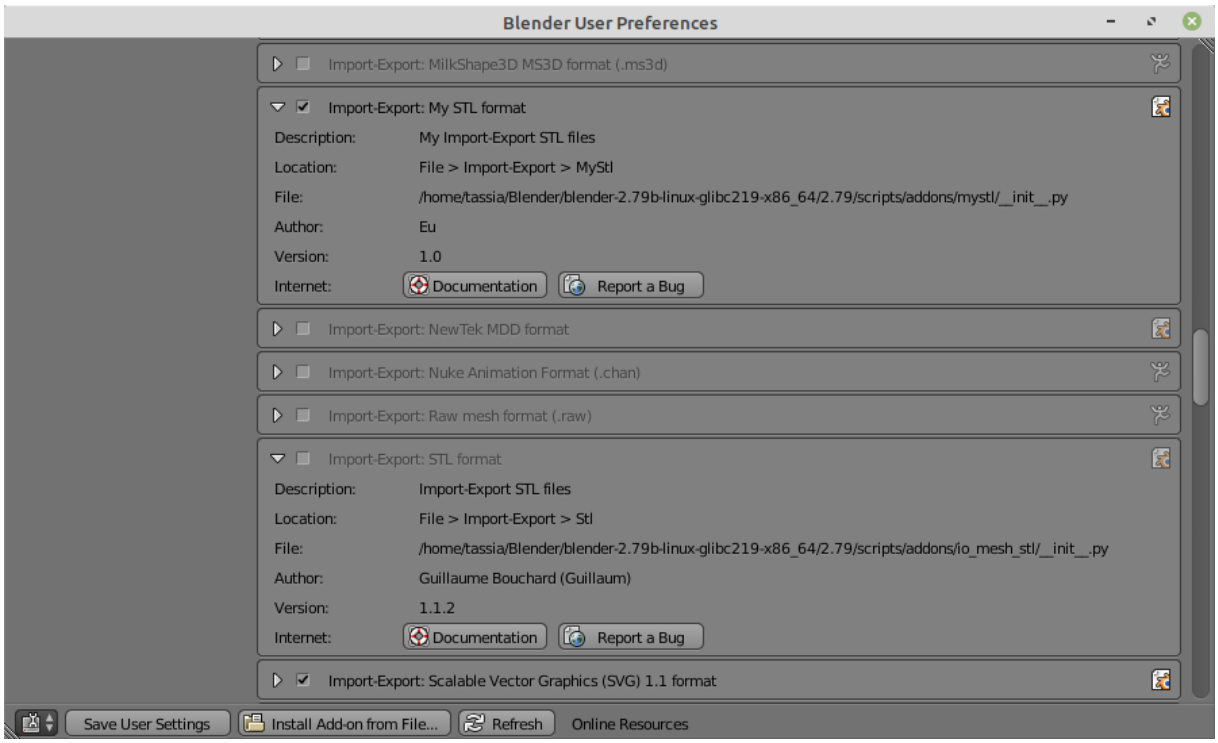

Before exiting the **Blender User Preferences** window, save changes by clicking on **Saver User Settings**.

Blender customisation is now finished.

B.1.3 Geometry design and export

Blender opens up with a default cubic object with edges of 2 m. This information is indicated in **Dimensions**, in the right-hand side **Transform** tab. It should be noted that by default the axes origin is located in the centre of the cube:

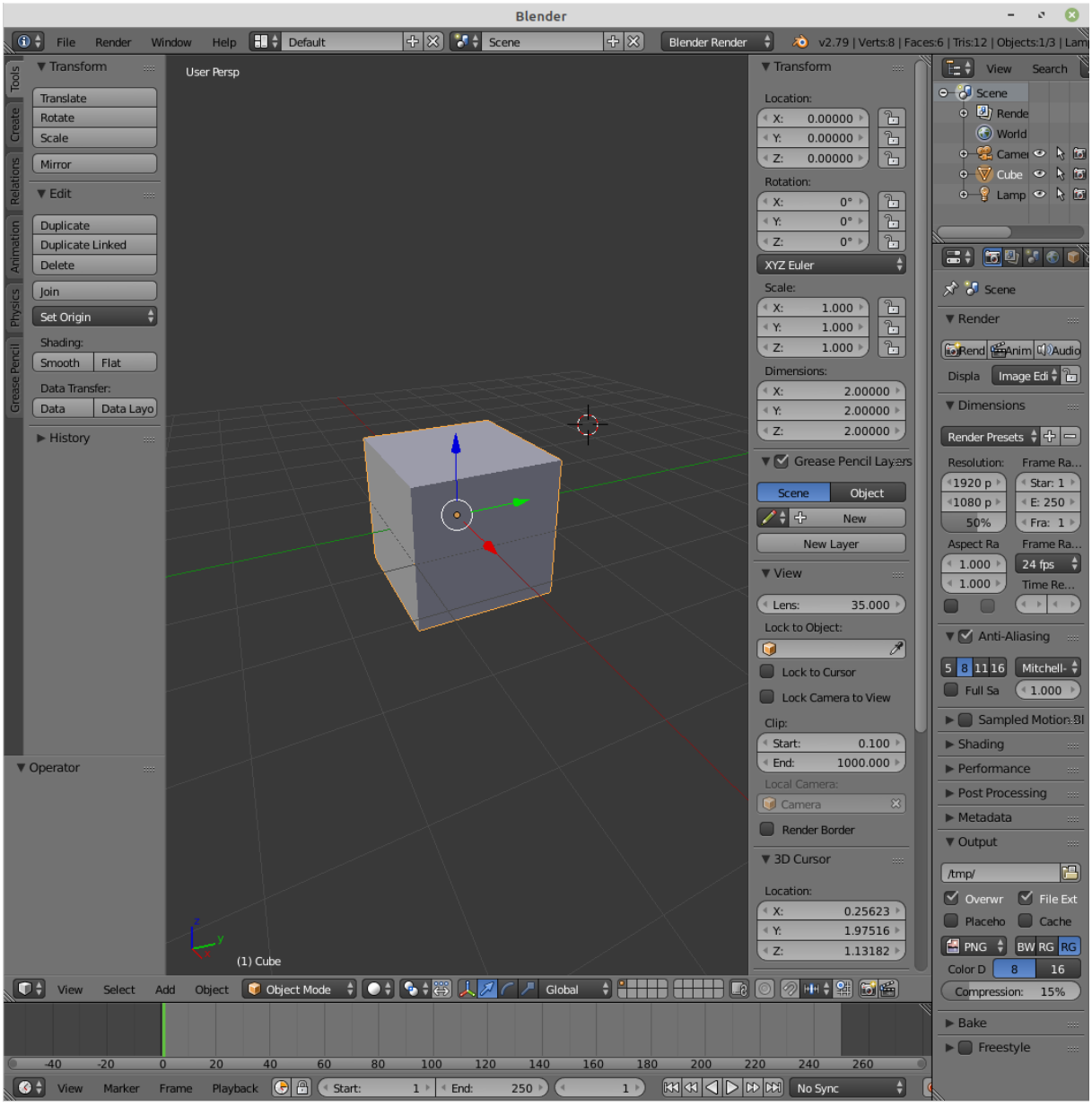

In this example, we are going to create a small cube with edges of 12 mm. This can be done by editing either the X, Y, Z fields of **Dimensions** or the X, Y, Z fields of **Scale**. However, **Dimensions** represent the whole edge of the cube, whereas **Scale** indicate half of the cube edge.

In the right-hand side **Transform** tab, set the X, Y, Z fields in **Dimensions** to the value of 0.012 m. Use the mouse scroll button to zoom in the cube region:

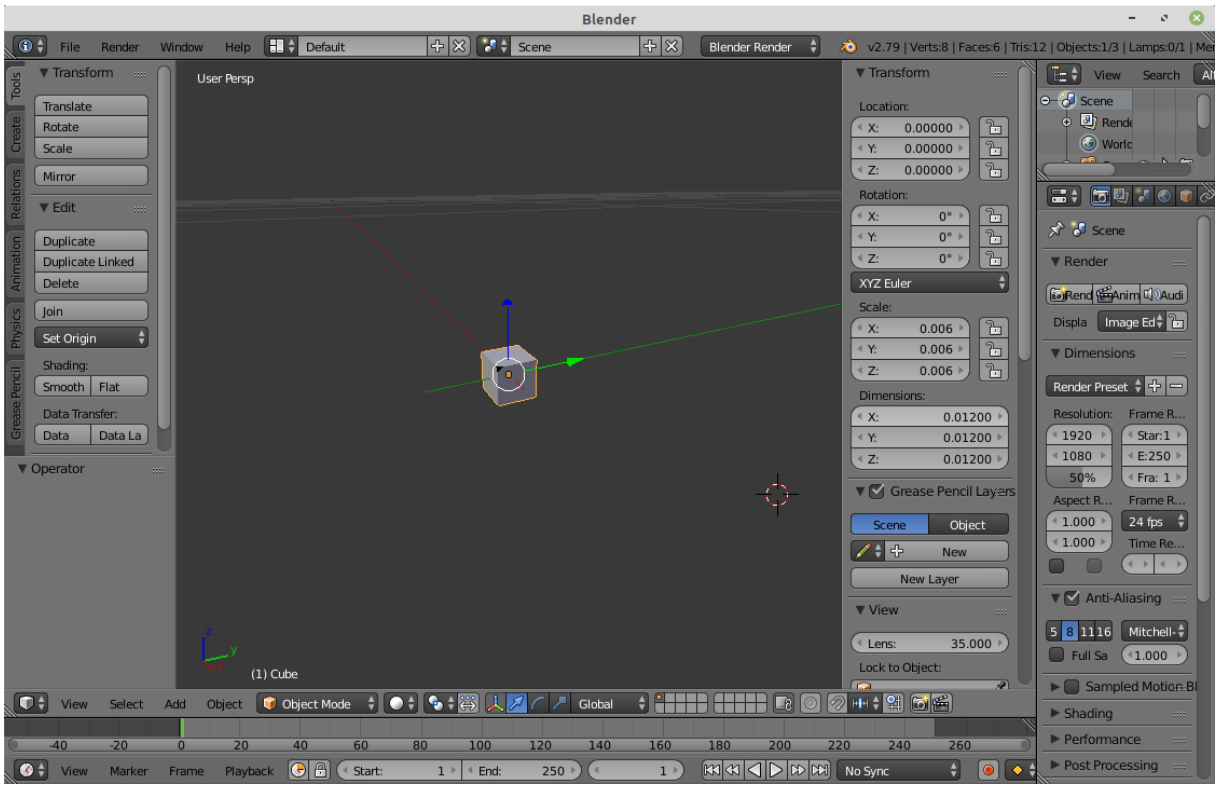

To export the geometry, go to **File** > **Export** > **Stl (.stl)**:

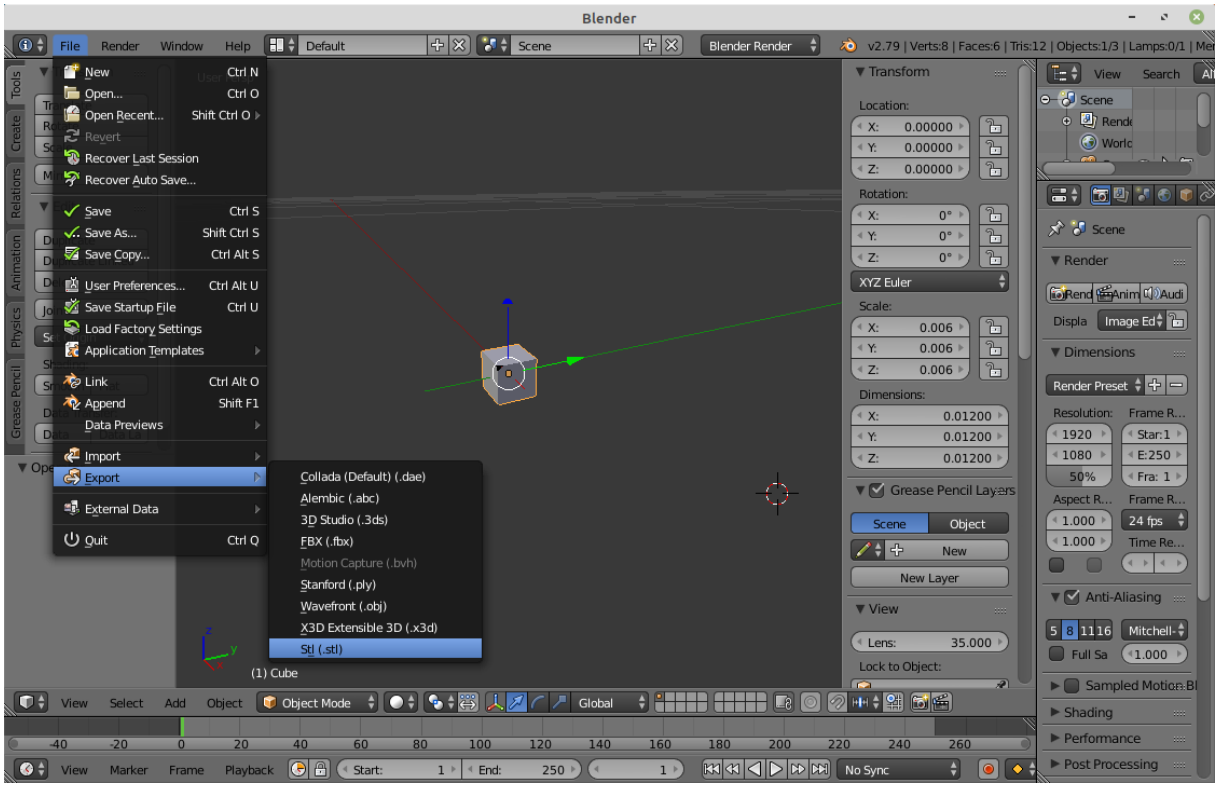

Tick the box **Ascii** in the bottom left-hand corner. Name the geometry as **cube.stl**, choose the directory **01-Geometry** and click on **Export STL**:

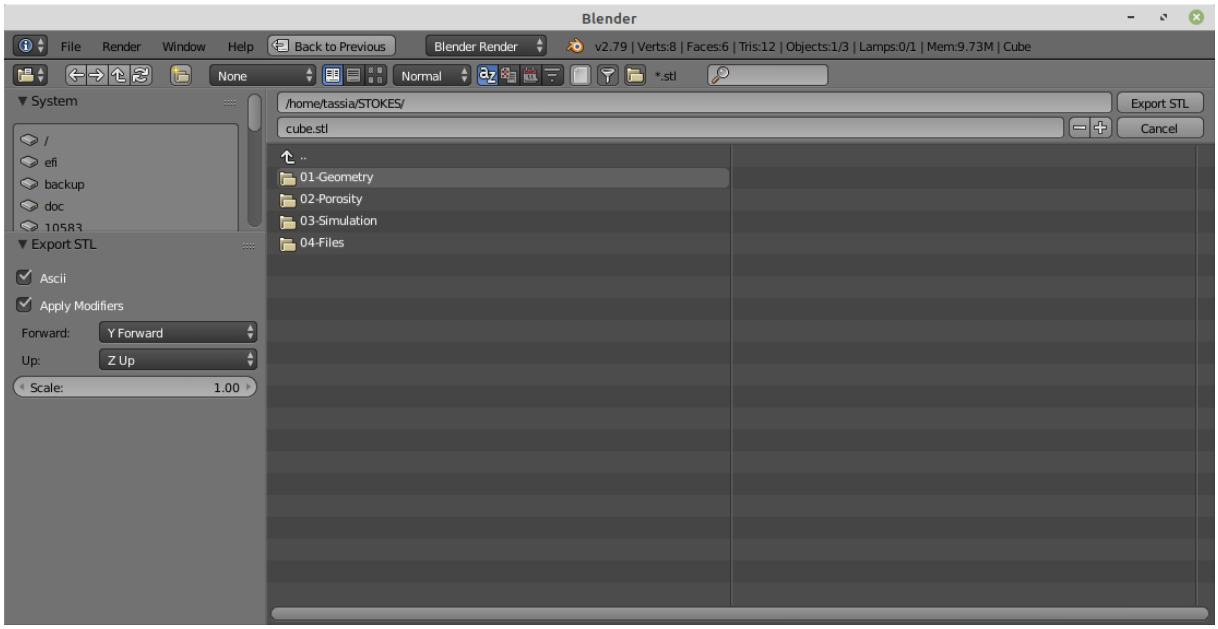

The geometry will be exported.

B.2 Porosity, domain and mesh with prePro

The definitions of domain dimensions, mesh spacing and porosity calculation are altogether performed with **prePro**. Before running **prePro**, the user needs to compile prePro to obtain an executable file by following the procedures below:

1. Go to **/STOKES/04-Files**, right-click on the compressed file **PDR–Flow–Solver.zip** and click on **Extract Here**:

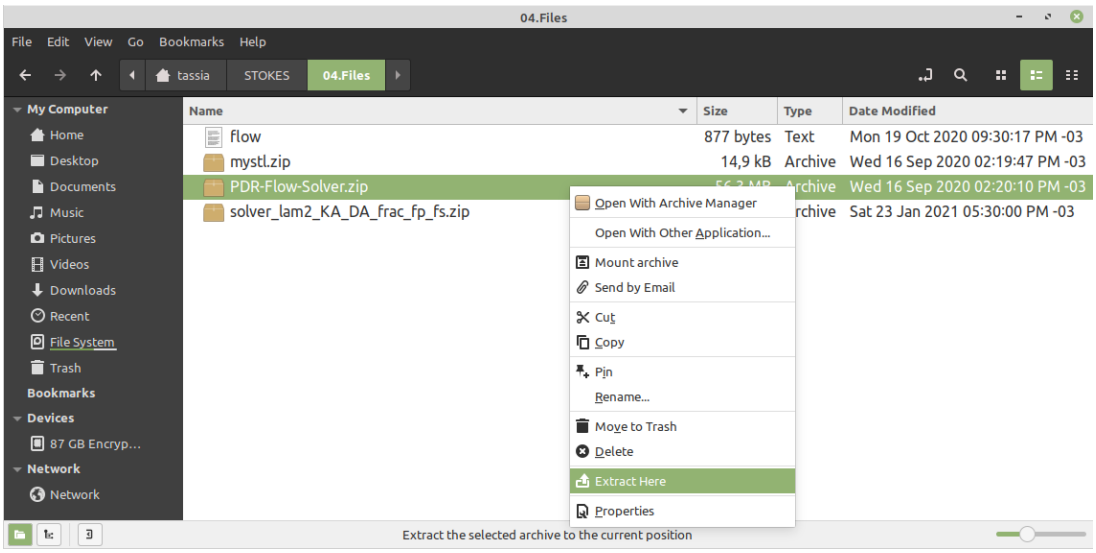

2. From the extracted **PDR-Flow-Solver** directory, right-click in any blank space to open the window options and then click on **Open in Terminal**:

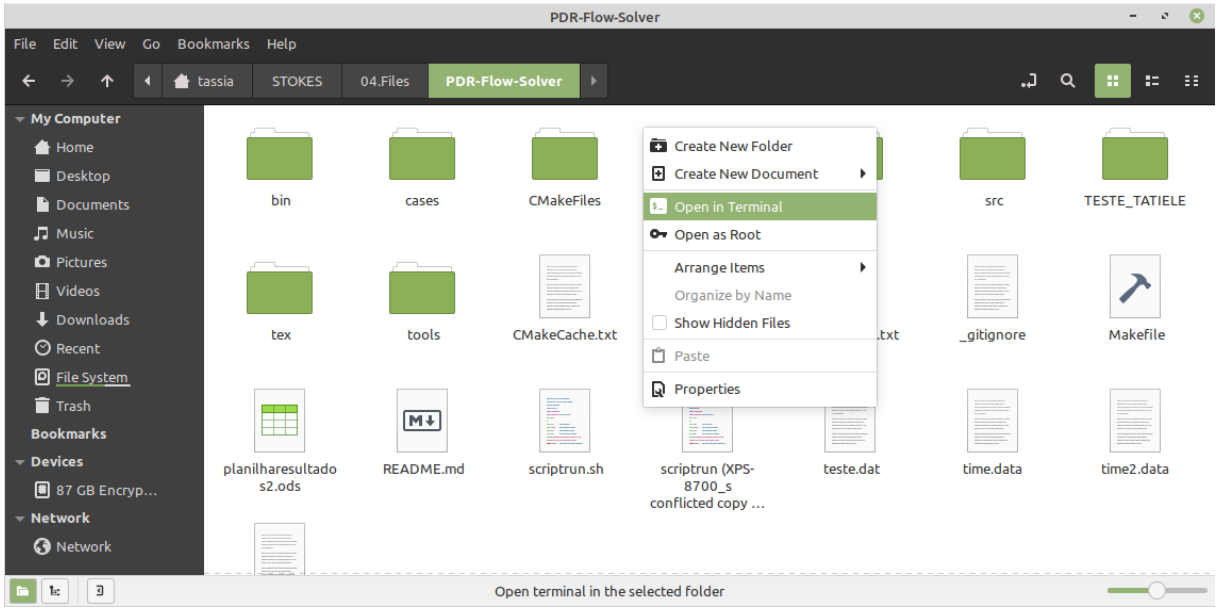

3. In the terminal, type to command **pwd**, hit **Enter**, and copy the path shown. Note that the popular copy & paste shortcut Ctrl+C, Ctrl+V does not work on Terminal. To copy the path shown, just make a selection:

4. Go back to the **PDR-Flow-Solver** directory and double-click to open the file **CMakeCache.txt**

5. With the **CMakeCache.txt** file open, press **Ctrl+H** on the keyboard to open a **Find and Replace** window

6. In the field **Find**, type the path **/home/victor/Dropbox/PDR-Flow-Solver**

7. In the field **Replace**, paste the path copied from terminal (step 3) by clicking with the mouse scroll button **/home/tassia/STOKES/04-Files/PDR-Flow-Solver**:

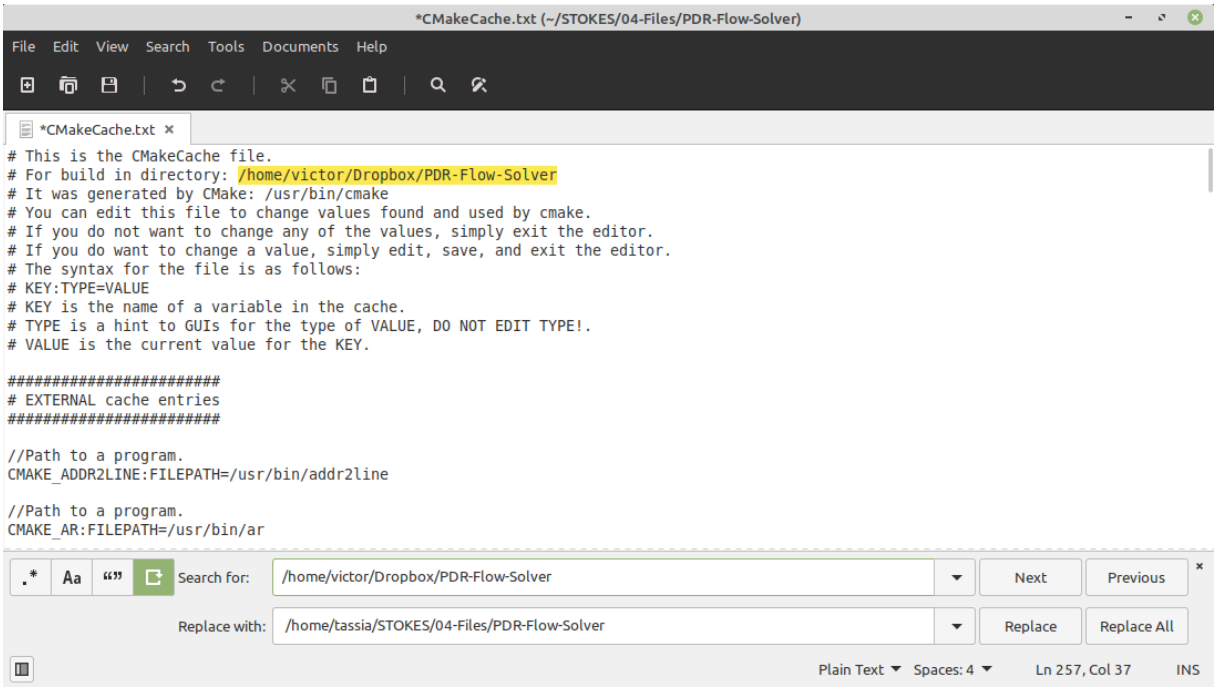

8. Click on **Replace all**, save and exit.

9. Go back to the **PDR-Flow-Solver** directory, double-click to open the file **README.md** and copy the command line **cmake -DCMAKE_BUILD_TYPE=Release**

10. Paste the copied command line **cmake -DCMAKE_BUILD_TYPE=Release** on the terminal opened in step 3, and hit **Enter**:

    Step 10 will fail if **cmake** is not installed. To install **cmake**, type the command **sudo apt-get -y install cmake** on terminal and hit **Enter** (Ubuntu and Mint distributions).

11. Type **make** in terminal and hit **Enter** to finally compile prePro:

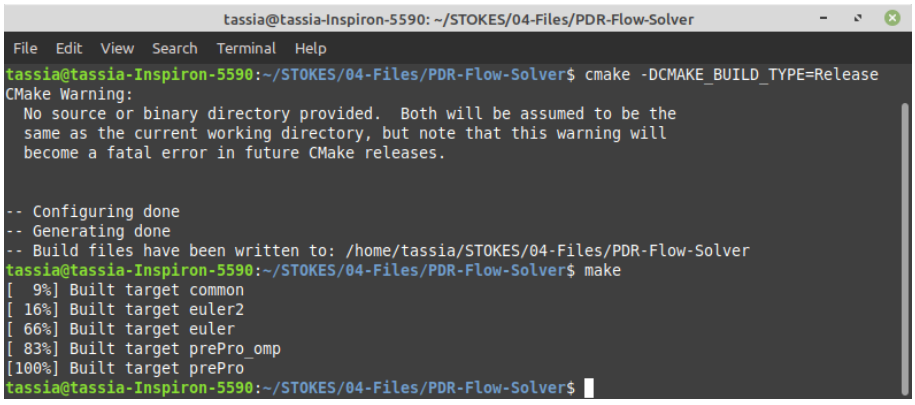

12. The program will be compiled and the executable **prePro** file saved in the directory **bin**:

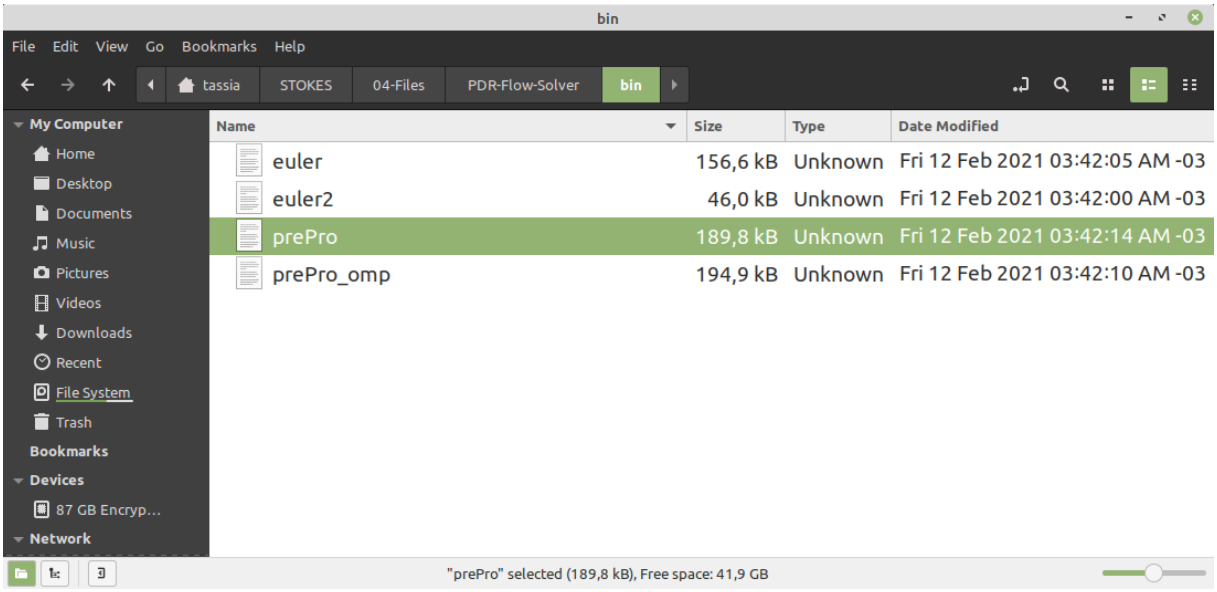

13. Copy the executable **prePro** to the directory **02-Porosity**

14. Copy the geometry CAD file **cube.stl** from **01-Geometry** to **02-Porosity**

15. Open the directory **02-Porosity** and open a new terminal:

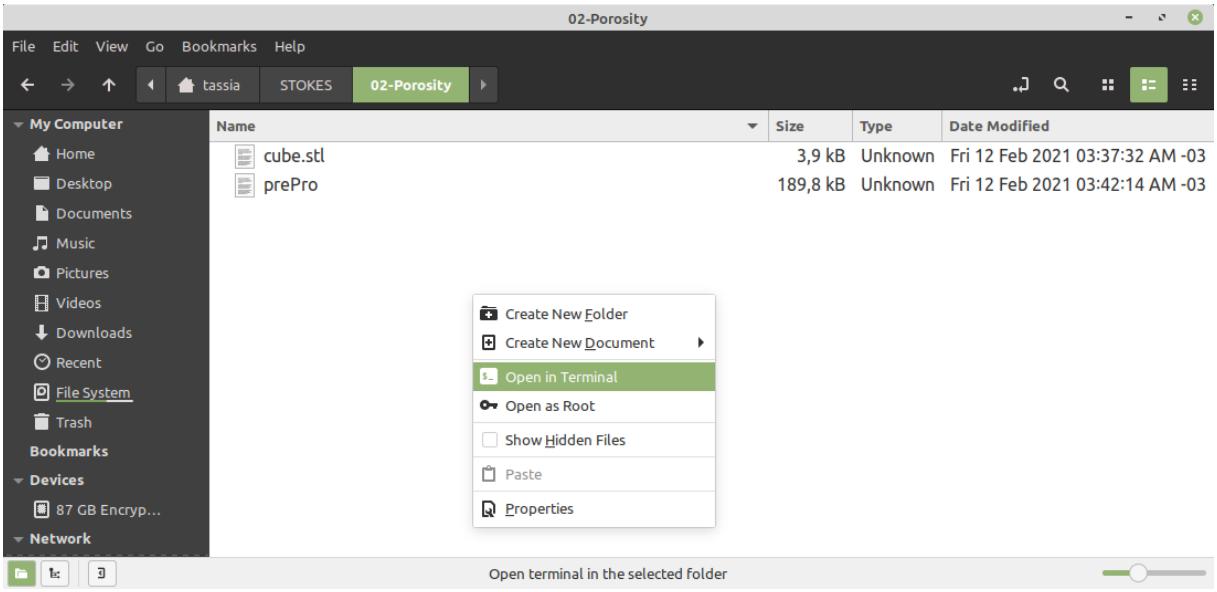

16. Type the command **./prePro cube.stl -manual** and hit **Enter** to run prePro in the manual mode:

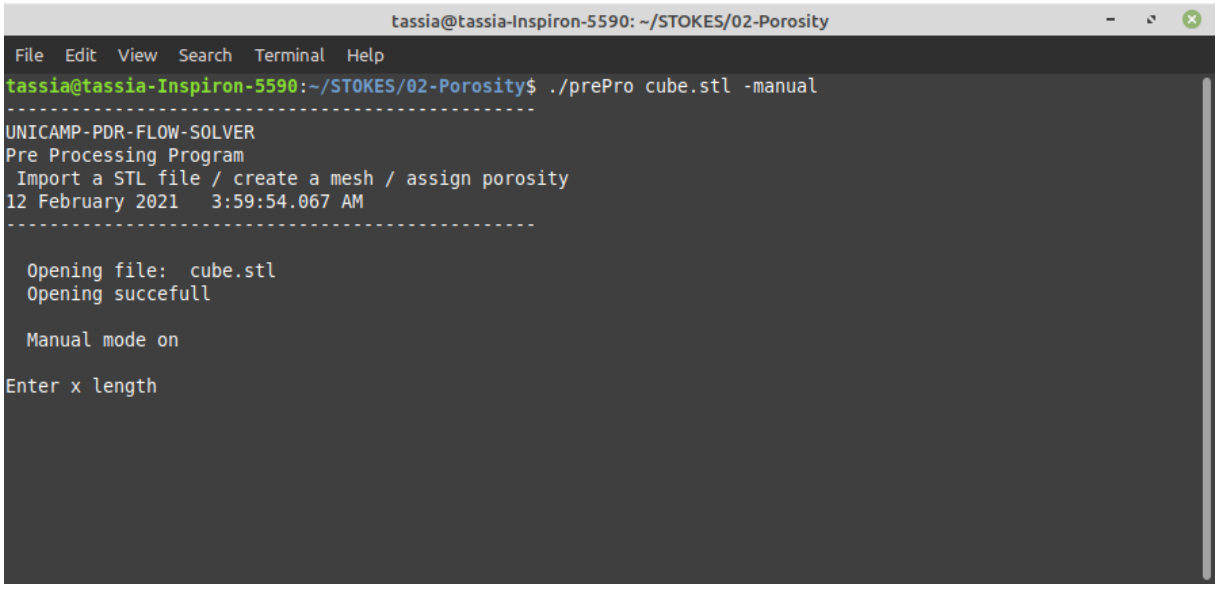

17. In this example, the domain dimensions are set to 0.250 x 0.050 x 0.050 m and the mesh spacing in all three directions is of 0.001 m. Axes translation are set to -0.1 m in the x direction, and -0.025 m in the y and z directions:

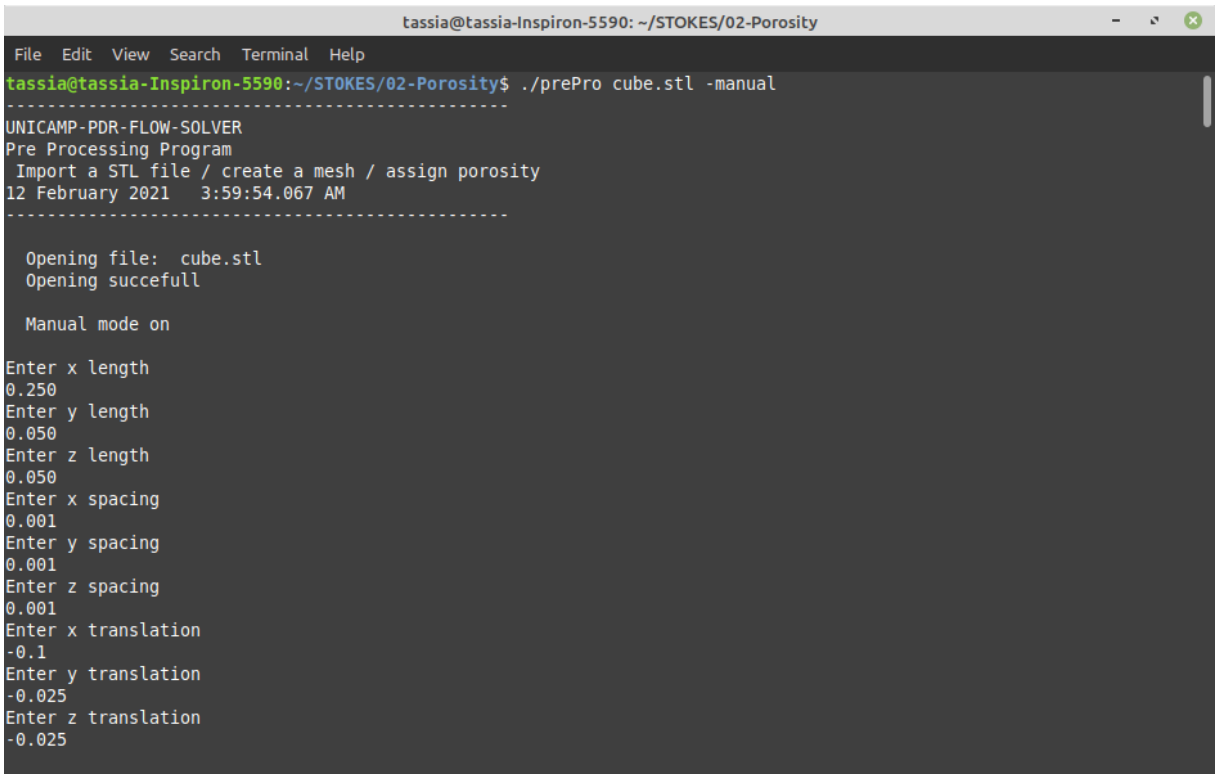

A porous mesh will be generated in the specified domain and several files will be created in the directory **02–Porosity**.

18. In **02-Porosity** directory, copy the geometry files

    cube.parameters.dat

    cube.porosity.areaX.asc

    cube.porosity.areaY.asc

    cube.porosity.areaZ.asc

    cube.porosity.asc

    to the directory **03-Simulation**:

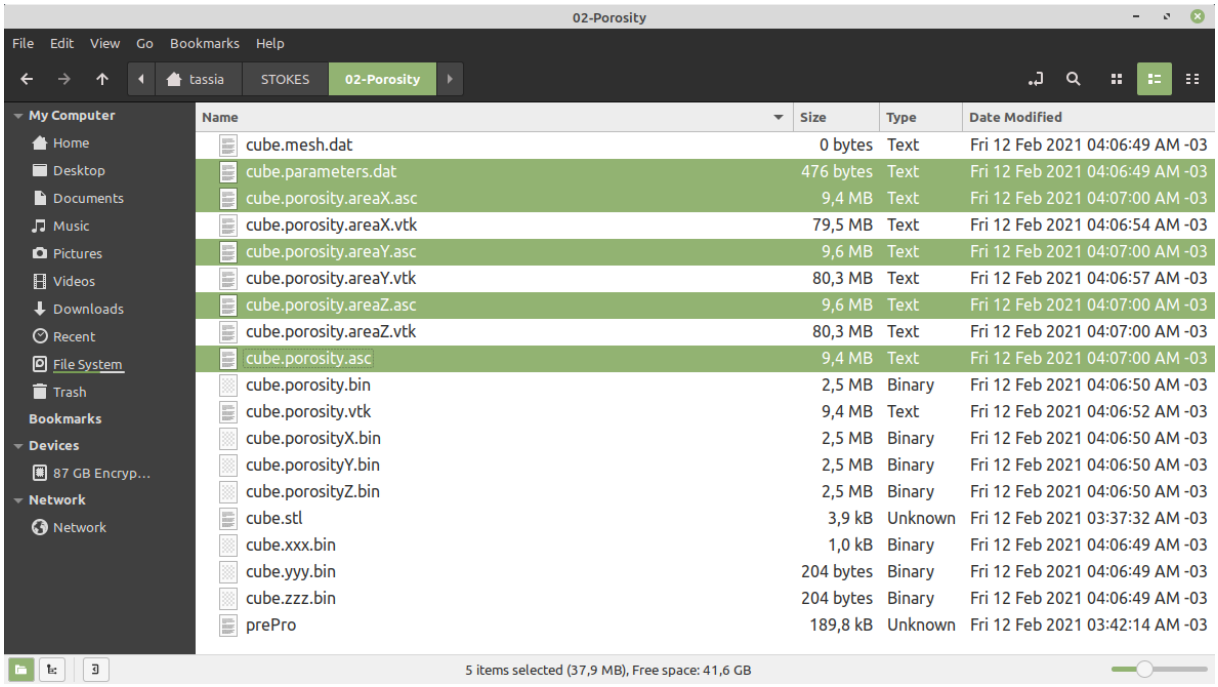

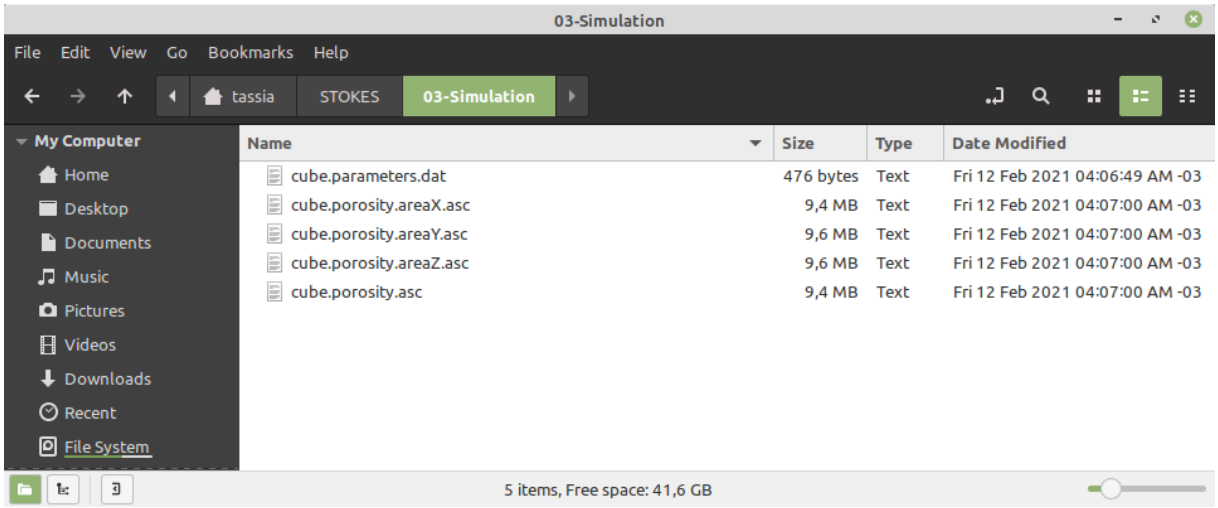

The geometry files are now ready to be used in a simulation case.

B.3 Running STOKES

STOKES is an open source CFD tool with no graphic interface. All subroutines which compose STOKES source code are located in the directory **solver_lam2_KA_DA_frac_fp_fs**.

It is **highly** recommended that the directory containing STOKES source code is added to the directory where the simulation will be run, along with the setup file and geometry files. This is essential not to get confused about which version of STOKES corresponds to the simulation case to be run.

The steps below will present the good practices to be followed when running a case in STOKES. Orientation on how to create a simple bash scripting file to make the simulation safer and easier is also presented.

1. Copy STOKES source code **solver_lam2_KA_DA_frac_fp_fs** from **04-Files** to **03-Simulation**

2. Copy the setup file **flow** from **04-Files** to **03-Simulation**

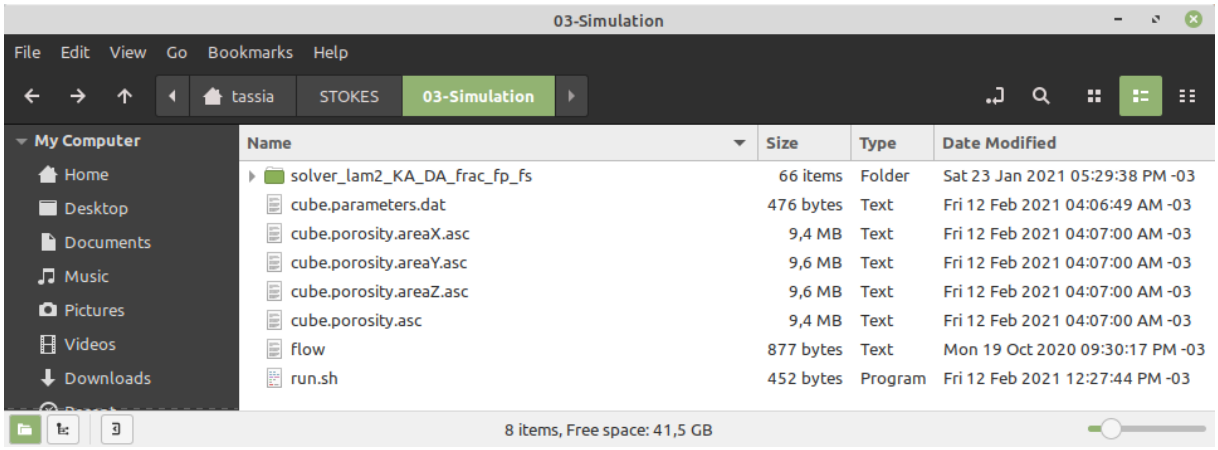

B.3.1 Bash script file *run.sh*

In this section you will lean how to create a script file named **run.sh** to run STOKES more easily. The script file is meant to deleted old simulation files, compile STOKES source code, copy the executable file to the simulation folder and open the setup file to start a new simulation.

It should be noted that the script file **run.sh** can be modified conveniently by the user at any time.

1. Open a terminal from the **03-Simulation** directory (right-click on any blank space and choose **Open in Terminal**)

2. To create a bash script file with **Vim** text editor, type on terminal **vim run.sh** and hit **Enter**

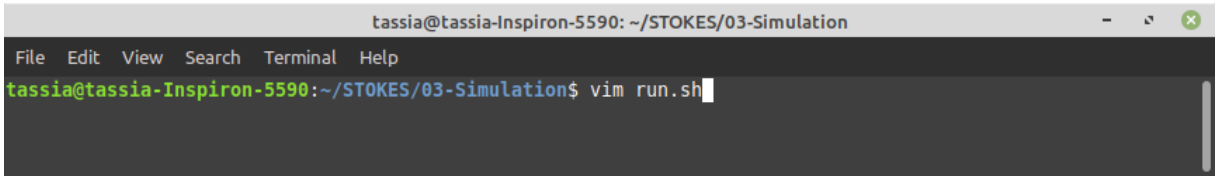

3. Type **i** to enter in **Insert mode** in **Vim**

4. In the insert mode, type the following lines:

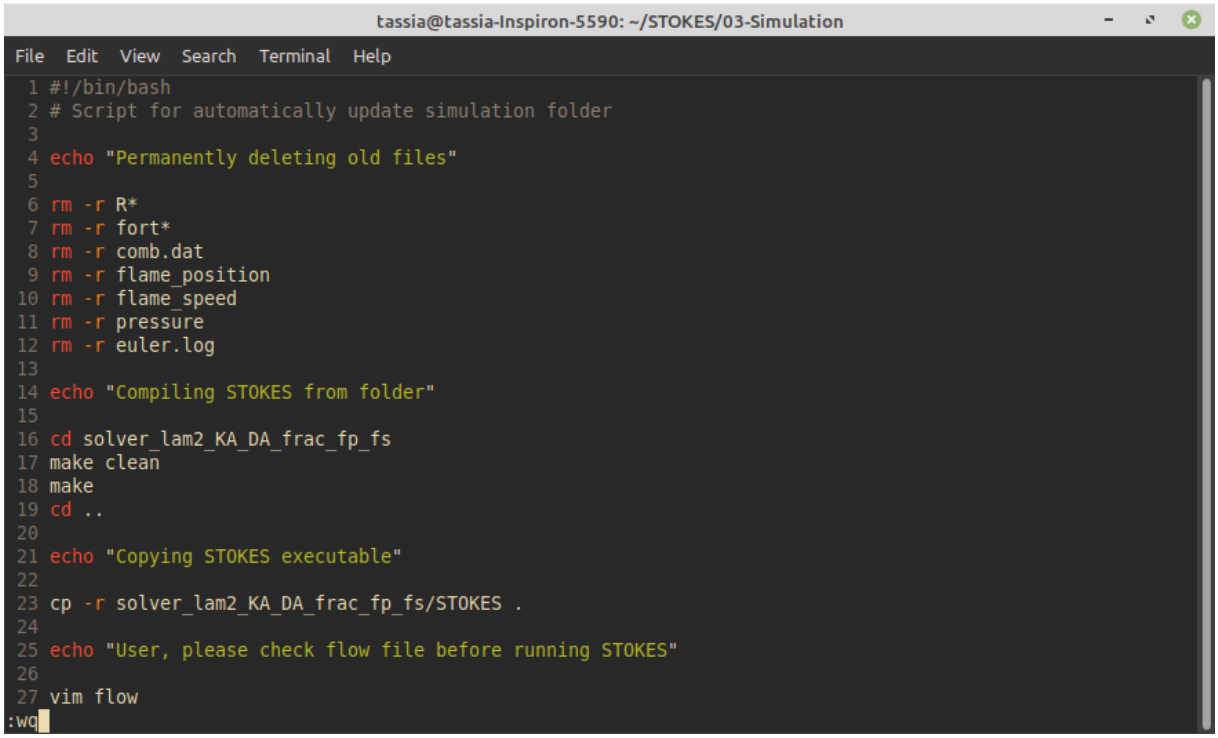

5. To exit insert mode, hit **Esc**

6. To save and exit the **run.sh** file, type **:wq** and hit **Enter** to go back to terminal

   The **run.sh** file was created in **03-Simulation** directory. It is possible to check it directly from terminal by typing **ll** and **Enter**. However, it is now necessary to make the **run.sh** file executable. This is done by changing the file permission with the command **chmod**.

7. To make the **run.sh** file executable, type in terminal **chmod 777 run.sh**, hit **Enter**, and then type **ll** to check the permission has changed (the file name will change colours):

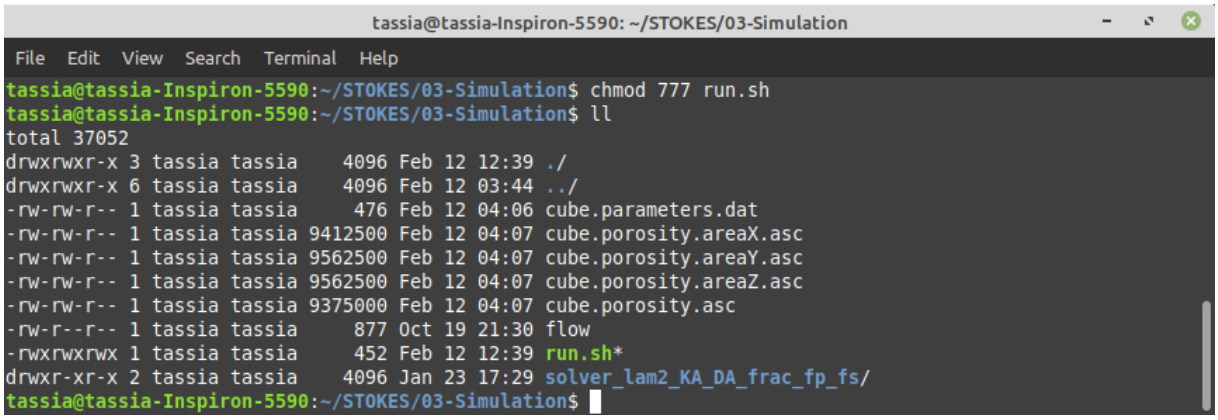

8. It is now possible to execute the **run.sh** file. To do that, type in terminal **./run.sh** and hit **Enter**

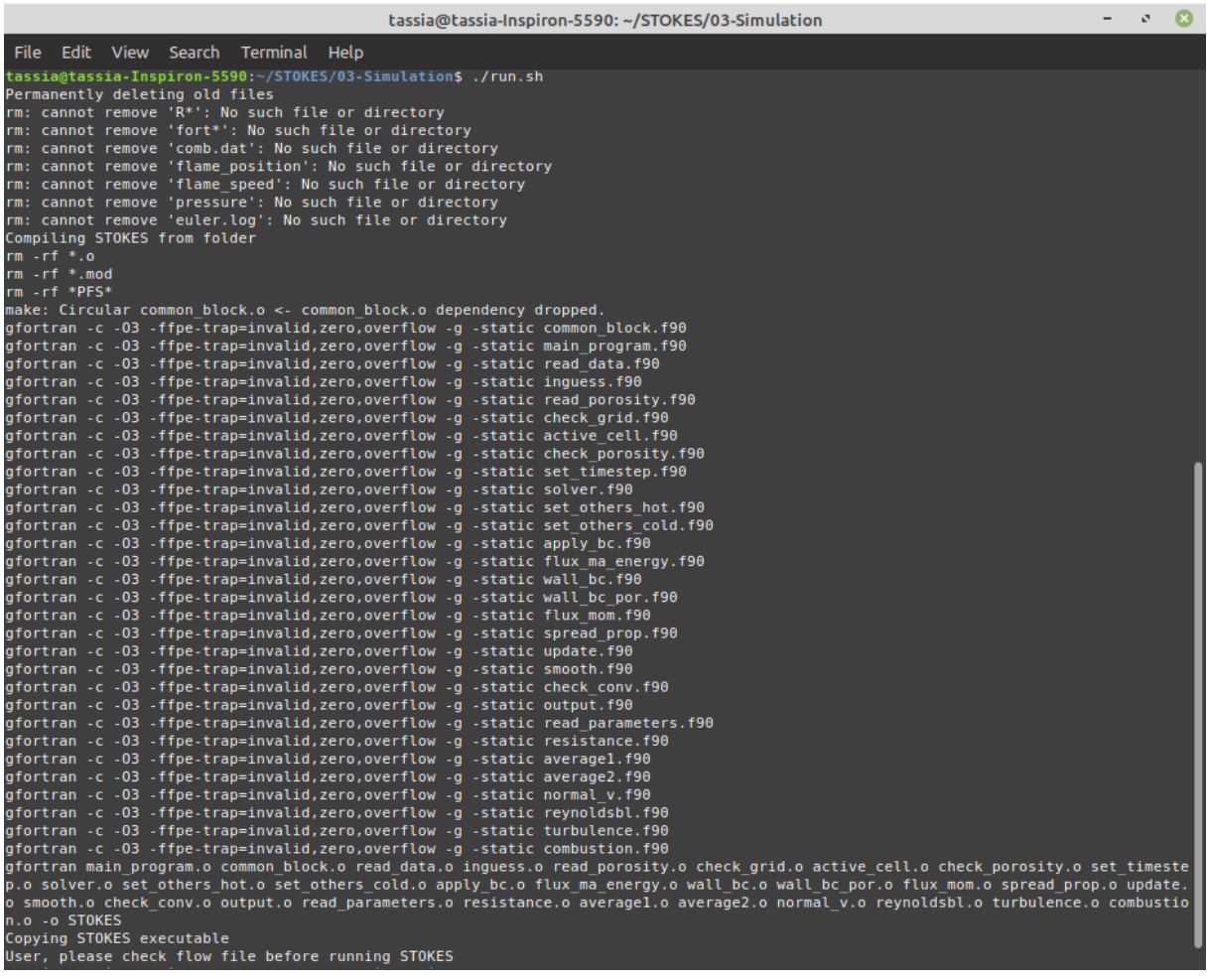

The **./run.sh** file will execute commands to delete old files, compile STOKES and bring the executable STOKES file to the simulation directory. The last command in **./run.sh** file is to open the setup **flow** file with **Vim**

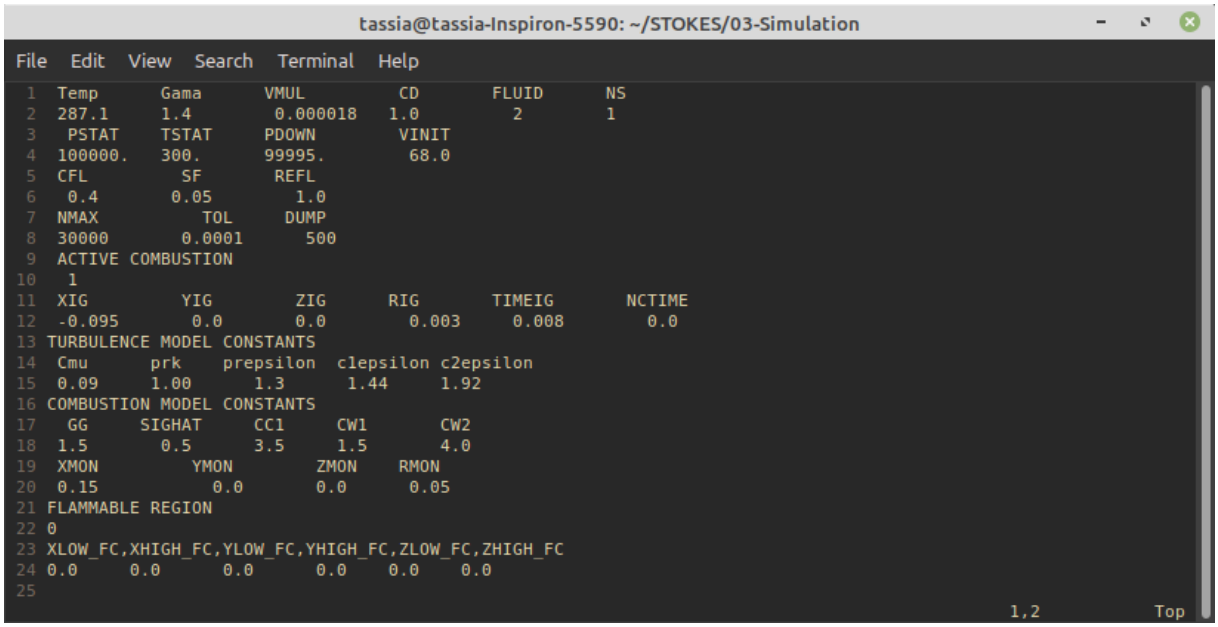

B.3.2 The setup file *flow*

The setup file **flow** contains many parameters that can be modified by the user according to the study of interest. Table B.1 shows the description of the **flow** file parameters.

Table B.1: Flow file parameters description

Ideal gas constant (air)	Heat capacities ratio (air)	Viscosity (air)	Dragging coefficient	Fluid type: 1-methane 2-propane	Navier Stokes flow code
Temp	**Gama**	**VMUL**	**CD**	**FLUID**	**NS**
287.1	**1.4**	**0.000018**	**1**	**2**	**1**
Stagnation pressure	Stagnation temperature	Pressure downwind	Initial velocity (ventilation)		
PSTAT	**TSTAT**	**PDOWN**	**VINIT**		
100000	**300**	**99995**	**68**		
Courant–Friedrichs–Lewy (CFL) condition	Smooth Factor				
CFL	**SF**	**REFL**			
0.4	**0.05**	**1**			
Iterations maximum number	Error tolerance	Write vtk file			
NMAX	**TOL**	**DUMP**			
30000	**0.0001**	**500**			
ACTIVE	COMBUSTION				
1					
Ignition point (x)	Ignition point (y)	Ignition point (z)	Ignition radius	Ignition time	
XIG	**YIG**	**ZIG**	**RIG**	**TIMEIG**	**NCTIME**
-0.095	**0**	**0**	**0.003**	**0.008**	**0**

TURBULENCE	MODEL	CONSTANTS			
Cmu	**prk**	**prepsilon**	**c1epsilon**	**c2epsilon**	
0.09	**1**	**1.3**	**1.44**	**1.92**	
COMBUSTION	MODEL	CONSTANTS			
GG	**SIGHAT**	**CC1**	**CW1**	**CW2**	
1.5	**0.5**	**3.5**	**1.5**	**4**	
Monitoring points					
XMON	**YMON**	**ZMON**	**RMON**		
0.15	**0**	**0**	**0.05**		
FLAMMABLE	REGION				
0					
Initial point of flammable cloud (x)	Final point of flammable cloud (x)	Initial point of flammable cloud (y)	Final point of flammable cloud (y)	Initial point of flammable cloud (z)	Final point of flammable cloud (z)
XLOW_FC	**XHIGH_FC**	**YLOW_FC**	**YHIGH_FC**	**ZLOW_FC**	**ZHIGH_FC**
0	**0**	**0**	**0**	**0**	**0**

B.3.3 Execution

Now that the **run.sh** has been created and the **flow** file has been introduced, STOKES can be finally run.

1. Before running STOKES, check if the directory **03-Simulation** contains all the geometry files, the **flow** file, and the **run.sh** file:

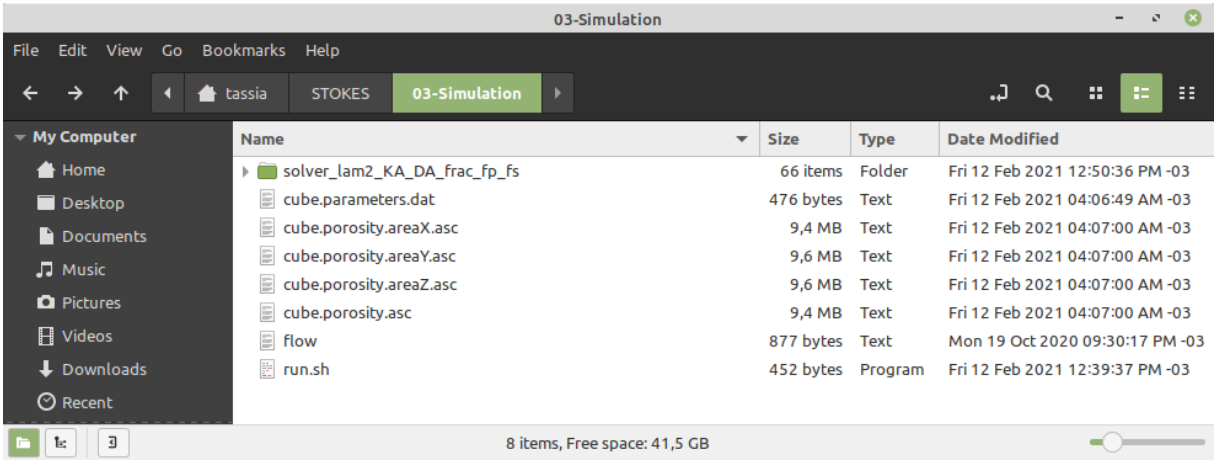

2. Right-click in any blank space to open a new terminal

3. In terminal, execute the **run.sh** file by typing **./run.sh** and hitting **Enter**. This will delete old files, create an updated executable STOKES file, and open the **flow** file in **Vim**.

4. To make modifications in the flow file, type **i** to enter **Insert mode**

5. As an example, modify the value of **CC1** to 3.4 (CC1 is the c_L constant of the BML model):

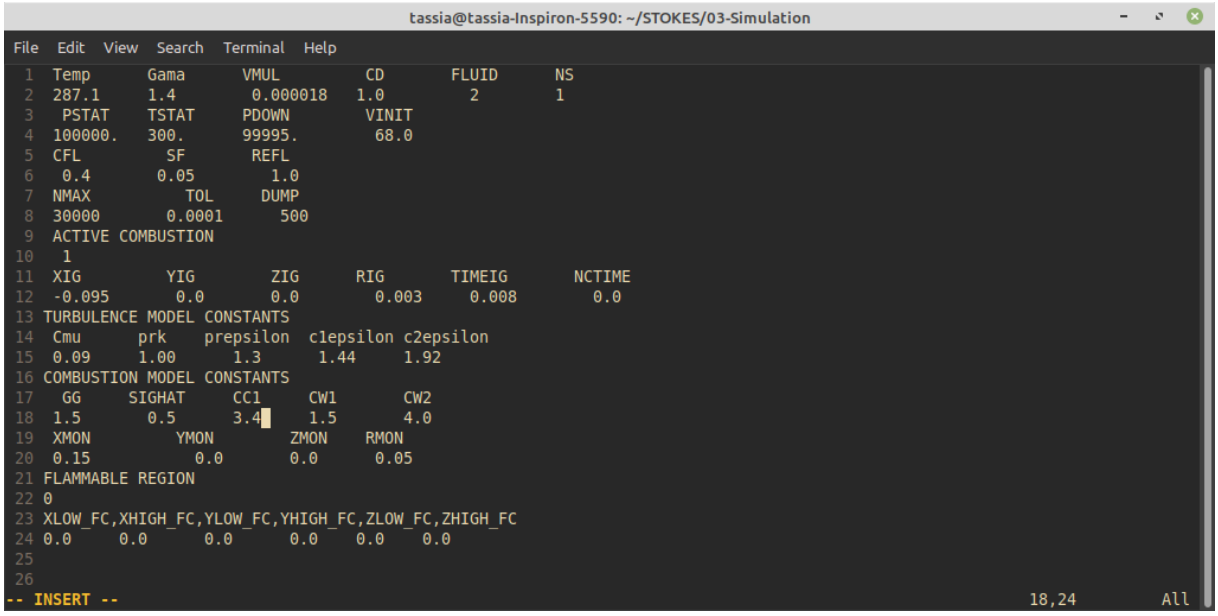

6. Exit insert mode by hitting **Esc**

7. Type **:wq** to save changes and exit the **flow** file. This action will close **Vim** and return to terminal

8. In the terminal, type **ll** and hit **Enter** to check all the existing files in **03-Simulation** directory:

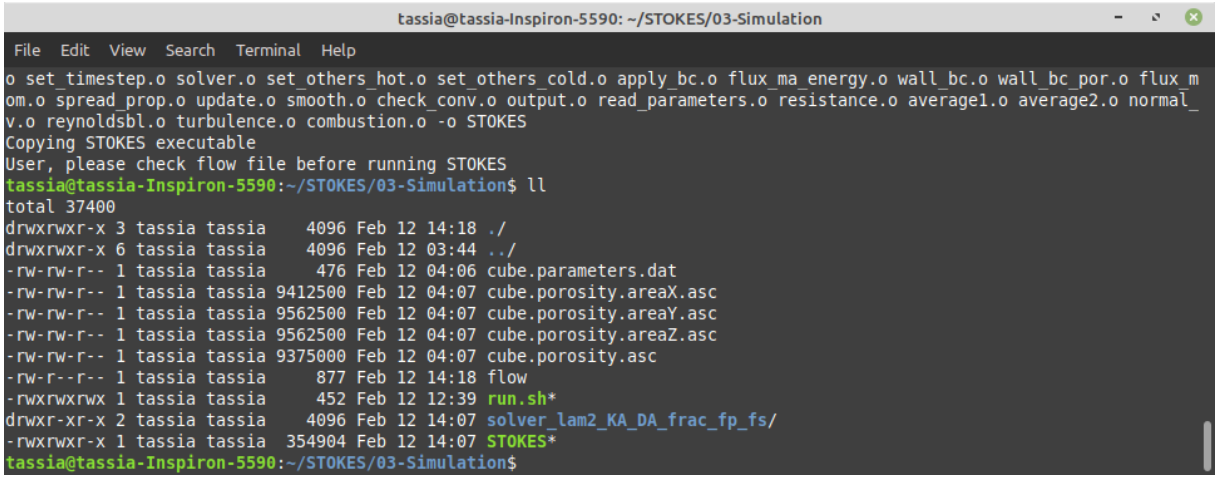

9. Execute STOKES by typing **./STOKES** and hitting **Enter**

   The patches will define if the domain boundaries are open or closed, this information need to be inserted by the user. In this example, all boundaries are defined as solid surfaces with the exception of the upper end of the chamber, which remains open:

```
X LOW   - solid surface

X HIGH  - outflow

Y LOW   - solid surface

Y HIGH  - solid surface

Z LOW   - solid surface

Z HIGH  - solid surface
```

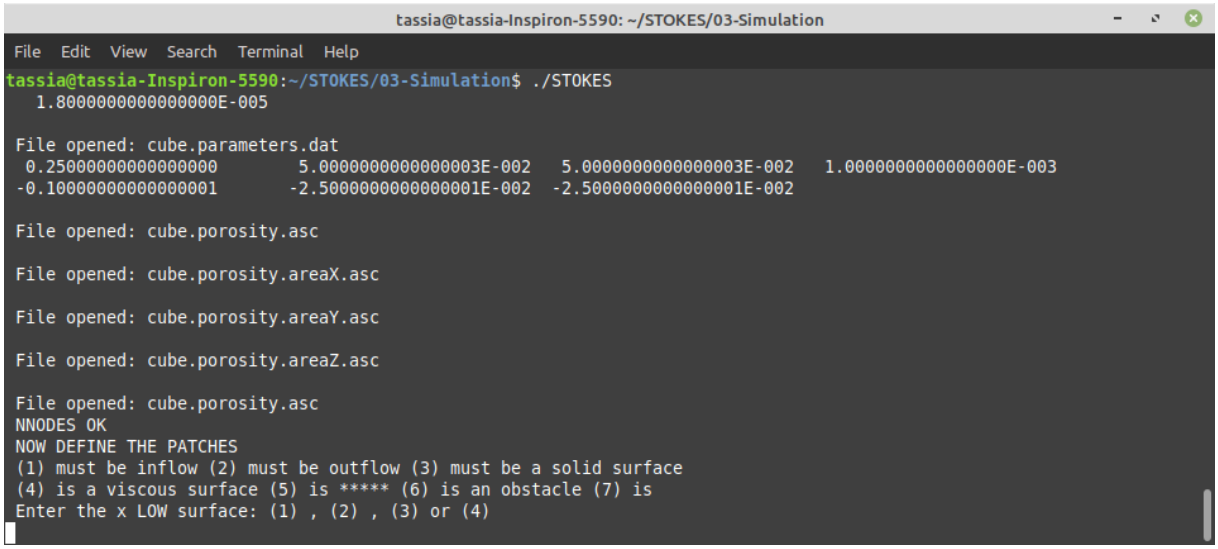

10. Follow the instructions shown on terminal and insert: **3** , **2** , **3** , **3** , **3**, **3**. Remember to hit **Enter** after each input number. The iteration will then start:

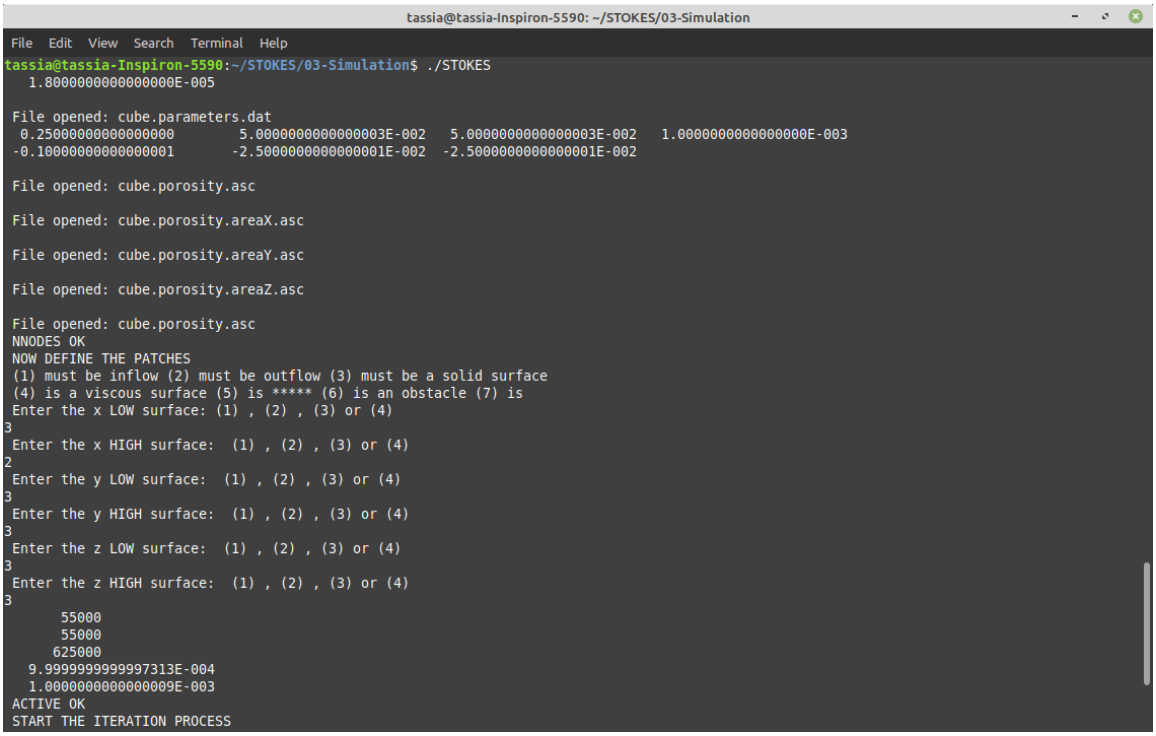

B.4 Post-processing

The instructions for the post-processing will be divided in two parts. In the first part, instructions on how to install and handle **ParaView** are presented. In the second part, it will be shown how to generate plots with **gnuplot** and script files.

B.4.1 ParaView installation

ParaView is an open-source, multi-platform data analysis and visualization application. It can be easily downloaded directly from the command terminal by following the steps below:

1. In any command terminal, type **sudo apt-get install paraview** and hit **Enter**
2. Insert the system password and hit **Enter**

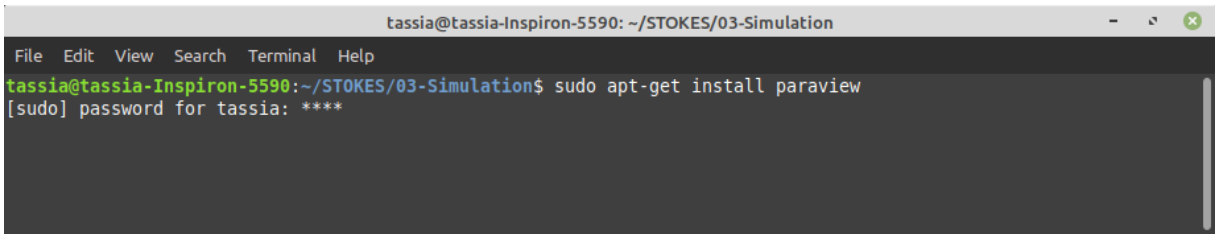

3. Type **yes** to any question during installation. ParaView will be installed.
4. After the installation is finished, type **paraview & exit** and hit **Enter** to open ParaView and close the terminal.

B.4.2 Opening a .vtk file with ParaView

When the simulation is finished, several output files will be created throughout the simulation and saved in the **03-Simulation** directory. The output files with a **.vtk** extension must be open in ParaView.

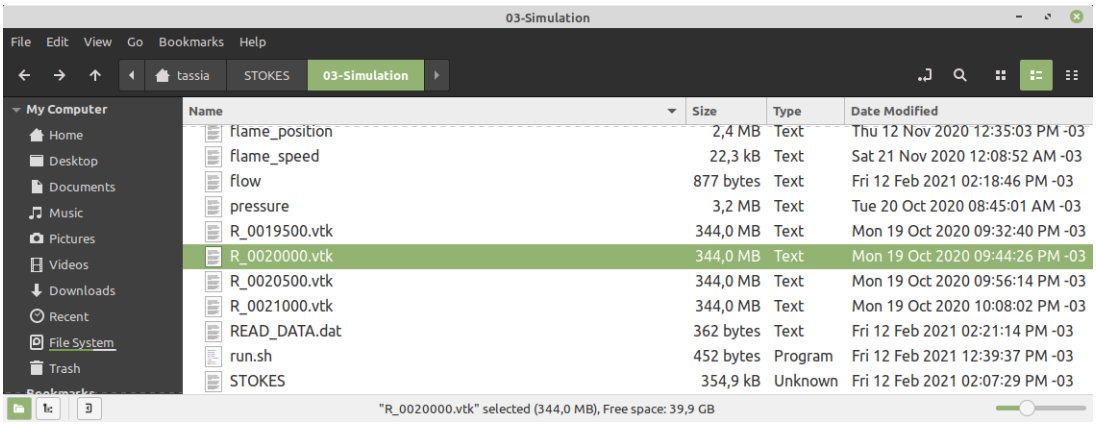

1. From the **03-Simulation** directory, right-click in any blank space to open a new terminal

2. In the new terminal, type **paraview & exit** and **Enter** to open ParaView and exit terminal.

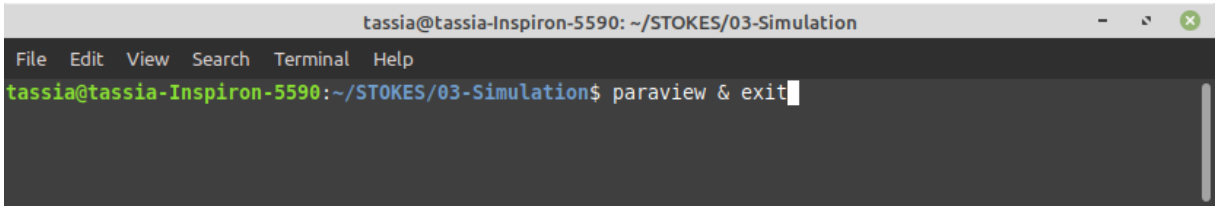

3. In ParaView, click on the yellow folder located at the top left corner to open the **03-Simulation** directory

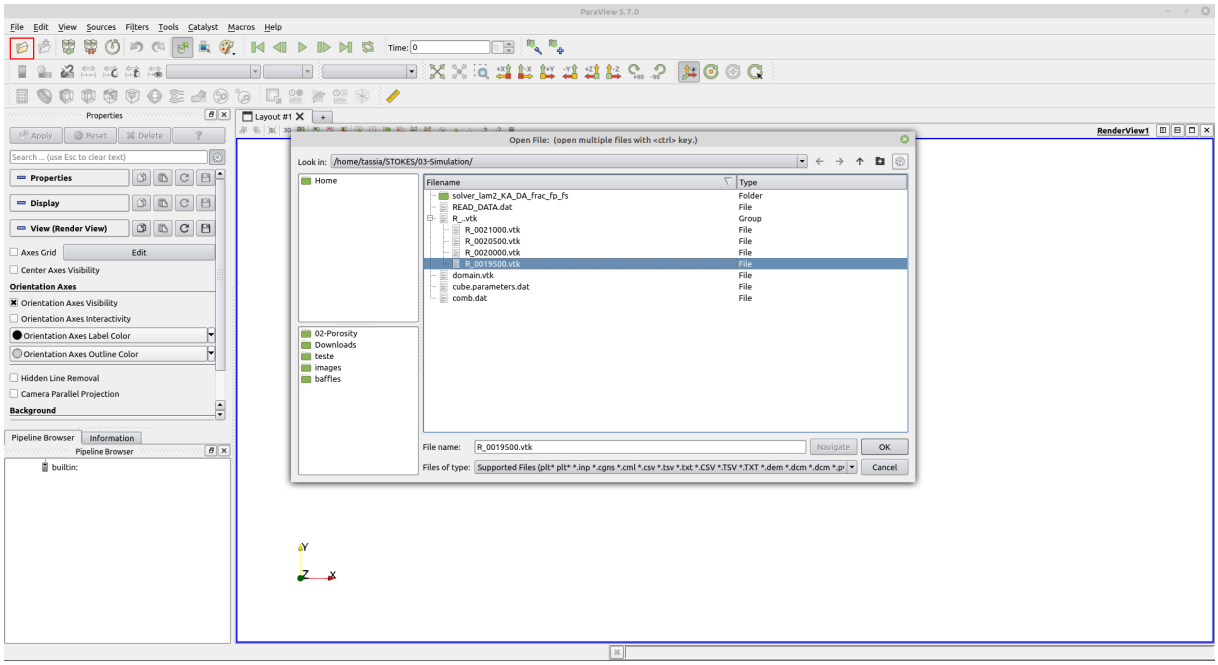

4. Double-click on the desired **.vtk** file and wait for ParaView to read it

5. Select the icon on the top ribbon to **"Apply changes to parameters automatically"**:

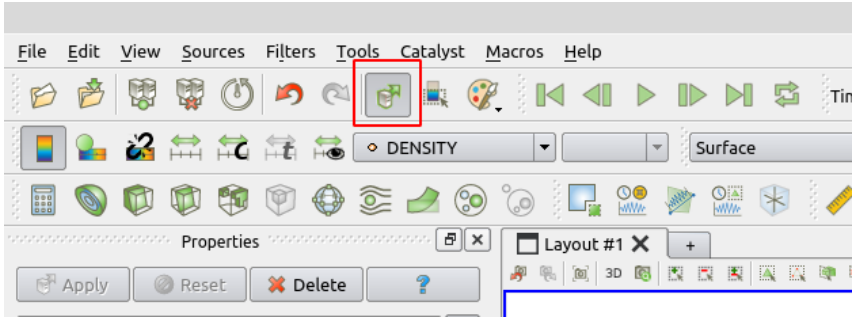

6. Make a slice selecting the **Slice** icon on top and then click on **Z Normal** in the **Plane Parameters** panel:

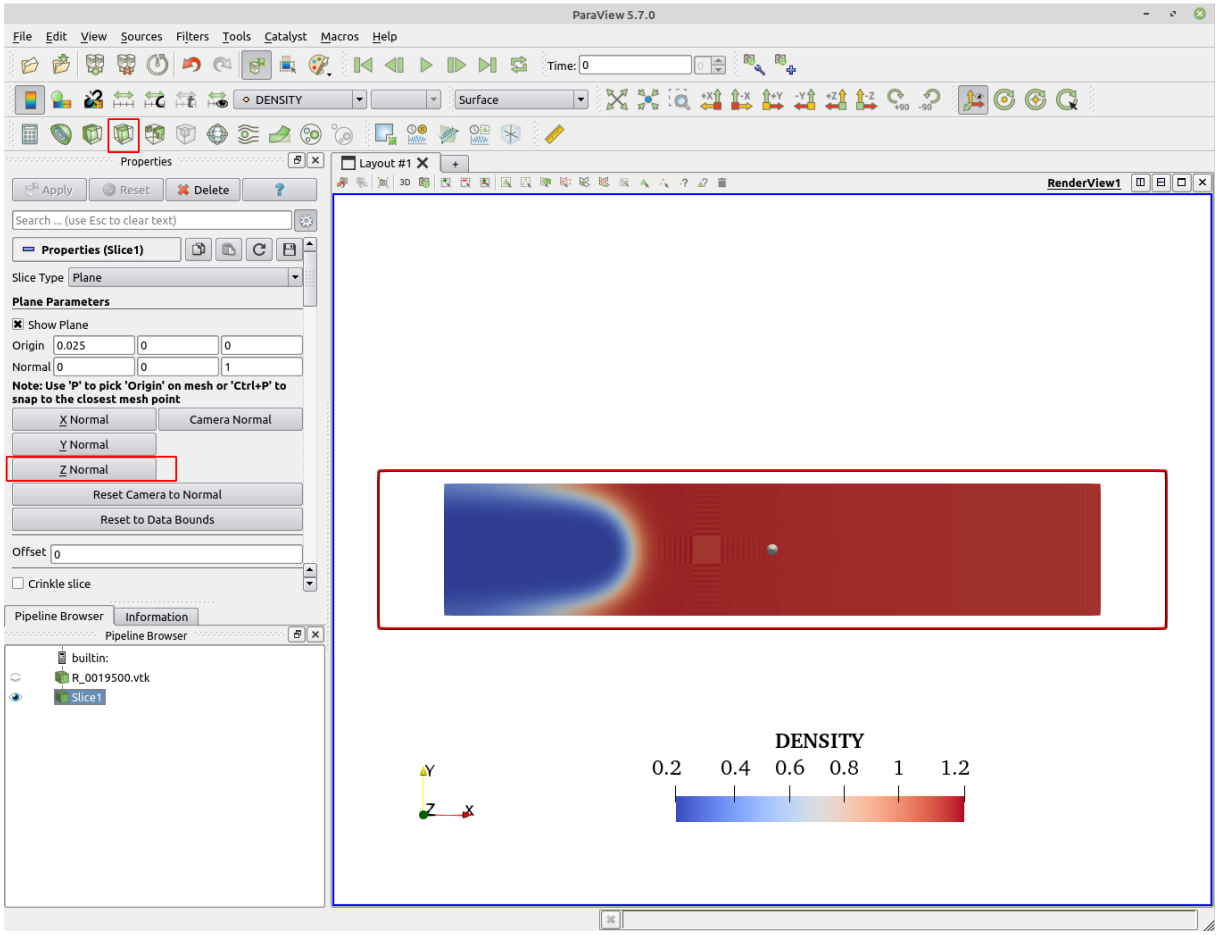

7. It is possible to change parameters from **Density** to for example **PV** (reaction progress variable) in top ribbon:

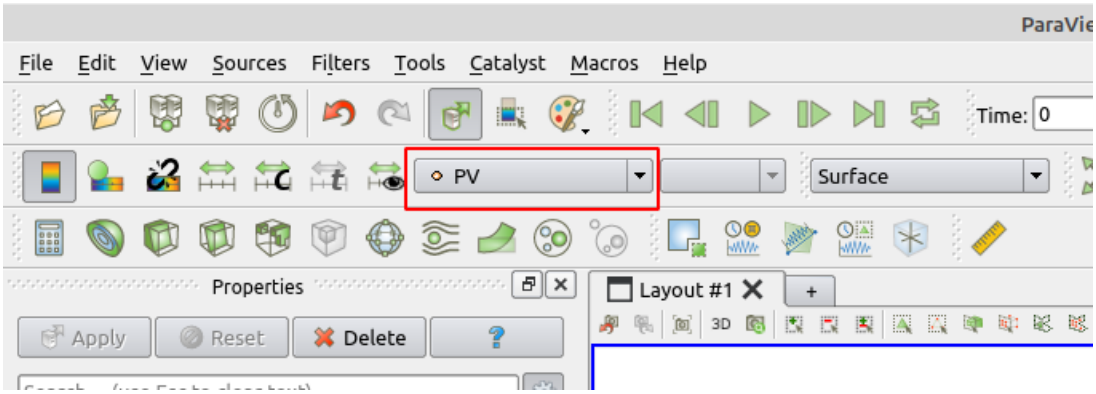

8. To change colours, click on the **Edit color map** icon in the top ribbon to open the **Color Map Editor**

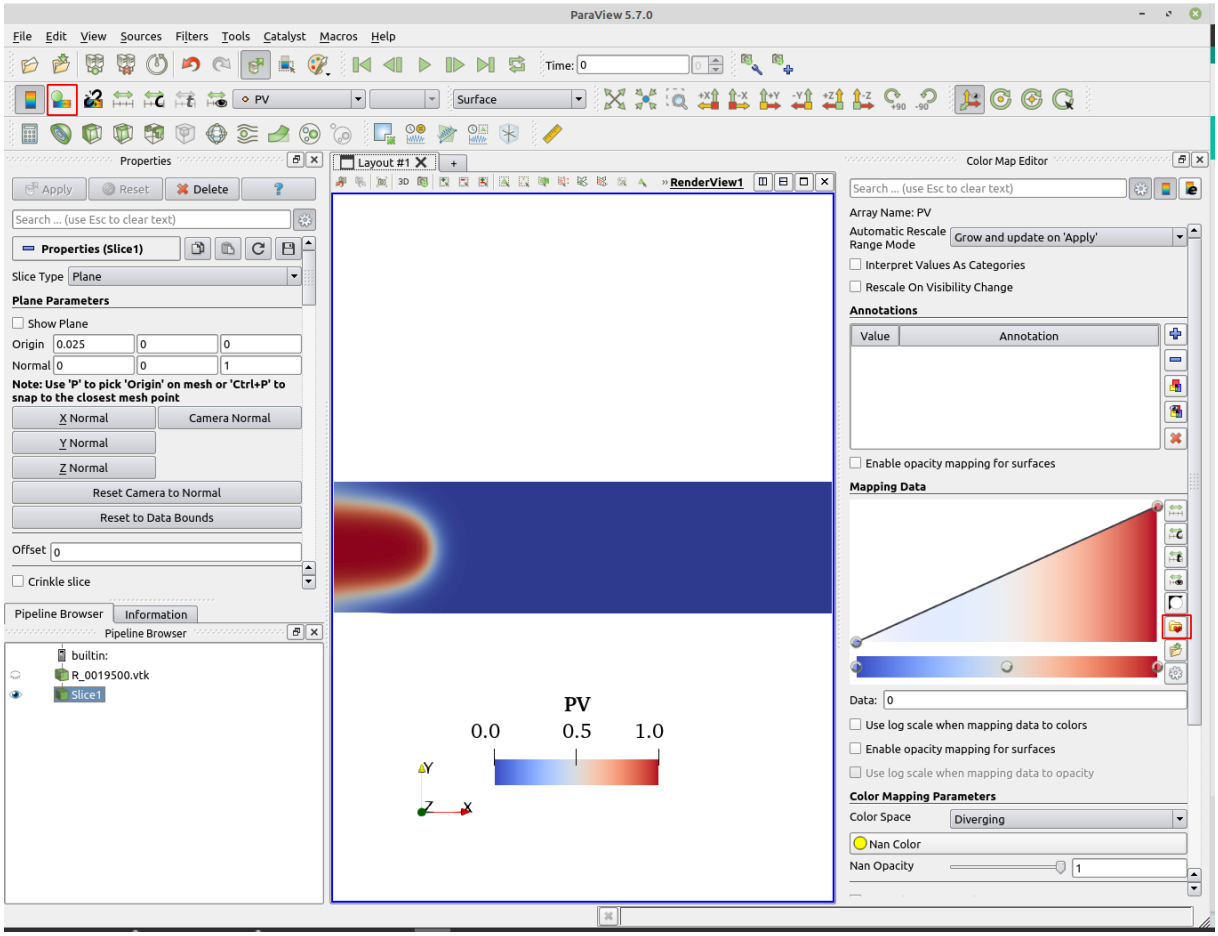

9. Click on the yellow folder icon with a heart on it to open the **Color Preset** window

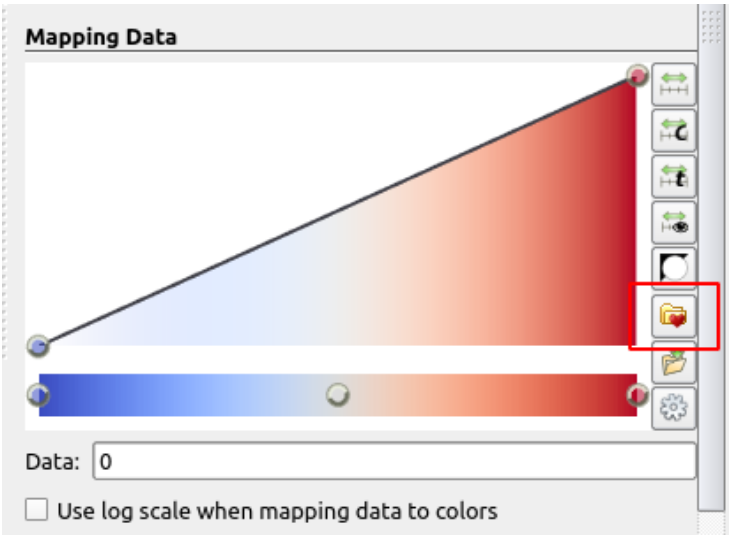

10. Choose the desired colour preset, e.g. **jet** and hit **Apply** and then **Close**

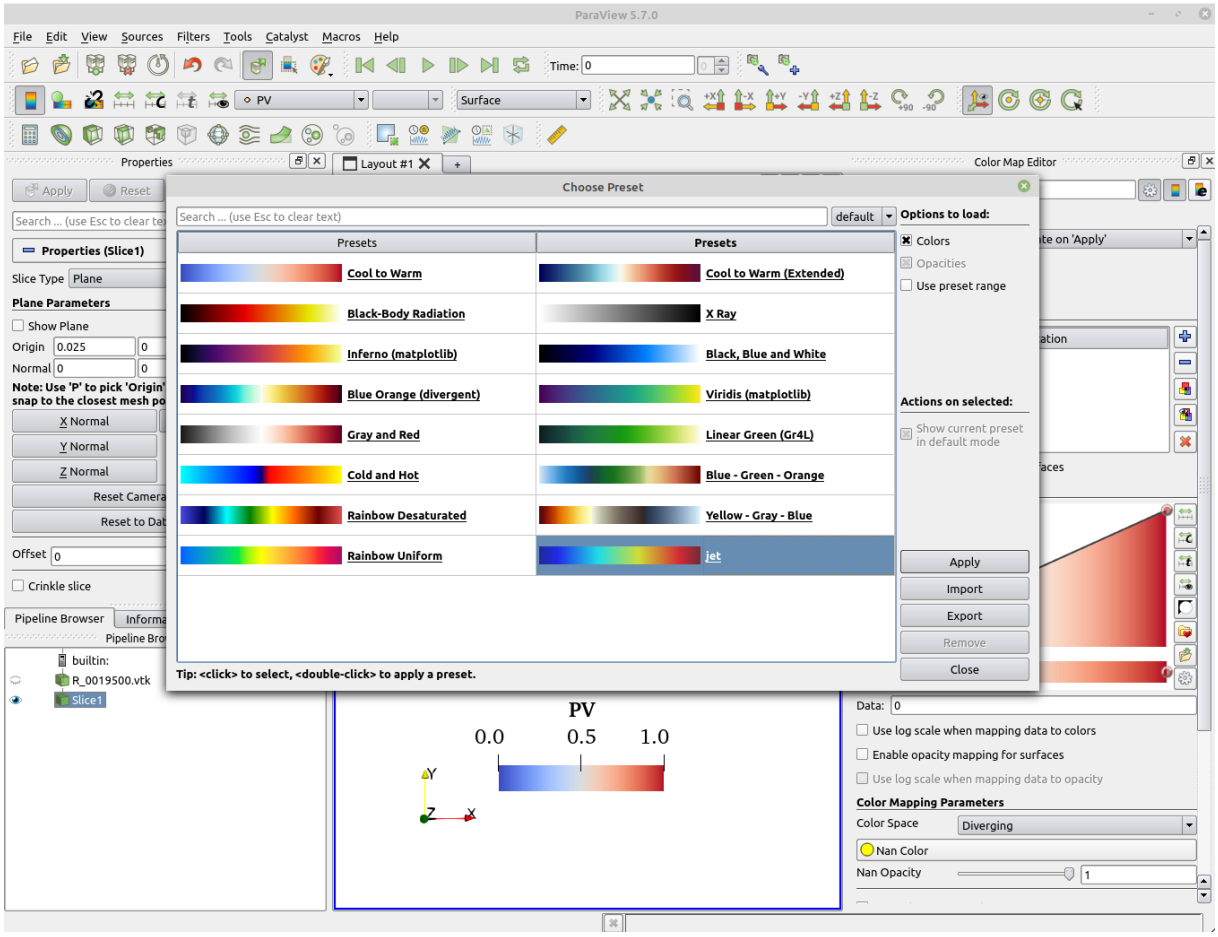

11. To export the image to a desired directory with a **.png** extension, click on **File** > **Save Screenshot**

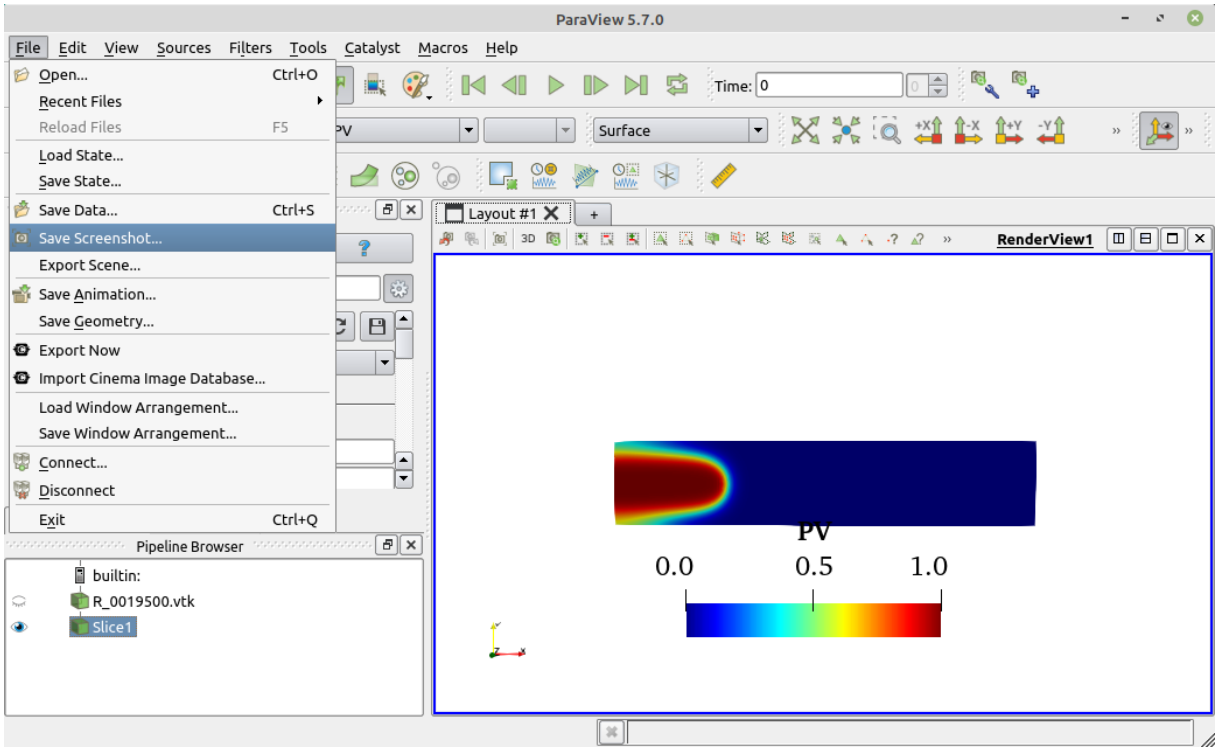

12. In the **Save screenshot** window, create a new folder named **Images**

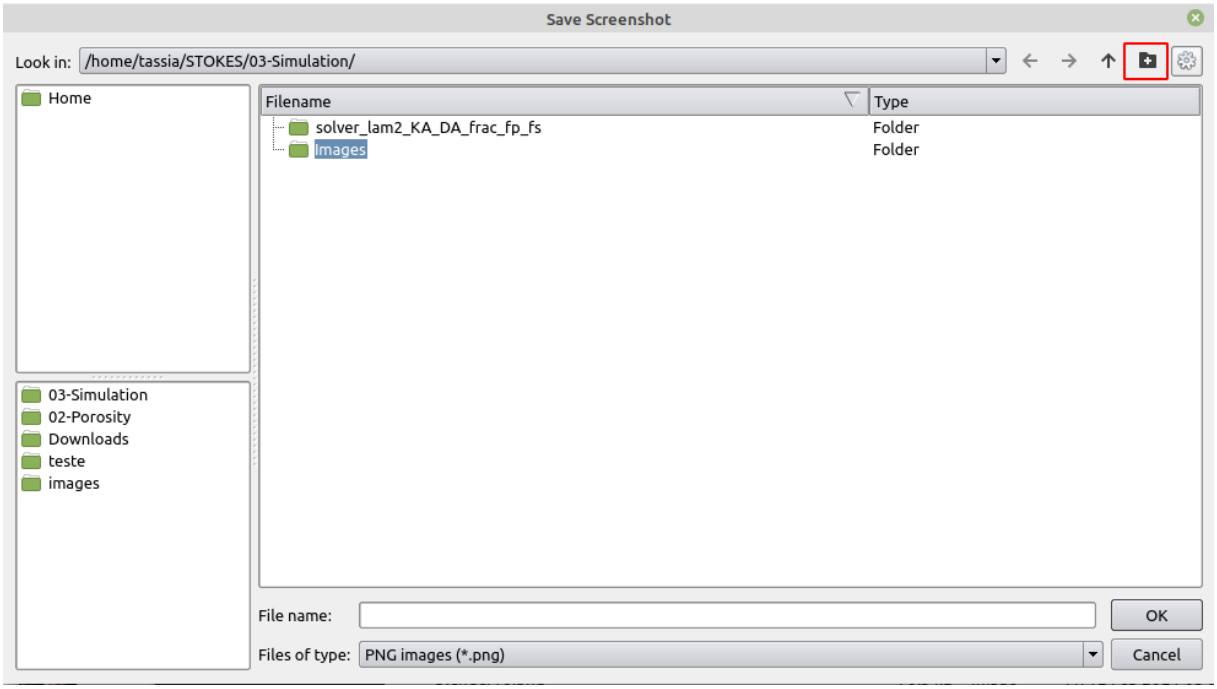

13. Double-click on **Images** to open it

14. Name your picture and then click on **OK**. A new window will open, you can click on **OK** again.

15. The image will be saved in the **Images** directory, within the simulation folder.

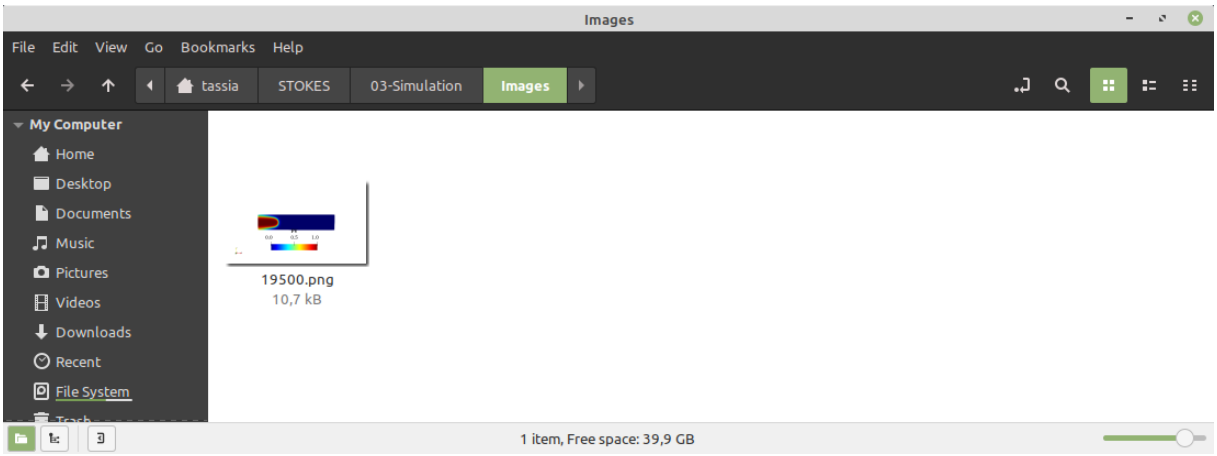

B.4.3 Graphs with gnuplot

The output files **flame_position**, **flame_speed**, and **pressure** generated throughout the simulation will be read by **gnuplot**. Gnuplot is a portable command-line driven graphing utility for GNU/Linux. Therefore, it does not have a graphic interface and needs to be run in terminal. However, it is convenient to create gnuplot script files to make plotting easier and more straightforward.

This section provides instructions on how to install gnuplot directly from terminal as well as on how to run gnuplot with the help of script files.

Installation

1. To install gnuplot directly from the command terminal, type **sudo apt-get install -y gnuplot** and hit **Enter**

2. Insert the system password and hit **Enter**. Gnuplot will be installed.

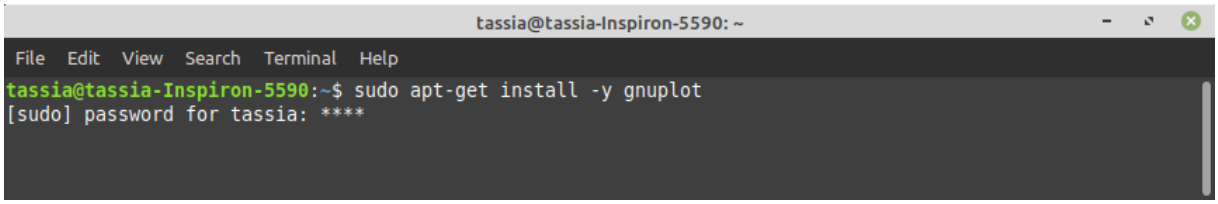

3. It is possible to open gnuplot from terminal by typing **gnuplot** and hitting **Enter**

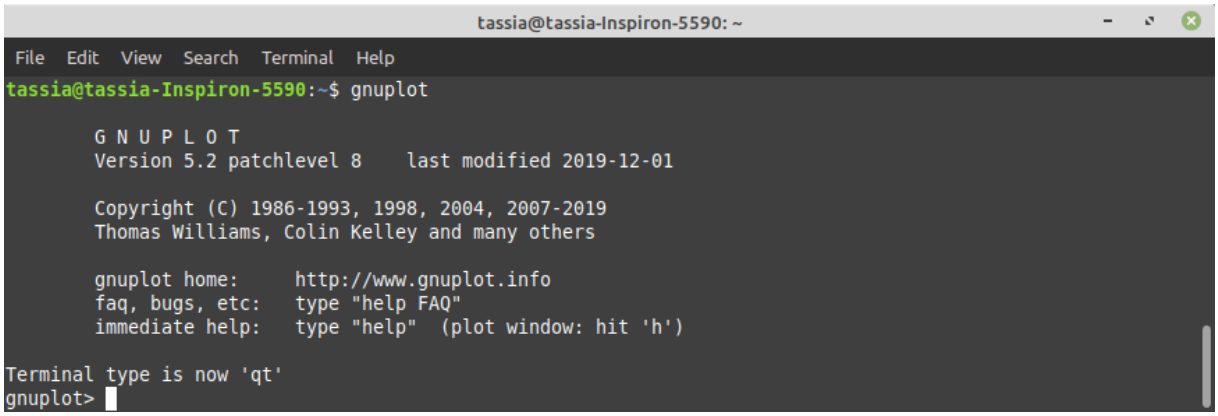

However, this is not the most efficient way to use the tool. Instead, we are going to write all the commands to be inserted in gnuplot in a script file that gnuplot is able to read. The script file will allow the graphs of flame position, flame speed and overpressure time histories to be generated all at once.

Gnuplot script

1. From the **03-Simulation** directory where the output files are located, right-click on any blank space to open a new terminal

2. In terminal, type **vim graphs.p** and hit **Enter**

3. Type **i** to enter **Insert mode** and copy the information below to your script file:

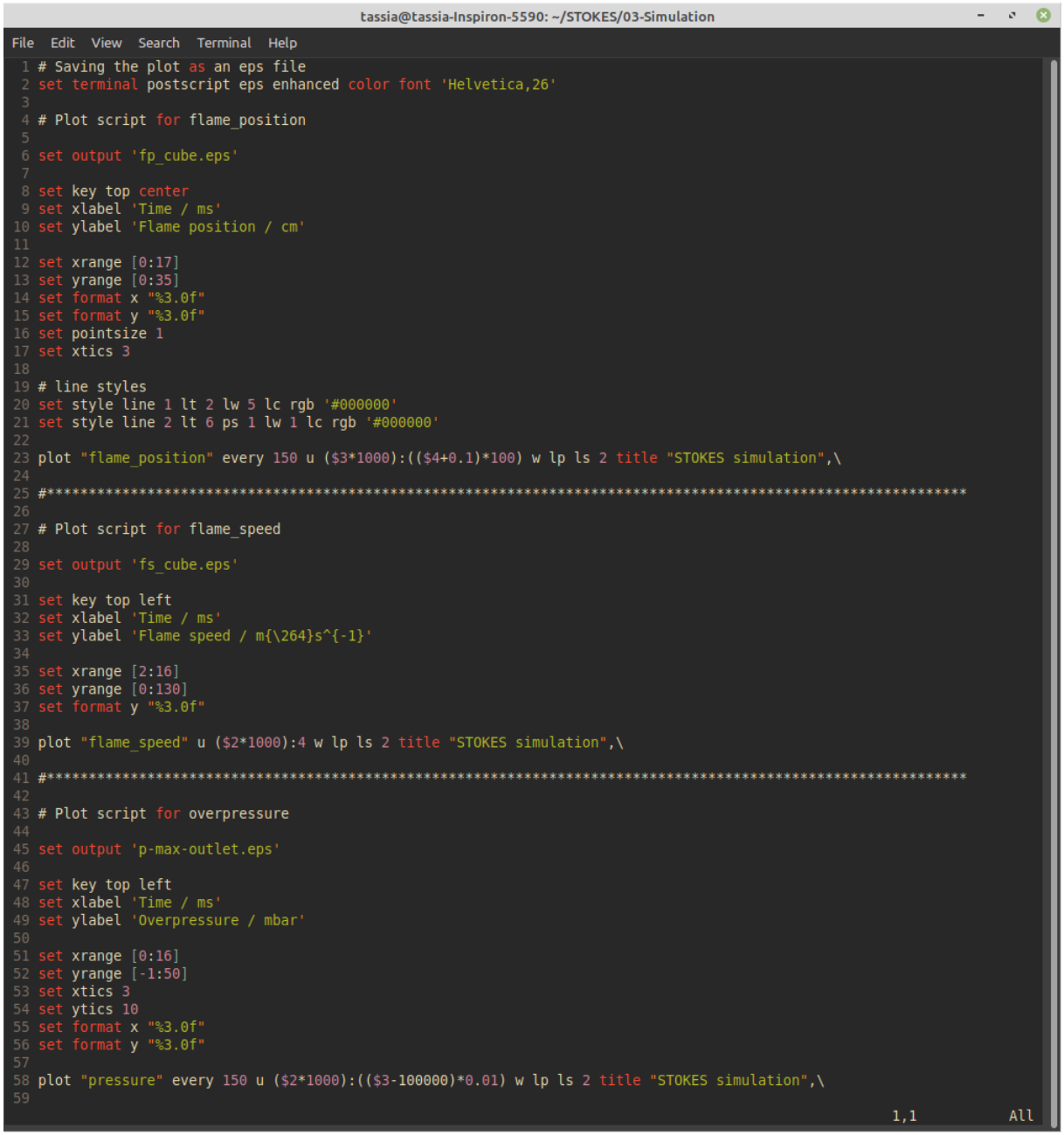


```
# Saving the plot as an eps file
set terminal postscript eps enhanced color font 'Helvetica,26'

# Plot script for flame_position

set output 'fp_cube.eps'

set key top center
set xlabel 'Time / ms'
set ylabel 'Flame position / cm'

set xrange [0:17]
set yrange [0:35]
set format x "%3.0f"
set format y "%3.0f"
set pointsize 1
set xtics 3

# line styles
set style line 1 lt 2 lw 5 lc rgb '#000000'
set style line 2 lt 6 ps 1 lw 1 lc rgb '#000000'

plot "flame_position" every 150 u ($3*1000):(($4+0.1)*100) w lp ls 2 title "STOKES simulation",\

#*****************************************************************************************************************

# Plot script for flame_speed

set output 'fs_cube.eps'

set key top left
set xlabel 'Time / ms'
set ylabel 'Flame speed / m{\264}s^{-1}'

set xrange [2:16]
set yrange [0:130]
set format y "%3.0f"

plot "flame_speed" u ($2*1000):4 w lp ls 2 title "STOKES simulation",\

#*****************************************************************************************************************

# Plot script for overpressure

set output 'p-max-outlet.eps'

set key top left
set xlabel 'Time / ms'
set ylabel 'Overpressure / mbar'

set xrange [0:16]
set yrange [-1:50]
set xtics 3
set ytics 10
set format x "%3.0f"
set format y "%3.0f"

plot "pressure" every 150 u ($2*1000):(($3-100000)*0.01) w lp ls 2 title "STOKES simulation",\

```

4. Type **Esc** to exit insert mode, and then type **:wq** to save changes and exit.

The gnuplot script file **graphs.p** was created. It contains information on what column to read in the output files, axes length, line styles, titles of axes, etc. Details on

the commands and sintaxe of gnuplot will not be explained here. For more information the user should refer to the gnuplot documentation, available online.

5. To generate the graphs, type on the terminal **gnuplot graphs.p** and hit **Enter**

6. Type **ll** and hit **Enter** to check that three files with **.eps** extension were created:

   `fp_cube.eps`

   `fs_cube.eps`

   `p-max-outlet.eps`

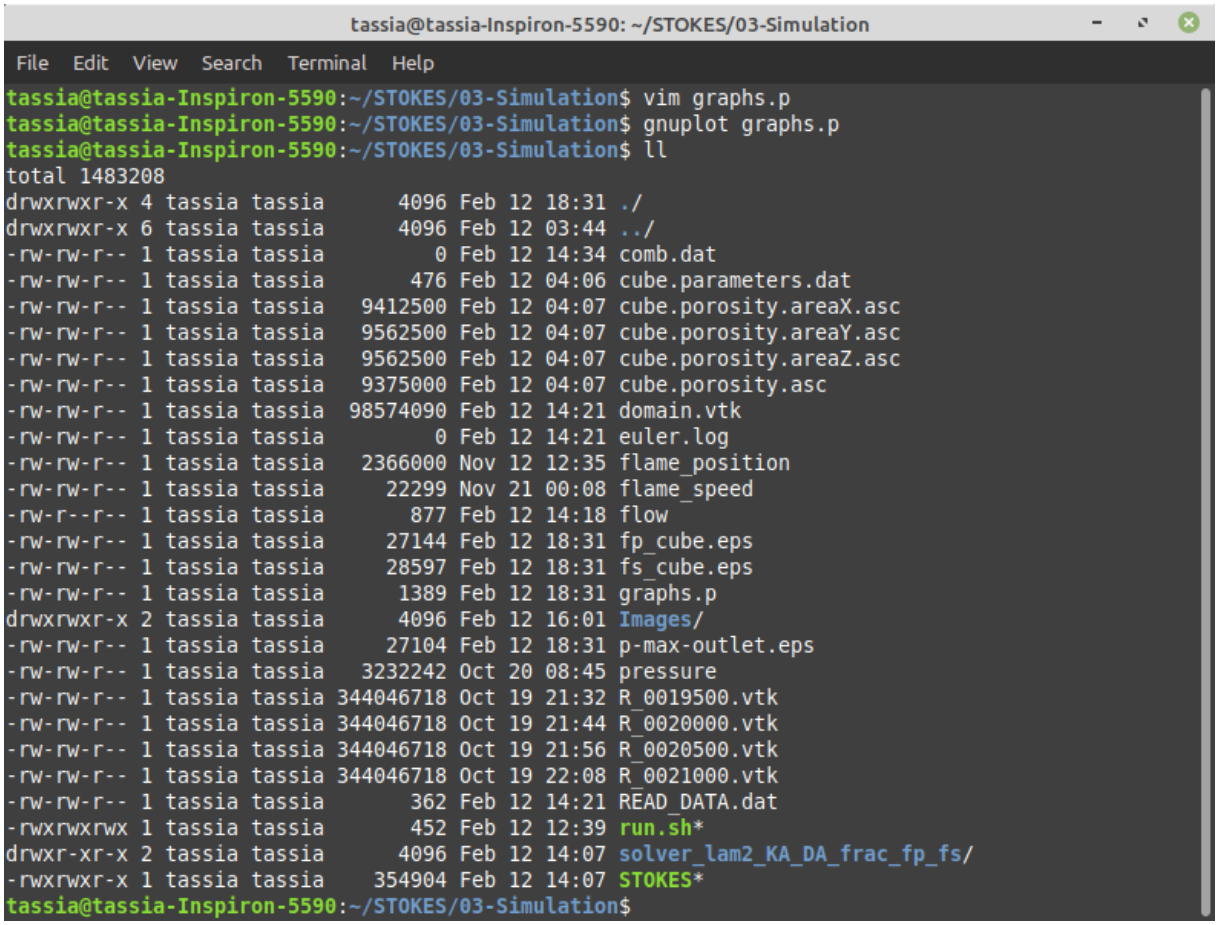

7. The **.eps** files can be open directly from terminal by typing **evince fp_cube.eps** and hitting **Enter**

Bash script for organising graphs

It is convenient to create one last bash script file to help with the directory organisation. This bash script file will be named **tidy.sh** and it will create a directory named **Graphs**, execute gnuplot, and transfer the **.eps** files to the directory **Graphs**.

1. From the **03-Simulation** directory, right-click on any blank space to open a new terminal
2. Type **vim tidy.sh** and hit **Enter**
3. Type **i** to enter **Insert mode**
4. Copy the information below:

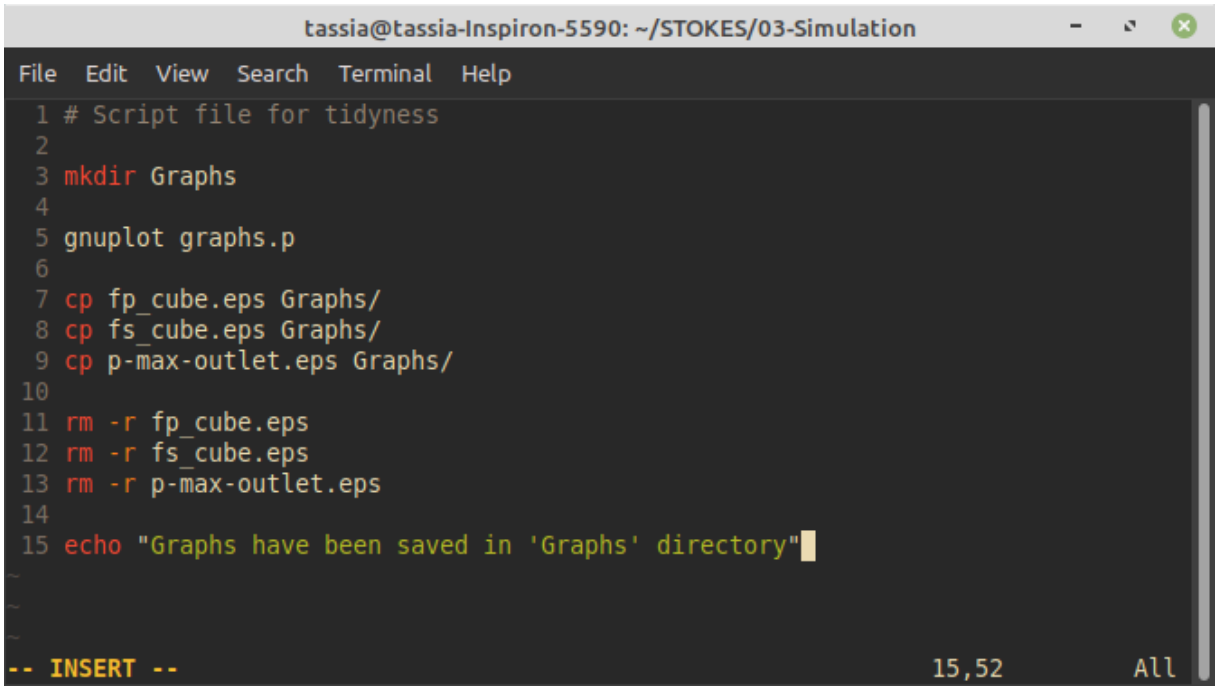

5. Hit **Esc** to exit insert mode
6. Type **:wq** to save the file and exit. The bash script file **tidy.sh** was created.
7. Type **chmod 777 tidy.sh** to make the file executable
8. Type **./tidy.sh** to execute the file. This generate graphs with gnuplot and save the **.eps** files in the **Graphs** directory.

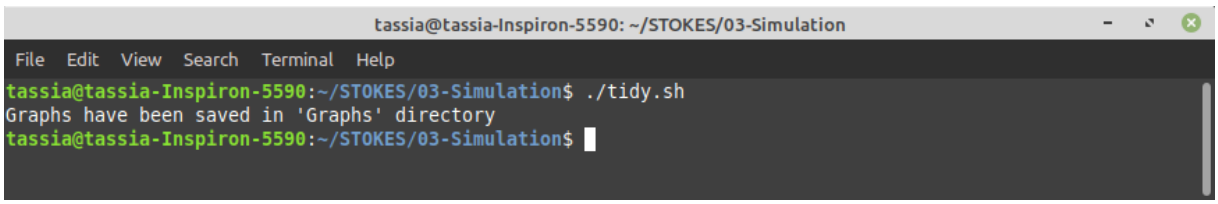

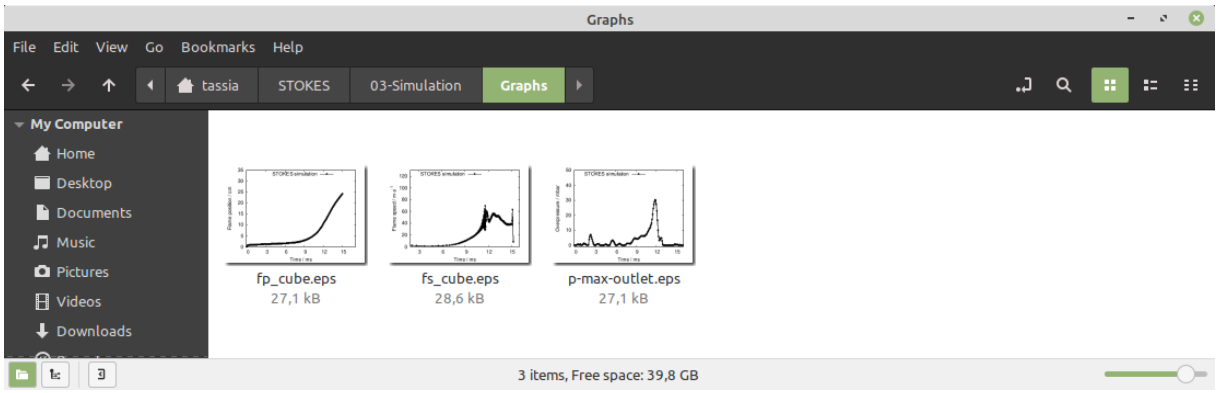
Graphs
File Edit View Go Bookmarks Help
tassia
STOKES
03-Simulation
Graphs
My Computer
Home
Desktop
Documents
Music
Pictures
Videos
Downloads
fp_cube.eps
27,1 kB
fs_cube.eps
28,6 kB
p-max-outlet.eps
27,1 kB
3 items, Free space: 39,8 GB

C Chamber 3 tests

This appendix shows several sensitivity analysis of the flame behaviour to variations in the constants c_L and c_{LAM}, as well as variations in Re_{th} in Chamber 3. The constant c_L belongs to the model of the integral length of wrinkling $\hat{L}_y$, whereas c_{LAM} is part of the laminar burning model. The threshold value of Re_{th} determines the transition from the laminar to the turbulent regimes of propagation.

C.1 Calibration of c_L constant

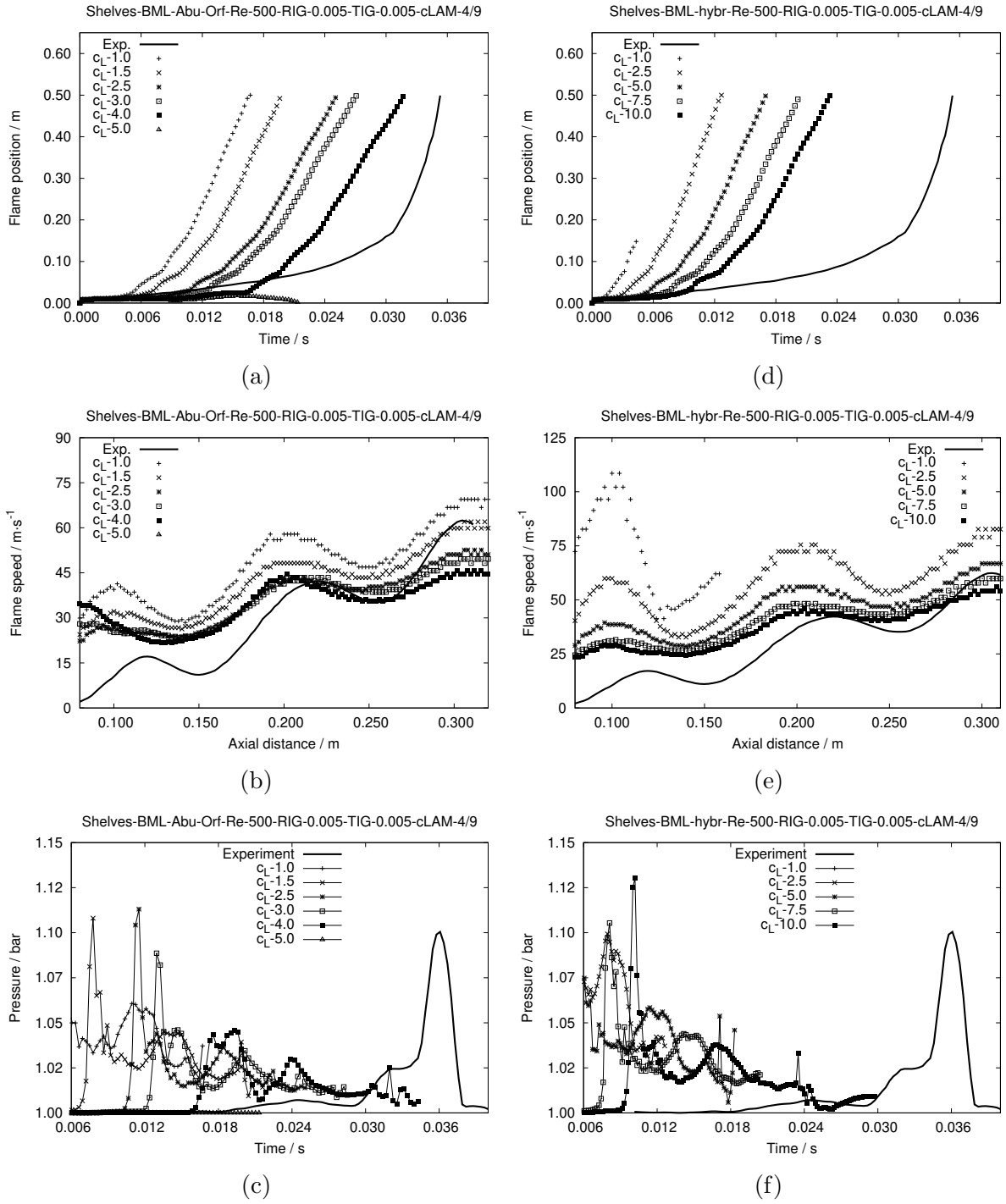

Figure C.1: Calibration of the c_L constant in the models BML-Abu-Orf (a; b; c) and BML-hybrid (d; e; f) in Chamber 2. (a) and (d) Flame position; (b) and (e) Flame speed; (c) and (f) Maximum overpressure. Values of Re_{th} and c_{LAM} are taken respectively as 500 and 4/9.

C.2 Varying c_{LAM}

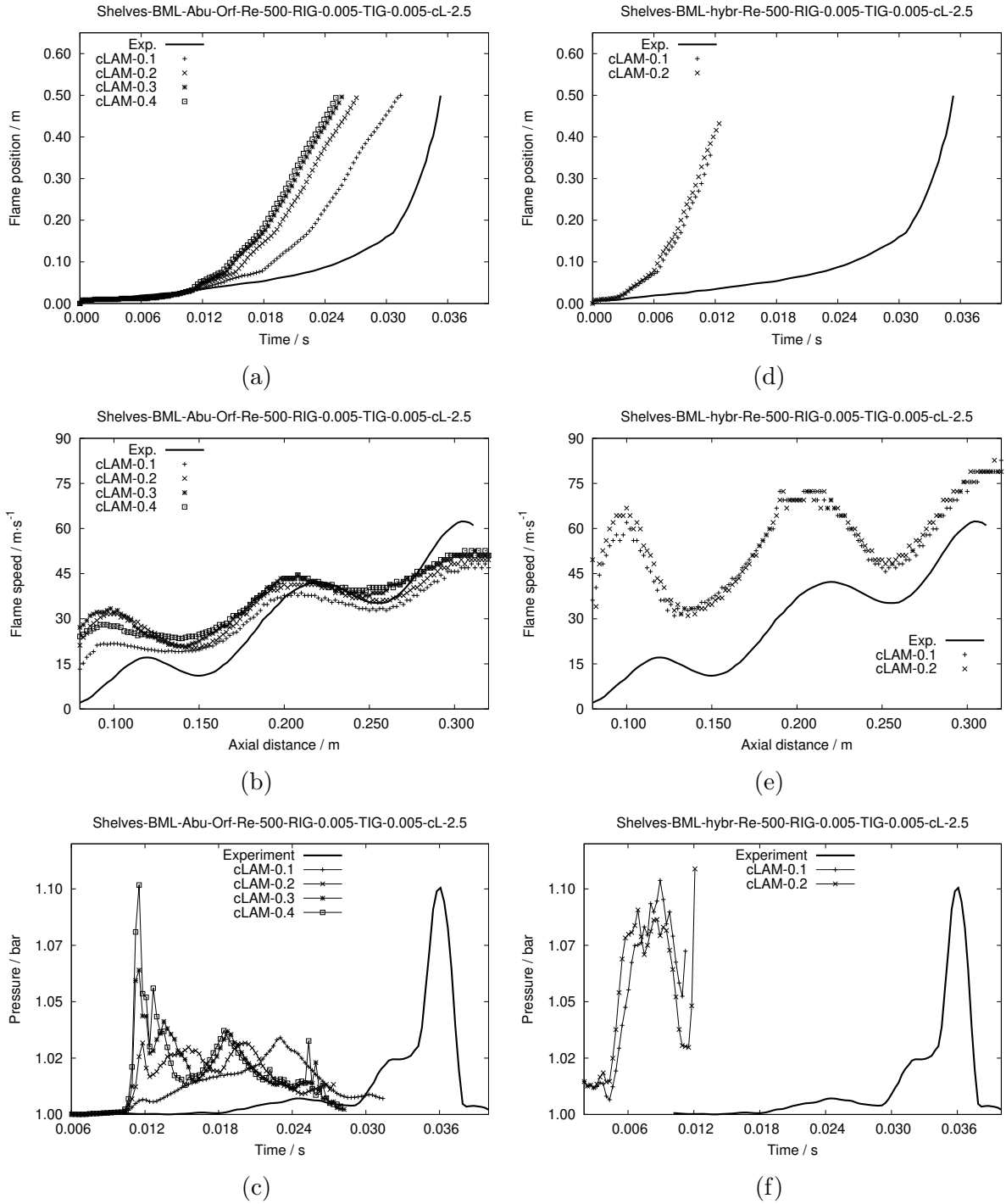

Figure C.2: Calibration of c_{LAM} constant in the models BML-Abu-Orf (a; b; c) and BML-hybrid (d; e; f) in Chamber 2. (a) and (d) Flame position; (b) and (e) Flame speed; (c) and (f) Maximum overpressure. Values of Re_{th} and c_L are taken respectively as 500 and 2.5.

C.3 Varying Re_{Th}

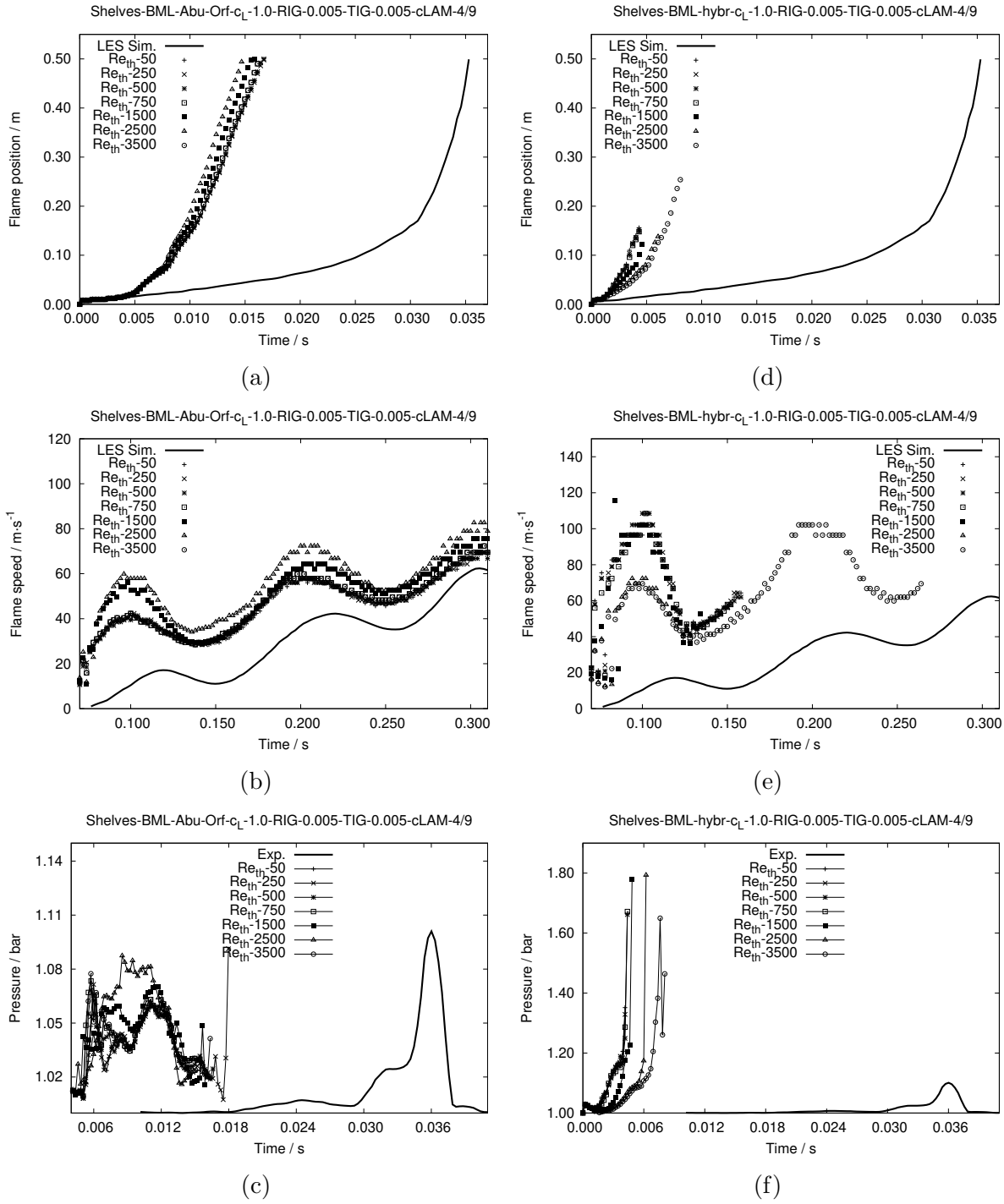

Figure C.3: Varying the Re_{th} in the models BML-Abu-Orf (a; b; c) and BML-hybrid (d; e; f) in Chamber 2. (a) and (d) Flame position; (b) and (e) Flame speed; (c) and (f) Maximum overpressure. Values of c_L and c_{LAM} are taken respectively as 1.0 and 4/9.